Characterization of noise sources in semiconductor qubit devices

by

Yujun Choi

A dissertation submitted in partial fulfillment of
the requirements for the degree of

Doctor of Philosophy
(Physics)

at the
University of Wisconsin-Madison
2023

Date of final oral examination: 6/14/2023

The dissertation is approved by the following members of the Final Oral Committee:

Robert Joynt, Professor, Physics
Mark Friesen, Distinguished Scientist, Physics
Mark Rzchowski, Professor, Physics
Ying Wang, Assistant Professor, Electrical and Computer Engineering

Abstract

Quantum computing has garnered substantial attention in recent decades for its potential applications across various domains such as cybersecurity, chemical engineering, logistics optimization, data search, drug synthesis, and machine learning. However, practical utilization of quantum computing faces significant challenges due to considerable overhead. Even with the aid of state-of-the-art quantum error correction codes, millions of physical quantum bits (qubits) are required. This necessity arises from limitations in gate fidelities of qubits resulting from environmental noise. Therefore, it is imperative to investigate noise source characteristics and devise strategies to mitigate their impact on qubits.

Semiconductor qubits offer a promising platform that can be readily expanded by leveraging existing semiconductor industry facilities. In semiconductor devices, an array of detrimental noise sources, such as charge noise, hyperfine noise, evanescent-wave Johnson noise, and phonon-induced noise, can degrade coherence of the qubits. This dissertation specifically focuses on charge noise ($1/f$ noise).

The dissertation commences by introducing a methodology to characterize diverse noise sources through the measurement of coherence times while rotating a vector magnet in a spin qubit device. Subsequently, it presents the application of a technique called noise source driving to enhance coherence of qubits. This approach involves applying an oscillating electric field to the charge noise sources. Following this, the dissertation elucidates a plausible mechanism explaining the pulse-induced resonance frequency shift of a qubit with fluctuations of two-level systems. Lastly, the dissertation discusses future research directions and concludes with closing remarks.

Acknowledgements

First of all, I would like to thank God, who guided me to the University of Wisconsin-Madison and has enabled me to complete my PhD degree. The passage from Korea to this point seemed impossible due to mandatory military service. However, I discovered an exemption opportunity that paved the way for me to pursue my studies in the United States. I quote a passage from the Bible that encapsulates my sentiments: *"For You created my inmost being; You knit me together in my mother's womb. I praise You because I am fearfully and wonderfully made; Your works are wonderful, I know that full well."*

I extend my thanks to my esteemed committee members, Dr. Robert Joynt, Dr. Mark Friesen, Dr. Mark Rzchowski, and Dr. Ying Wang, for dedicating their valuable time to my dissertation and defense. Above all, I am genuinely grateful to Robert Joynt for serving as my advisor. When I initially approached him to become his research assistant, my knowledge of semiconductor qubit devices and noise sources was limited, and I harbored concerns about conducting theoretical research effectively. However, he consistently provided guidance and instruction, allowing me to expand my understanding each week. If I become a professor in the future, I will strive to emulate his advising approach. I deeply appreciate the insightful comments and kind advice from Mark Friesen and Susan Coppersmith during our weekly group meetings. The discussions we had, particularly during the challenging times of the widespread COVID-19 pandemic, were instrumental in keeping my studies on track. I would also like to thank Leah Tom and Hruday Mallubhotla for sharing their perspectives and collaborating with me during our regular meetings. Additionally, I am grateful for the assistance provided by Jeffrey Schmidt, Jim Reardon, and Michelle Holland, who helped me acclimate to the Department of Physics and guided me in choosing my advisor when I first joined as a graduate student. I also want to thank Erika Kawakami, Michael Wolfe, and Santiago Serrano for sharing their experimental data and generously addressing my inquiries regarding their devices.

The support and love of my family were indispensable in completing my PhD degree. I am truly grateful to my wife, Han Ah Yoo, who has always been supportive and encouraging, providing assistance whenever I felt exhausted during my research journey. My parents have been a solid foundation, providing me with the opportunity to pursue my academic goals. My sister has been a lighthouse, facilitating my study abroad in the United States, while my brother has been a constant source of encouragement through regular communication. I believe that their unconditional love has propelled me to where I am today.

It was great honor to have my friends in the United States. I would like to thank brothers and sisters at the Korean Presbyterian Church of Madison and His Ambassadors Fellowship UPC of Madison. Fellowship with them has provided invaluable support and solace during my academic pursuits. In particular, I experienced immense joy in meeting the members of Mahanaim, who serve as the praise and worship team at the Korean church. The O'Neal family, including Pastor George, Pam, and Liana, have consistently cared for me and uplifted me with their prayers. It was a pleasure to meet Minho Kwon, Joon Suk Huh, Sanghyeok Park, Eunji Oh, Hyunheung Cho, and Soyeon Choi, who were fellow Korean students majoring in physics. I

thoroughly enjoyed spending time with Donghwan Jeon and Changkeun Oh. I extend my gratitude to Soyeon Chang and Youjeong Jeon for their valuable feedback on my PhD application materials, as well as the encouragement from Youngkyu Sung and Jinbong Lee.

I acknowledge the financial support from Kwanjeong Educational Foundation. Their scholarship for graduate students studying abroad has enabled me to dedicate my full attention to my research.

My research at UW-Madison was sponsored in part by the Army Research Office (ARO) under Grant Number W911NF-17-1-0274. The views and conclusions contained in this document are those of the authors and should not be interpreted as representing the official policies, either expressed or implied, of the Army Research Office (ARO), or the U.S. Government. The U.S. Government is authorized to reproduce and distribute reprints for Government purposes notwithstanding any copyright notation herein.

Contents

List of Figures

List of Tables

Chapter 1

Introduction

1.1 Quantum computing

Since its initial proposal in 1981 by Feynman [1], quantum computing has emerged as a dynamic field of study within physics. While the concept originated from simulating quantum systems using other quantum systems, numerous studies have been conducted on universal quantum computing, which aims to achieve general-purpose capabilities similar to classical computers. Notably, the discovery of quantum algorithms applicable to real-world problems has greatly invigorated the field. One such example is the Shor algorithm, which enables efficient factorization of large prime numbers compared to classical algorithms such as the number field sieve [2]. This breakthrough has implications for breaking public-key cryptography, including the widely used RSA scheme [3]. Additionally, the Grover algorithm provides a quadratic speed-up for searching specific data within unsorted datasets [4], addressing the needs of modern society, where the handling of vast amounts of data is increasingly important.

At the core of quantum computing lies the quantum bit (qubit), the fundamental computational unit. Unlike classical bits that represent either 0 or 1, qubits can exist in superpositions of these states. Mathematically, a qubit can be expressed as:

$$|\psi\rangle = a|0\rangle + b|1\rangle = \begin{pmatrix} a \\ b \end{pmatrix}, \tag{1.1}$$

where a and b are complex numbers satisfying $|a|^2 + |b|^2 = 1$. While this pure state representation is often convenient, a more general description of a qubit utilizes the density operator representation:

$$\rho = \sum_j p_j |\psi_j\rangle\langle\psi_j|, \tag{1.2}$$

where ρ represents the density operator for an ensemble of pure states $|\psi_j\rangle$ with respective probabilities p_j. This representation can also be expressed in matrix form as:

$$\rho = \begin{pmatrix} \rho_{00} & \rho_{01} \\ \rho_{10} & \rho_{11} \end{pmatrix}, \tag{1.3}$$

with the basis set, $\{|0\rangle, |1\rangle\}$. The trace is conserved, $\mathrm{Tr}(\rho) = \rho_{00} + \rho_{11} = 1$, and the matrix is Hermitian, $\rho_{01} = \rho_{10}^*$.

Multiple qubits can be represented by a set of computational basis states, for the case of n qubits, $\{|0\rangle, |1\rangle\}^{\otimes n}$. The set contains 2^n basis states. For example, a pure state for two qubits can be expressed as:

$$|\psi\rangle = a|00\rangle + b|01\rangle + c|10\rangle + d|11\rangle = \begin{pmatrix} a \\ b \\ c \\ d \end{pmatrix}, \tag{1.4}$$

where the complex coefficients satisfy $|a|^2+|b|^2+|c|^2+|d|^2 = 1$. This state is referred to as *separable* if it can be written as the tensor product of two single-qubit states, such as $|\psi\rangle = |\psi_1\rangle \otimes |\psi_2\rangle$, and *entangled* if it cannot. The density matrix for n qubits is an $n \times n$ matrix with the given basis set.

The process of quantum computing involves three stages: initialization, gate operations, and measurement. Initially, qubits are typically prepared in the state $|0\rangle^{\otimes n}$. Gate operations involve applying unitary operators to the qubits' states. It is known that a universal gate set for quantum computing can be achieved using single-qubit and two-qubit gates, allowing for the approximation of any unitary operator using a finite number of these gates [5]. Examples of such gates include Hadamard gate, T gate (also known as $\pi/8$ gate), and controlled-NOT gate (CNOT gate), represented by the following matrices, respectively:

$$H = \frac{1}{\sqrt{2}}\begin{pmatrix} 1 & 1 \\ 1 & -1 \end{pmatrix}, \quad T = \begin{pmatrix} 1 & 0 \\ 0 & e^{i\pi/4} \end{pmatrix}, \quad CNOT = \begin{pmatrix} 1 & 0 & 0 & 0 \\ 0 & 1 & 0 & 0 \\ 0 & 0 & 0 & 1 \\ 0 & 0 & 1 & 0 \end{pmatrix}. \tag{1.5}$$

Following gate operations specific to a quantum algorithm, measurement is usually performed by projecting the qubits' state onto their basis states. While this process functions perfectly in theory, its implementation in a real physical system often differs significantly from initial expectations.

1.2 Semiconductor quantum dots

Various physical platforms have been extensively investigated as candidates for implementing qubits and the essential components of quantum computing. These platforms include superconducting circuits [6], trapped ions [7], neutral atoms [8], semiconductor quantum dots [9], color centers in diamond [10], optical systems [11], and topological systems [12]. Each platform has its own advantages and disadvantages in terms of realizing a quantum computer, and their suitability can be assessed based on DiVincenzo's criteria [13]: (1) scalable and well-defined qubits, (2) initialization capability for the qubits, (3) long coherence times of the qubits, (4) a universal gate set for the qubits, and (5) measurement capability for the qubits.

Semiconductor quantum dots have gained significant attention since the proposal of encoding a spin qubit in an electron confined within a quantum dot [14]. The spin qubit is straightforward and intuitive as it involves an inherent two-dimensional quantum system. A wide range of qubit implementations in quantum dots have been suggested and experimentally verified, including charge qubit [15], singlet-triplet qubit [16], exchange-only qubit [17], hybrid qubit [18], hole spin qubit [19], and flip-flop qubit [20].

Quantum dots exhibit several advantageous features according to DiVincenzo's criteria, with the exception of the first criterion, scalability of qubits. The scalability is a crucial factor, as practical applications of quantum computing require millions of qubits [21]. Recent studies have demonstrated universal operation with a 6-qubit processor [22, 23], but quantum dots still lag behind other physical platforms in terms of scalability. This limitation arises from the extremely small size of quantum dots [9]. Specifically, it is challenging to reproduce identical dots even using the same fabrication process and to connect and tune the dots in a dilution refrigerator.

However, it is envisioned that quantum dot devices can be manufactured by leveraging existing semiconductor foundries [24, 25]. This approach would benefit the quantum computing industry by reducing costs associated with building new factories and developing novel mass production technologies. Another potential avenue for scalability is the operation of devices above 1K, resulting in increased cooling power using a simple ^{4}He pump instead of a dilution refrigerator [26, 27].

The other criteria have been partially fulfilled by recent studies demonstrating gate operation fidelities above 99% for single and two-qubit operations for spin qubits [28–33]. The gate errors, approximately 1%, are close to the error threshold of the surface code [34], but further reduction is necessary to enhance practicality.

1.3 Noise problem

The gate fidelities of quantum dot devices are mostly limited by decoherence of qubits [28–30]. Decoherence occurs due to the unavoidable interaction of qubits with the surrounding environment in practical settings. In quantum dot devices, various sources introduce noise that affects the qubits. These include interactions with surrounding nuclear spins (hyperfine noise) [35, 36], fluctuations of background charges (charge noise) [37–40], phonons [41–43], evanescent waves emanating from metals (evanescent-wave Johnson noise) [44, 45], and so on.

Decoherence in quantum systems can be experimentally characterized by two time scales: T_1 and T_2. The relaxation time, T_1, represents the time it takes for a qubit to relax from higher energy state to lower one. On the other hand, the decoherence time, T_2, refers to the time it takes for a qubit to lose its coherence. Additionally, there is an inaccessible time scale, T_ϕ, known as the dephasing time, which accounts for decoherence resulting from pure dephasing. These time scales are related as follows [46]:

$$\frac{1}{T_2} = \frac{1}{2T_1} + \frac{1}{T_\phi}. \tag{1.6}$$

In the latest semiconductor quantum dot qubits, T_1 is in the order of seconds, while T_2 is in the order of microseconds [47]. Therefore, T_ϕ can be approximated as T_2, making the mitigation of decoherence through pure dephasing crucial.

In the theoretical framework using density matrix formalism, pure dephasing can be represented by a Gaussian decay of the magnitude of off-diagonal terms as follows:

$$|\langle \rho_{01}(t) \rangle| = |\langle \rho_{01}(0) \rangle| \exp[-(t/T_\phi)^2], \tag{1.7}$$

where $\langle \cdot \rangle$ denotes the average over the stochastic process caused by noise. This holds only for quasi-static noise ($W(\omega, T_\phi) \approx 1$ in Eq. 1.9). More general dephasing time can be obtained by solving an integral equation numerically [48]:

$$T_\phi^{-2} = C_0 \int_{-\infty}^{\infty} S(\omega) W(\omega, T_\phi)\, d\omega, \tag{1.8}$$

where ω is the angular frequency, and C_0 is a constant determined by the qubit species and the noise source. The power spectral density (PSD) of the noise, denoted as $S(\omega)$, is the Fourier transform of the correlation function, $\langle x(\tau)x(0) \rangle$, where $x(t)$ is a physical quantity of the noise at time t. The window function for integration is given by:

$$W(\omega, T_\phi) = \frac{\sin^2(\omega T_\phi/2)}{(\omega T_\phi/2)^2} \equiv \mathrm{sinc}^2(\omega T_\phi/2), \tag{1.9}$$

assuming the Gaussian approximation is valid, which holds when the data accumulation time is longer than the correlation time (or memory time) of the noise [46]. The window function in Equ. 1.9 is used for the decay of the free induction signal (or Ramsey signal). In the case of spin (Hahn) echo, the window function is given by $\sin^4(\omega T_\phi/4)/(\omega T_\phi/4)^2$.

If the coupling between the qubit and the noise source is strong, the Gaussian approximation may not be accurate, and it is not enough to obtain the PSD for the dephasing time. In this case, specifying the model for the noise source and the coupling is needed [49].

1.4 Spin qubits and charge noise

Spin qubits are highly promising candidates for implementing qubits in semiconductor devices due to their compact size and ability to perform fast gate operations. The two most significant noise sources contributing to the decoherence of spin qubits are hyperfine noise and charge noise [50–52]. Hyperfine noise directly couples the qubit to magnetic noise fields (Overhauser field), while charge noise indirectly affects the qubit through spin-orbit coupling, which can be either natural or artificial depending on the device materials.

Hyperfine noise poses a greater challenge for devices based on III-V semiconductors like GaAs, mainly due to the natural abundance of isotopes with non-zero nuclear spins. However, in devices based on group IV semiconductors such as Si or Ge, the impact of hyperfine noise on decoherence is less severe because these materials have a lower percentage of non-zero nuclear spins, 4.7% ^{29}Si and 7.7% ^{73}Ge [53]. By utilizing isotopic enrichment techniques, the ratio of nuclear spins can be reduced to a level where the coherence of the qubit is primarily limited by charge noise [28, 54].

On the other hand, charge noise is inevitable since the devices require a sufficiently strong spin-orbit coupling to enable fast gate operations through electric dipole spin resonance [55, 56]. Charge noise in semiconductor devices is commonly referred to as $1/f$ noise due to its power-law spectrum, characterized by $S(\omega) \sim 1/\omega^\alpha$ with $0 < \alpha \leq 2$. This type of noise has a detrimental effect on the coherence of qubits, as the dephasing time is inversely proportional to the low-frequency portion of the PSD, as described in the previous section. $1/f$ noise has been reported across a broad range of frequencies and in various devices, including Si/SiGe heterostructures and silicon metal-oxide-semiconductor devices [54, 57, 58].

The most widely accepted theoretical model explaining charge noise involves a multitude of fluctuating two-level systems (TLS) contributing to the noise independently [59]. These TLSs are assumed to have thermally activated switching rates, given by $w(E) = w_0 \exp(-E/k_BT)$, where w_0 is the maximum attempt rate and E is the activation energy for the TLSs. Assuming a constant distribution of activation energies, $D(E)$, the PSD for $1/f$ noise can be represented as follows:

$$S(\omega) = \int s(\omega) D(E)\, dE = \int \frac{1}{\pi} \frac{w(E)}{\omega^2 + w(E)^2} D(E)\, dE \sim k_BT/\omega \tag{1.10}$$

Here, $s(\omega)$ represents the PSD for each TLS, which follows a normalized Lorentzian shape. The integration range should have low and high cut-off frequencies to prevent $S(\omega)$ from diverging, although the specific cut-off frequencies have not been experimentally observed. It is worth noting that a large number of TLSs are not necessary to produce $1/f$ noise; it can be composed of a few Lorentzians with switching rates following a log-uniform distribution. The physical origin of charge noise has been the subject of study since its discovery in 1925 [60], and despite considerable efforts, it remains unclear compared to other noise sources.

1.5 Dissertation outline

This dissertation explores the various sources of noise that affect qubits in quantum dot devices, with a primary focus on charge noise, which plays a crucial role in the decoherence of qubits. The main objectives of this research are to identify the dominant noise mechanism in these devices, characterize the properties of TLSs, and enhance the coherence of qubits by mitigating the effects of charge noise.

Chapter 2 delves into the methodology used to identify the dominant noise source that affects spin qubits in quantum dot devices. The chapter begins by introducing the equations that govern the coherence times, T_1 and T_2, of spin qubits. To simulate the effects, a hypothetical model device is employed, borrowing parameters from a spin qubit device with micromagnets. By calculating T_1 and T_2 while varying the rotation angles of the applied magnetic field, the chapter presents diverse anisotropy patterns for T_1 and T_2 resulting from different noise sources and charge noise models. The chapter concludes with a discussion and summary of the findings.

Chapter 3 focuses on a technique that improves qubit coherence by applying an oscillating electric field to the TLSs. The chapter begins with a brief review of noise source driving in solid-state systems and introduces the concept of stochastic resonance. It then presents a model Hamiltonian for TLSs and the Lindblad master equation, which elucidates the dynamics of a TLS coupled to its environment. Through numerical simulations on both single and multiple TLSs, the chapter demonstrates the shift of the PSD caused by the driving field and the resulting T_ϕ. The results of damped Rabi oscillation for single TLS are also showcased. After discussing relevant physical conditions involving double-well potential, the chapter concludes by offering suggestions for future research.

Chapter 4 explains the mechanism behind the pulse-induced resonance frequency shift in semiconductor-based qubit devices. The chapter initially introduces the commonly observed frequency shift of qubits in modern spin qubit devices. It proposes a model Hamiltonian for TLSs influenced by local, random electric fields, as well as interactions between the TLSs. By employing different physical models, the chapter demonstrates the non-monotonic behavior of the frequency shift as a function of temperature. It discusses simulation results from a large number of samples and provides fitting for recent experimental data. The chapter concludes with a summary and a discussion on an unraveled conundrum.

Chapter 5 suggests future research directions on semiconductor qubit devices. It specifically highlights the importance of conducting studies with cross-PSD of qubits. Furthermore, the chapter proposes a broader research direction in the context of quantum information science.

Chapter 2

Anisotropy of coherence times of spin qubits

This chapter follows closely to the published work, “Anisotropy with respect to the applied magnetic field of spin qubit decoherence times” by Y. Choi and R. Joynt [61].

2.1 Spin qubits as noise sensors

2.1.1 Vector character of coherence times

Spin qubits are sensitive to environmental noise that degrades their coherence. This disadvantage can be exploited reversely by using them as noise sensors. Measuring the coherence times, T_1 and T_2, of the qubits is one of the well-known methods that evaluate the effect of noise, but it is not enough to have just these two times to identify the dominant noise mechanism and find out the positions of the sources, specifically two-level systems (TLS) for charge noise. More sophisticated experiments are needed to obtain detailed information on the physical nature of the noise sources.

The spin qubits are under the influence of effective noise magnetic field, $\mathbf{B}^{(\mathrm{eff})}$, which is a vector. In experiments, a static magnetic field $\mathbf{B}_0$, is applied to the qubits to set their quantization axis that is defined by z axis such as $\mathbf{B}_0 = B_0\hat{z}$. This z axis is not geometric one, but indicates the preferred axis for computational basis of the qubits. The noise power tensor is then

$$\langle B_i^{(\mathrm{eff})}\, B_j^{(\mathrm{eff})}\rangle_\omega = \int dt\, e^{i\omega t}\, \langle B_i^{(\mathrm{eff})}(t)\, B_j^{(\mathrm{eff})}(0)\rangle, \tag{2.1}$$

where the angle bracket, $\langle\cdot\rangle$, denotes a quantum and thermal average, the angle bracket with subscript ω, $\langle\cdot\rangle_\omega$, means the Fourier transform of the correlation function with respect to angular frequency ω, and the subscripts i and j are Cartesian components.

The relaxation rate $1/T_1$, is determined by the transverse noise components: $1/T_1 \propto \langle B_x^{(\mathrm{eff})} B_x^{(\mathrm{eff})}\rangle_{\omega_{op}} + \langle B_y^{(\mathrm{eff})} B_y^{(\mathrm{eff})}\rangle_{\omega_{op}}$, which means that the noise power at the operating frequency of the qubits, ω_{op}, is important for T_1. The dephasing rate $1/T_\phi$, on the other hand, is determined by the longitudinal noise component $\langle B_z^{(\mathrm{eff})} B_z^{(\mathrm{eff})}\rangle_\omega$ with Eq. 1.8, in which low-frequency part of the noise power is important for T_ϕ considering the sinc^2 window function. Since we have $1/T_2 = 1/2T_1 + 1/T_\phi$, all of the diagonal components of the noise tensor are experimentally accessible.

The vector character of the coherence time equations suggest that one can investigate the nature of noises in spin qubit devices by measuring T_1 and T_2 as a function of the direction of the applied field. If the applied field is rotated to the direction $\mathsf{R}\hat{z}$, where R is a rotation operator that takes $\hat{z}$ into the direction with polar and azimuthal angle, (θ, ϕ), then $1/T_1(\theta,\phi) \propto \langle B_{\mathsf{R}\hat{x}}^{(\mathrm{eff})} B_{\mathsf{R}\hat{x}}^{(\mathrm{eff})}\rangle_{\omega_{op}} + \langle B_{\mathsf{R}\hat{y}}^{(\mathrm{eff})} B_{\mathsf{R}\hat{y}}^{(\mathrm{eff})}\rangle_{\omega_{op}}$ while $T_\phi(\theta,\phi)$ depends on $\langle B_{\mathsf{R}\hat{z}}^{(\mathrm{eff})} B_{\mathsf{R}\hat{z}}^{(\mathrm{eff})}\rangle_\omega$. We will show that the pattern of $T_1(\theta,\phi)$ and

$T_\phi(\theta, \phi)$ gives information about the nature of the noise sources and their positions relative to the qubit.

2.1.2 Applicability

For charge qubits, the analog of the applied field direction is the direction along the separation between two quantum dots. It is difficult to adjust this direction over a wide range in practice. As a result, the experiments we propose are only possible for spin qubits. In this chapter, we limit the analysis to single-spin devices. The idea of using anisotropy of T_1 and T_ϕ to investigate noise should also be applicable to multi-dot spin qubit devices such as hybrid qubits [62] or singlet-triplet qubits [63]. The analysis is more complicated for these cases. For example, in the two-qubit experiment of Ref. [64], the change in the ratio of g-factors as the field is rotated introduces additional complications. We will not attempt any treatment of these complex multi-qubit systems in this chapter, since we are mainly attempting to establish the basic principles involved, and for this purpose it is best to do the simpler cases first. Nevertheless, it seems likely that the anisotropy of coherence times would be a useful tool even in these more intricate situations.

We focus on the anisotropy of three different types of noise sources: charge noise, hyperfine noise, and evanescent-wave Johnson noise (EWJN) in silicon devices. Charge noise is the most crucial one at low frequencies and generally determines T_2. Hyperfine noise is also important for T_2, particularly in GaAs systems. It is expected to be isotropic in $\mathbf{B}_0$, which from the viewpoint of this chapter is a key experimental signature of this type of noise [65], as we shall discuss below. EWJN is important at higher frequencies and low magnetic fields, and in many cases may determine T_1. Phonon-induced relaxation mediated by spin-orbit coupling, in contrast, is highly anisotropic, as shown previously [42, 66]. This mechanism is essential at higher magnetic fields B_0. Since we do not include it, the results we present here hold only for $B_0 \leq$ 3-4 T [67]. At these lower fields T_1 saturates. It is noteworthy that the anisotropy due to phonon effects is determined by the orientation of $\mathbf{B}_0$ relative to the crystal axes, while the anisotropy considered in this chapter is relative to the direction determined by the geometry of the device. Hot spots, where the valley and Zeeman levels cross, are also a strong source of decoherence [68]. Fortunately, it is relatively easy to avoid this by tuning the strength of the applied field, and this would be necessary for the proposed experiment to work. In metal-oxide-semiconductor (MOS) structures the Dresselhaus interaction can be strong and anisotropic. This gives rise to anisotropic T_2 from charge noise that was measured in Ref. [69]. Here we focus on dots in heterostructures, where the angular variation of the spin-orbit coupling is expected to be much weaker.

In most experiments on spin qubits, the relative orientation of the sample and the applied magnetic field is not allowed to vary. However, rotatable sample holders can give some variation in the angle between the growth direction and the applied field [70]. Full coverage of the whole solid angle can be obtained from vector magnet arrangements with appropriate parameters of the magnets. Indeed, experiments to optimize qubit operation by changing the direction of the applied field have been carried out [71]. This paper can be viewed as an aid to these kinds of efforts, since the direction of maximum coherence times can be inferred from the calculations. Other phenomena that have been investigated by rotating the field are the variations in the Rabi frequency of multi-hole qubits in Si [72] and the profile of the spin-orbit interaction of a silicon double quantum dot in MOS structures [73, 74].

This chapter will focus on experiments that use micromagnets to provide magnetic field gradients at the position of a spin qubit. The direction of the magnetization of the micromagnets can be affected by the rotation of the applied field in a way that is not well understood and that is difficult to measure. This means that to carry out the proposed experiment here, hard magnets must be used.

2.2 Coherence times in a rotating magnetic field

2.2.1 Relaxation time

The relaxation rate of a spin qubit in the noise magnetic field depends on the noise correlation function $\langle B_i^{(\text{eff})}(t) B_j^{(\text{eff})}(0)\rangle_{\omega_{op}}$. The effective noise magnetic field is any time-dependent field that couples to the spin qubit. Hence this could be a physical magnetic field, a field that comes from the motion of the qubit in an inhomogeneous field, a field that results from phonons mediated by spin-orbit coupling, *etc.*

T_1 depends only on the transverse components of the noise power tensor. If we define $T_1^{(i)}$ as the relaxation time when the applied field is in the i-direction, then the relaxation rates are

$$\begin{aligned}
\frac{1}{T_1^{(x)}} &= (\frac{\mu_B}{\hbar})^2 \left[\langle B_y^{(\text{eff})} B_y^{(\text{eff})}\rangle_{\omega_{op}} + \langle B_z^{(\text{eff})} B_z^{(\text{eff})}\rangle_{\omega_{op}}\right], \\
\frac{1}{T_1^{(y)}} &= (\frac{\mu_B}{\hbar})^2 \left[\langle B_z^{(\text{eff})} B_z^{(\text{eff})}\rangle_{\omega_{op}} + \langle B_x^{(\text{eff})} B_x^{(\text{eff})}\rangle_{\omega_{op}}\right], \\
\frac{1}{T_1^{(z)}} &= (\frac{\mu_B}{\hbar})^2 \left[\langle B_x^{(\text{eff})} B_x^{(\text{eff})}\rangle_{\omega_{op}} + \langle B_y^{(\text{eff})} B_y^{(\text{eff})}\rangle_{\omega_{op}}\right].
\end{aligned} \tag{2.2}$$

μ_B is the Bohr magneton. We take $g = 2$.

If the applied field is in an arbitrary direction $\hat{n} = \sin\theta\cos\phi\,\hat{x} + \sin\theta\sin\phi\,\hat{y} + \cos\theta\,\hat{z}$, where θ is the polar angle and ϕ is the azimuthal angle with respect to the growth direction, then the relaxation rate becomes

$$\frac{1}{T_1(\theta,\phi)} = (\frac{\mu_B}{\hbar})^2 \sum_{i,j} Q_{ij}^{(1)} \langle B_i^{(\text{eff})} B_j^{(\text{eff})}\rangle_{\omega_{op}} \tag{2.3}$$

where the matrix elements for rotation are

$$\mathsf{Q}^{(1)} = \begin{bmatrix} \cos^2\phi\cos^2\theta + \sin^2\phi & -\cos\phi\sin\phi\sin^2\theta & -\cos\phi\cos\theta\sin\theta \\ -\cos\phi\sin\phi\sin^2\theta & \sin^2\phi\cos^2\theta + \cos^2\phi & -\sin\phi\cos\theta\sin\theta \\ -\cos\phi\cos\theta\sin\theta & -\sin\phi\cos\theta\sin\theta & \sin^2\theta \end{bmatrix}$$

with $\{x, y, z\}$ as the basis for the matrix $\mathsf{Q}^{(1)}$. Note that if there are any nonzero off-diagonal correlation functions $\langle B_i^{(\text{eff})} B_j^{(\text{eff})} \rangle_{\omega_{op}}$ $(i \neq j)$, they are also needed in the expression for the relaxation rate.

2.2.2 Dephasing time

The calculation of the dephasing time is more complicated than that for the relaxation time, since it depends more broadly on the full frequency spectrum of the noise and higher-level correlation functions. For the purposes of this chapter, only ratios of T_ϕ for different applied field angles are essential. Hence the specific approximation used to compute T_ϕ is not so crucial. If the applied field is in the z-direction, the specific form of Eq. 1.8 reads

$$T_\phi^{-2} = \frac{1}{2}(\frac{2\mu_B}{\hbar})^2 \int_{-\infty}^{\infty} d\omega\, \langle B_z^{(\text{eff})} B_z^{(\text{eff})} \rangle_\omega \,\text{sinc}^2(\omega T_\phi/2). \tag{2.4}$$

If the applied field is in the arbitrary direction set by (θ, ϕ), then

$$T_\phi^{-2} = \frac{1}{2}(\frac{2\mu_B}{\hbar})^2 \sum_{i,j} Q_{ij}^{(2)} \int_{-\infty}^{\infty} d\omega\, \langle B_i^{(\text{eff})} B_j^{(\text{eff})} \rangle_\omega \,\text{sinc}^2(\omega T_\phi/2) \tag{2.5}$$

where the matrix elements for rotation are

$$\mathsf{Q}^{(2)} = \begin{bmatrix} \cos^2\phi\sin^2\theta & \cos\phi\sin\phi\sin^2\theta & \cos\phi\cos\theta\sin\theta \\ \cos\phi\sin\phi\sin^2\theta & \sin^2\phi\sin^2\theta & \sin\phi\cos\theta\sin\theta \\ \cos\phi\cos\theta\sin\theta & \sin\phi\cos\theta\sin\theta & \cos^2\theta \end{bmatrix}$$

in the same basis as used for $\mathsf{Q}^{(1)}$.

As an equivalent of the equation above, we can define a function $\Gamma(t)$ as

$$\Gamma(t) = \frac{t^2}{2}(\frac{2\mu_B}{\hbar})^2 \sum_{i,j} Q^{(2)}_{ij} \int_{-\infty}^{\infty} d\omega \, \langle B_i^{(\text{eff})} B_j^{(\text{eff})} \rangle_\omega \, \text{sinc}^2(\omega t/2) \tag{2.6}$$

and then solve $\Gamma(T_\phi) = 1$ for T_ϕ to obtain the dephasing time. As mentioned in the introduction chapter, $T_\phi \approx T_2$ in our simulation.

The results of this subsection and the previous one make it clear that the entire tensor structure of the noise correlation function is in principle accessible simply by measuring T_1 and T_2.

2.3 Micromagnets

2.3.1 Conversion of electric to magnetic field noise via micromagnets

Single-qubit logic gates in spin qubit devices are often implemented using micromagnets to set up magnetic field gradients. This leads to the unwanted complication that noise electric field moves the spin up and down the gradient, causing a time-dependent magnetic field $\mathbf{B}^{(E)}$ that can reduce the coherence of the qubit. Here we outline how this plays into the anisotropy effect.

We will take a simple model of a quantum dot confined in a harmonic potential.

The Hamiltonian is

$$\begin{aligned} H &= -\sum_i \frac{\hbar^2}{2m_i}\frac{\partial}{\partial x_i^2} + \sum_i \frac{1}{2}k_i x_i^2 - q\sum_i x_i E_i(t) \\ &= -\sum_i \frac{\hbar^2}{2m_i}\frac{\partial}{\partial x_i^2} + \sum_i \frac{1}{2}k_i(x_i - \frac{qE_i(t)}{k_i})^2 - \sum_i \frac{q^2 E_i(t)^2}{2k_i^2} \end{aligned} \tag{2.7}$$

where i is a Cartesian index, m_i and k_i are the effective mass and spring constant of the electron in the i-direction, q is the electric charge of the electron, and $E_i(t)$ is the noise electric field component in the i-direction. The frequency of the noise electric field is much smaller than the natural frequencies of the harmonic motion, so the Born-Oppenheimer approximation applies and the effect of $E_i(t)$ is to shift the position of the minimum of the potential by $\Delta x_i(t) = qE_i(t)/k_i$. The confinement in the z-direction is much stronger, though the effects of excited states in this potential are measurable [75, 76]. To the level of approximation needed in this chapter, we can drop the z term in the potential in Eq. 2.7 and treat the dot as two-dimensional since $k_z \gg k_x, k_y$.

The micromagnets set up a static magnetic field $\mathbf{B}^m$ that varies strongly in space. The associated effective noise magnetic field that acts on the spin qubit is

$$B_i^{(E)}(t) = \sum_j \frac{\partial B_i^m}{\partial x_j}\Delta x_j(t) = q\sum_j \frac{1}{k_j}\frac{\partial B_i^m}{\partial x_j}E_j(t). \tag{2.8}$$

The magnetic field gradient and the spring constant are device parameters. This equation already shows that considerable device modeling is necessary to extract any interesting information about the noise electric field $E_i(t)$.

2.3.2 Precaution for magnet hardness

In spin qubit experiments carried out to date, the micromagnets are made of pure cobalt [77, 78]. Co is hexagonal with the easy axis for magnetism along the z-direction. The anisotropy parameter (the difference in energy between the z-axis and the x-y plane) is about 10^6 J/m^3, which corresponds to an anisotropy field H_A of about 0.5 T when the magnetization is saturated, as it surely is at the low temperatures of the experiments. This and shape anisotropy will mainly determine the coercive field, though sample-dependent domain wall pinning will also contribute. The anisotropy parameter quoted above is consistent with the results of Ref. [79], though it is sometimes assumed that the magnet will rotate freely [80, 81]. In any case, at the fields of present-day experiments (a fraction of 1 T), the magnet cannot be considered to be hard and some rotation of the direction of the magnetization of the Co micromagnets is certainly to be expected. This will be problematic by changing the field gradient tensor, $\mathsf{Q}^{(1)}$ and $\mathsf{Q}^{(2)}$, that is used to calculate T_1 and T_2 respectively.

The first possible solution is to use a softer ferromagnet with a cubic crystal structure such as Fe, where one could expect that the magnetization follows the applied field. This would erase much of the anisotropy of the coherence times. It is certainly not ideal but might still give useful information about the noise sources.

The second option is to use a harder ferromagnet, so that the field gradient tensor is fixed once and for all when the magnet is cooled in a static magnetic field. There are many possibilities, but one natural suggestion is $\mathrm{SmCo_5}$ which is chemically very close to the Co magnets in current use. The anisotropy field can be as high as $H_A = 55$ T, an order of magnitude higher than pure Co magnets [82]. The magnetization would not be significantly affected by the rotation of the external field. Therefore, the anisotropy of T_1 and T_2 is more pronounced and more information can be extracted from it.

The third possibility is to stick with the Co magnet but to use an external field that is considerably smaller (*e.g.* $B_0 < 0.05$ T) so that the field from the micromagnets is fixed. This has the problem that the energy level splitting of the qubit becomes smaller than $k_B T$, and initializing the spin qubit for measurements is tricky. It is possible only at temperatures of the order of 1 mK, considerably lower than the temperatures in current dilution refrigerators. However, one might still be able to do spin blockade-based measurements.

In this chapter, we shall assume that the second alternative is chosen, since this gives the richest phenomenology, and seems feasible with fairly modest changes in fabrication techniques. Thus, we take the magnetic field gradients to be fixed. This means that the experiment cannot be carried out with the sample of Ref. [78], which uses Co micromagnets and electron temperature of order 150 mK.

2.4 Parameters from a model device

Keeping in mind the precaution in the previous section, we assume that there is a hypothetical device in which the magnetic field gradients do not change with the applied magnetic field direction. The calculations in the following sections will use the parameters from the device of Ref. [78] given below because they have been particularly well-characterized.

The magnetic field gradients at the qubit in units of $\mathrm{mT(nm)^{-1}}$ are $\partial B_x/\partial x = -0.20$, $\partial B_y/\partial x = -0.05$, $\partial B_z/\partial x = -0.27$, $\partial B_x/\partial y = -0.03$, $\partial B_y/\partial y = 0.18$, and $\partial B_z/\partial y = -0.02$. The z-direction of the device is taken to be the growth direction. The variation in the z-direction is not needed in the two-dimension approximation we are using. Other important parameters are the thickness of the aluminum oxide layer

$l = 100\,\mathrm{nm}$, the dielectric constant $\epsilon_d = 13.05$ for $\mathrm{Si}_{0.7}\mathrm{Ge}_{0.3}$ [83], and the transverse effective mass $m = 0.19\,m_e = 1.73\times10^{-31}\,\mathrm{kg}$. The lowest orbital excitation frequency is taken as $\omega_{orb} = 6.84\times10^{11}\,\mathrm{s}^{-1}$ and it is related to the spring constants by the equations $k_x = k_y = m\omega_{orb}^2$. As mentioned earlier, we take $k_z \to \infty$ since confinement is strong along the growth direction. The base temperature is 25 mK, while the electron temperature is about 150 mK, the value we use for the calculations.

Another parameter needed as input to the theory is the conductivity σ of the Au gates. This was not measured in this device, but under similar growth conditions for Au films a value of $\sigma = 2\times10^8\,\mathrm{S\,m}^{-1}$ was obtained at the temperatures of the experiment [84]. We should regard this as a probably somewhat high order-of-magnitude estimate of σ in the actual device, and we will use a range of values for σ. We take the gate thickness as $w = 25\,\mathrm{nm}$, and the distance from the qubit to the gates $d = 137\,\mathrm{nm}$. The qubit operating frequency is $\omega_{op} = 2\pi\times12.9\,\mathrm{GHz}$ $= 8.11\times10^{10}\,\mathrm{s}^{-1}$. Two micromagnets made of cobalt are defined on top of the gates, approximately 162 nm above the qubit. In the experiments reported in Ref. [78] the applied field B_0 was in the x-direction. T_2^* of the device was measured to be $840\pm70\,\mathrm{ns}$ and T_1 was in the order of 1 s [85].

2.5 Charge noise

2.5.1 Models for charge noise sources

The exact nature of the low-frequency charge noise remains controversial. There are two leading models for the source of the TLSs that give rise to this noise.

The first model is the proposal of Anderson, Halperin and Varma, and independently Phillips, in 1972 [86, 87]. The picture, shown in Fig. 2.1(a), is that the noise source is the motion of some atom or group of atoms in a potential that supports

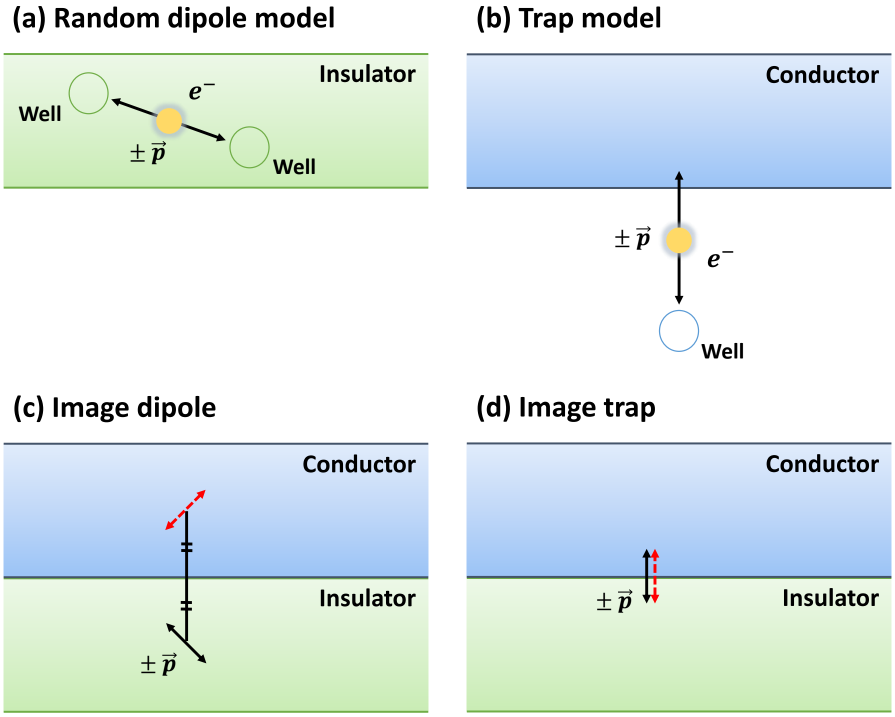

Figure 2.1: Conceptual diagram of random dipole model and trap model. **(a)** and **(b)**: A charge moves back and forth between bistable potential wells in the random dipole model while between the Fermi surface of a conductor and a trap of an insulator in the trap model. Screening effect of metallic gates can be taken into account by adding image charges in the conductor. **(c)** and **(d)**: Resultant image dipole and image trap are depicted as red dashed arrows respectively.

bistability in some range of parameters. The motion also produces a fluctuating dipole moment, which we take as $\pm\mathbf{p}$ in the two stable positions. For the most part, this idea has formed the conceptual background of the field in physics experiments for the last half century. We will assume that the orientation of these dipoles is uniformly random on the unit sphere, and that they are distributed uniformly in space in the oxide layer above the qubit. We call this the random dipole model.

The second model is the related but physically quite distinct idea of McWhorter [88], in which a conducting layer serves as a reservoir for electron traps near the surface of the layer whose energies are close to the Fermi level of the layer. Electrons from the reservoir can hop on and off, again changing the distribution of charge in the system. The change is well approximated by a fluctuating dipole perpendicular to the layer. In this case the fluctuation is between a zero and a fixed nonzero value of the dipole moment, while in the random dipole model the fluctuation is between two different nonzero values. The trap-type TLS is in fact widely thought to be the most important for the noise in field-effect transistors in the engineering community. However, as in the case of the random dipole model, real proof of the details of the model is hard to come by. We call this the trap model. An illustration of the model is given in Fig. 2.1(b).

It is evident that the two models are not easy to distinguish experimentally, since they will both give random telegraph noise with a distribution of switching rates, and reasonable assumptions about the distribution will lead to $1/f$ noise. They differ in the orientation of the effective dipoles, however, suggesting that an experiment that can detect anisotropy in the noise power tensor will distinguish the two models. This forms a chief motivation for the current work.

We note that because of the metallic elements in the device, it is important to include screening of the noise electric field. Electric dipoles near a metal surface at $z = 0$ are screened in an anisotropic fashion. A dipole oriented perpendicularly to the surface is anti-screened, since the image dipole is in the same direction as the original one. This is in sharp contrast to a dipole oriented parallel to the surface, which is strongly screened, with the image dipole opposite in direction to the original one [40]. These image charge effects are taken into account in our calculations by adding an image dipole $\mathbf{p}_{im}$ to the bare dipole $\mathbf{p}_0$. If the bare dipole $\mathbf{p}_0 = (p_{x0}, p_{y0}, p_{z0})$ is located at $\mathbf{r} = (x, y, z)$ relative to a metallic layer at $z = 0$, the image dipole is located at $(x, y, -z)$ and its moment is given by $\mathbf{p}_{im} = (-p_{x0}, -p_{y0}, p_{z0})$. Examples of a bare dipole and corresponding image dipole for the random dipole and trap models are shown in Fig. 2.1(c) and Fig. 2.1(d) respectively.

2.5.2 Source positions

Anisotropy of the coherence times can come from several sources. We have seen that the random dipole and trap models have characteristic anisotropy signatures. In addition to this, it is possible for charge noise sources to be clumped, which is due to a tendency to adhere to different device elements, or particularly in the case of only a few sources, to cluster by random chance. Of course if the noise is coming from a certain direction this is also a source of anisotropy.

This leads to distinguishing four models all together, which we call the uniformly distributed dipole model (UD), uniformly distributed trap model (UT), localized cluster dipole model (CD), and localized cluster trap model (CT). The U-type models assume that the sources are many in number and uniformly distributed, while the C-type models assume that the sources are relatively few in number. The total number or density of the sources is another important subject to study [40, 89].

The U- and C- type models represent limiting cases of very many and just a few closely spaced noise sources, respectively. It is not possible to rule out in advance a lumpy set of 10 to 100 noise sources. The current computational method would need to be developed considerably further to become a useful characterization tool in this difficult intermediate case. In particular, multiple qubits and cross-correlation functions among them would most likely be helpful.

2.5.3 Noise correlation functions

The noise correlation functions for all models are calculated as follows. Let the qubit be at the point $\mathbf{r}$, so we are interested in the correlation function $\langle E_i(\mathbf{r},t)E_j(\mathbf{r},0)\rangle$. Let the dipole be at $\mathbf{r}'$ and the root-mean-square dipole strength be p_0. Define

$\mathbf{R}' = \mathbf{r} - \mathbf{r}'$. Then total noise electric field from dipoles is

$$E_i(\mathbf{r}, t) = \frac{1}{4\pi\epsilon_0} \sum_{\mathbf{r}'} \sum_{k} \frac{3R'_k p_k(t) R'_i - R'_k R'_k p_i(t)}{|\mathbf{R}'|^5}. \tag{2.9}$$

with the subscripts being Cartesian index.

The dipoles, except for the bare and image pairs, are assumed to be statistically independent, so their correlation function is

$$\langle p_i(\mathbf{r}', t) p_j(\mathbf{r}', 0)\rangle = \delta_{mod}\, p_0^2\, g(t). \tag{2.10}$$

where the model-dependent factor $\delta_{mod} = \delta_{ij}/3$ for the random dipole model, $\delta_{mod} = \delta_{iz}\delta_{jz}$ for the trap model, and δ_{ij} is the Kronecker delta. $g(t)$ is the time correlation function for a single dipole, which is assumed to be exponential: $g(t) = e^{-|t|/\tau}$ where τ is the characteristic time of the dipole. This corresponds to random telegraph noise, but the precise model for the time correlations is not that important, since the anisotropic pattern of coherence times depends only on the ratios of specific averages of the correlation functions.

Focusing on the noise from single dipole, the correlation function for effective noise magnetic field is

$$\langle B_i^{(\mathrm{eff})} B_j^{(\mathrm{eff})}\rangle = \sum_{m,n} \frac{q^2}{k_m k_n} \frac{\partial B_i}{\partial x_m} \frac{\partial B_j}{\partial x_n} \langle E_m E_n\rangle. \tag{2.11}$$

where the noise electric fields from the dipole are given as

$$\begin{aligned} E_m(\mathbf{r}, t) &= \frac{1}{4\pi\epsilon_0} \sum_{k} \frac{3R'_k p_k(t) R'_m - R'_k R'_k p_m(t)}{|\mathbf{R}'|^5}, \\ E_n(\mathbf{r}, 0) &= \frac{1}{4\pi\epsilon_0} \sum_{s} \frac{3R'_s p_s(0) R'_n - R'_s R'_s p_n(0)}{|\mathbf{R}'|^5}. \end{aligned} \tag{2.12}$$

Combining the equations above, the correlation function for noise electric field is

$$\begin{aligned}\langle E_m(\mathbf{r},t)E_n(\mathbf{r},0)\rangle =&\frac{1}{16\pi^2\epsilon_0^2}\sum_{k,s}|\mathbf{R}'|^{-10}\\ &\times\langle\, 9R'_kR'_sR'_mR'_np_k(t)p_s(0)-3R'_sR'_nR'_kR'_kp_m(t)p_s(0)\\ &-3R'_kR'_mR'_sR'_sp_n(t)p_k(0)+R'_kR'_kR'_sR'_sp_m(t)p_n(0)\,\rangle.\end{aligned} \tag{2.13}$$

Considering the UD and UT model, we can simplify Eq. 2.13 when the number of dipoles is large substituting integration for the summation over $\mathbf{r}'$ in Eq. 2.9 and using Eq. 2.10 such that

$$\langle E_m(\mathbf{r})E_n(\mathbf{r})\rangle_\omega=\frac{1}{48\pi^2\epsilon_0^2}\rho_vp_0^2\,g(\omega)\int d^3r'\frac{3R'_mR'_n+\delta_{mn}|\mathbf{R}'|^2}{|\mathbf{R}'|^8} \tag{2.14}$$

for the UD model and

$$\begin{aligned}\langle E_m(\mathbf{r})E_n(\mathbf{r})\rangle_\omega=&\frac{1}{16\pi^2\epsilon_0^2}\rho_ap_0^2\,g(\omega)\int d^2r'|\mathbf{R}'|^{-10}\\ &\times\left[9R'^2_zR'_mR'_n-3R'_zR'_n|\mathbf{R}'|^2\delta_{mz}\right.\\ &\left.-3R'_zR'_m|\mathbf{R}'|^2\delta_{nz}+|\mathbf{R}'|^4\delta_{mz}\delta_{nz}\right]\end{aligned} \tag{2.15}$$

for the UT model.

ρ_v and ρ_a are the volume and areal density of dipoles respectively. These densities are assumed to be constant in the region of integration and used as fitting parameters to make $T_2^{(x)}=840\,\mathrm{ns}$ which is the measured value in the experiment [78].

$g(\omega)$ is the Fourier transform of $g(t)$ and often of the $1/f$ type for charge noise. However, one of the important advantages of the experiments described in this chapter is that we can investigate the sources of noise by using spatial and geometric information alone, and the frequency spectrum of the noise is less important. For calculation we simply take $g(\omega)=2\tau/(1+(\omega\tau)^2)$ and τ to be the inverse of maximum attempt frequency in Ref. [40].

The integration region for the UD model is the aluminum oxide layer which is infinite in xy plane, 37 nm above the qubit, and whose thickness is $l = 100\,\text{nm}$, namely $\rho \in [0, \infty)$, $\phi \in [0, 2\pi)$, $z \in [37, 137]\,\text{nm}$ with cylindrical coordinate system. That for the UT model is the interface between the oxide layer and accumulation gates that is $d = 137\,\text{nm}$ above the qubit, *i.e.* $\rho \in [0, \infty)$, $\phi \in [-\pi/4, 5\pi/4]$, at $z = d$. The domain of $\phi \in [-\pi/4, 5\pi/4]$ takes into account the actual gate geometry of the device of Kawakami *et al.* [85].

For the CD and CT models, the passage to an integral as in Eqs. 2.14 and 2.15 is not possible, and the summation over $\mathbf{r}'$ in Eq. 2.9 must be performed explicitly. The overall dipole strength p_0 is used as the fitting parameter of these localized cluster models to make $T_2^{(x)} = 840\,\text{ns}$.

2.5.4 Screening effect of metallic gates

It is important to take into account the screening effect of metallic gates by considering image dipoles. Since an image dipole is formed symmetric to real dipole about the interface between the oxide layer and gates, $R'_z \to 2d - R'_z$. The orientation of the image dipole is reversed in x and y direction such that $p_x \to -p_x$ and $p_y \to -p_y$, which does not have an effect on our random dipole and trap model. Assuming there is no correlation between the dipoles/traps and their images, we can get the total correlation function as a sum of each correlation function:

$$\langle E_m(\mathbf{r}, t) E_n(\mathbf{r}, 0) \rangle = \langle E_m(\mathbf{r}, t) E_n(\mathbf{r}, 0) \rangle_{re} + \langle E_m(\mathbf{r}, t) E_n(\mathbf{r}, 0) \rangle_{im} \tag{2.16}$$

where subscripts re and im denote the correlation function from bare and image dipoles, respectively.

To use Eq. 2.14 for the UD model, two integration regions have to be included in the calculation: $\rho \in [0,\infty),\ \phi \in [0,2\pi),\ z \in [37,137]\,\mathrm{nm}$ for $\langle E_m(\mathbf{r},t)E_n(\mathbf{r},0)\rangle_{re}$ and $\rho \in [0,\infty),\ \phi \in [0,2\pi),\ z \in [137,237]\,\mathrm{nm}$ for $\langle E_m(\mathbf{r},t)E_n(\mathbf{r},0)\rangle_{im}$. This is equivalent to increasing the region of integration to $\rho \in [0,\infty),\ \phi \in [0,2\pi),\ z \in [37,237]\,\mathrm{nm}$ and then using Eq. 2.14. To exploit the formula in Eq. 2.22 and Eq. 2.23, the parameters should be changed to $l = 200\,\mathrm{nm}$ and $d = 237\,\mathrm{nm}$. For the UT model, $\langle E_m(\mathbf{r},t)E_n(\mathbf{r},0)\rangle_{im} = \langle E_m(\mathbf{r},t)E_n(\mathbf{r},0)\rangle_{re}$ because traps are distributed at the interface. Thus, the correlation function for the UT model is effectively increased by a factor of 2, leading to two times of Eq. 2.15 and so does Eq. 2.24.

The noise power tensor for one bare and image pair for the CD model is

$$\langle E_m(\mathbf{r})E_n(\mathbf{r})\rangle_\omega = \frac{1}{48\pi^2\epsilon_0^2}p_0^2\,g(\omega)\left(\frac{3R'_mR'_n+\delta_{mn}|\mathbf{R}'|^2}{|\mathbf{R}'|^8}+\frac{3R''_mR''_n+\delta_{mn}|\mathbf{R}''|^2}{|\mathbf{R}''|^8}\right) \tag{2.17}$$

with $\mathbf{R}'' = (R'_x, R'_y, 2d - R'_z)$, and for the CT model,

$$\begin{aligned}\langle E_m(\mathbf{r})E_n(\mathbf{r})\rangle_\omega =& \frac{1}{8\pi^2\epsilon_0^2}p_0^2\,g(\omega)|\mathbf{R}'|^{-10}\\ &\times(9R'^2_zR'_mR'_n - 3R'_zR'_n|\mathbf{R}'|^2\delta_{mz} - 3R'_zR'_m|\mathbf{R}'|^2\delta_{nz} + |\mathbf{R}'|^4\delta_{mz}\delta_{nz}).\end{aligned} \tag{2.18}$$

The screening effect is included when the rate formulas 2.3 and 2.4 are evaluated for both U- and C- type models.

2.6 Hyperfine noise

The most relevant hyperfine interaction for a spin qubit is Fermi contact interaction, which shows isotropic interaction strength for electrons in quantum dots [90]. The isotropic pattern of T_1 of a spin qubit with respect to the rotation of applied magnetic field was observed by numerical simulation and experiment in Ref. [65].

The studies imply that spin qubit also has isotropic pattern of T_2 because of the isotropic interaction strength.

The isotropic hyperfine noise is taken into account by estimating the decoherence rate from other experiments. It should not differ too much from one device to another. The material in the model device is natural silicon. If the decoherence rate in isotopically purified silicon [39] is subtracted from that in natural silicon [91], we find a hyperfine contribution to the rate of $1/T_2^{hyper} = (1.83\mu\text{s})^{-1} - (20.4\mu\text{s})^{-1} = (2.01\,\mu\text{s})^{-1}$. $1/T_2^{hyper}$ is then simply added to the dephasing rates from charge noise. Hence, $1/T_2(\pi/2, 0) + 1/T_2^{hyper}$ is set to $(840\,\text{ns})^{-1}$ by fitting the densities or dipole strength of charge noise. Because of its isotropy, its effect is to smooth the resulting plots.

The hyperfine noise is not the main factor for the relaxation of a spin qubit in silicon devices: T_1 in the order of tens of seconds for GaAs system was reported at low applied magnetic field [65], and that for Si/SiGe system is expected to be longer than measured T_1 in the order of seconds [85]. Thus we will neglect the hyperfine noise contribution for relaxation rate.

2.7 Evanescent-wave Johnson noise

Evanescent-wave Johnson noise (EWJN) is due to the random motion of charges in the metallic elements of the device. This motion produces random electric and magnetic fields on the qubits in the vicinity of the metal. For the discussion of this effect, let us take the growth direction for the device to be the z-direction, the distance of the qubit from the gate layer as d, the gate thickness as w, and the dielectric constant of the intervening insulating material as ϵ_d.

For the case of noise from a conducting half-space, rather simple formulas are available [44, 92]. In most Si/SiGe heterostructure and Si MOS devices the gates form sheets of metal that can be approximated as a uniform layer from the standpoint of noise production. Thus the theory of EWJN from a film with a finite w is more appropriate. It has been worked out in detail [93], though the results are somewhat complicated, and depend on whether we consider noise electric field or noise magnetic field. For the values of d of interest to us, noise electric field is slightly enhanced for the film case as compared to the half-space case, while the opposite is true for the noise magnetic field, and the effect of finite w is larger. A very good approximation is to use the half space formula for the electric noise and a modified formula for the magnetic case.

Given these considerations, the noise power tensor for electric EWJN at qubit operating frequency is

$$\langle E_z E_z \rangle_{\omega_{op}} = \frac{\hbar \omega_{op} \epsilon_d \epsilon_0}{2\sigma d^3} \coth \frac{\hbar \omega_{op}}{2k_B T} \tag{2.19}$$

where σ is the conductivity of the metallic gates. The other elements of the noise tensor are $\langle E_x E_x \rangle_{\omega_{op}} = \langle E_y E_y \rangle_{\omega_{op}} = (1/2)\langle E_z E_z \rangle_{\omega_{op}}$, while the off-diagonal elements of the tensor vanish. This electric noise is converted into effective noise magnetic field using Eq. 2.11.

The noise power tensor for magnetic EWJN is given by

$$\langle B_z B_z \rangle_{\omega_{op}} = \frac{\hbar \omega_{op} \mu_0 \sigma w}{8d^2} \coth \frac{\hbar \omega_{op}}{2k_B T}. \tag{2.20}$$

This is reduced from the half-space result by a factor of w/d. The other elements of this noise tensor are $\langle B_x B_x \rangle_{\omega_{op}} = \langle B_y B_y \rangle_{\omega_{op}} = (1/2)\langle B_z B_z \rangle_{\omega_{op}}$, while the off-diagonal elements of the tensor vanish. Unlike the electric noise, magnetic EWJN acts directly on the spin qubit to produce decoherence.

2.8 Anisotropy of decoherence time

2.8.1 Decoherence time from evanescent-wave Johnson noise

The measured T_2^* of the model device corresponds to $T_2^{(x)}$ of our simulation because the applied magnetic field B_0 is in the x-direction. For EWJN, the decoherence rate in the i-direction is

$$\frac{1}{T_2^{(i)}} = 2\pi k_B T(\frac{2\mu_B}{\hbar})^2 \lim_{\omega\to 0}\left[\frac{1}{\omega}\langle B_i^{(\mathrm{eff})} B_i^{(\mathrm{eff})}\rangle_\omega\right]. \tag{2.21}$$

This is the rate for the exponential regime when the time $t \gg \hbar/k_B T$. With the correlation function given in Eq. 2.29, the calculated $T_2^{(x)} = 1.19\,\mathrm{s}$ from EWJN is six orders of magnitude larger than the experimental one. Thus the dominant mechanism for the decoherence of the qubit should be charge noise, not EWJN.

2.8.2 Decoherence time from charge noise

For charge noise, $\Gamma(t)$ for the applied magnetic field along the (θ, ϕ) direction can be written as

$$\Gamma(t;\, \theta, \phi) = \sum_{ij} Q_{ij}^{(2)}\left[\gamma_{2x}(t)\frac{\partial B_i}{\partial x}\frac{\partial B_j}{\partial x} + \gamma_{2y}(t)\frac{\partial B_i}{\partial y}\frac{\partial B_j}{\partial y}\right] \tag{2.22}$$

where $\gamma_{2x}(t)$ and $\gamma_{2y}(t)$ are the prefactors related to the gradients in the x- and y-direction respectively.

Now we assume that the TLS noise is a Poisson process with an exponential time correlation functions with characteristic relaxation time τ and carry out the necessary integrations. For the UD model we have

$$\begin{aligned}\gamma_{2x}(t) = \gamma_{2y}(t) = (\frac{2\mu_B}{\hbar})^2(\frac{q}{mw_{orb}^2})^2\frac{\rho_v p_0^2}{576\pi\epsilon_0^2}\left(\frac{1}{l^3}-\frac{1}{d^3}\right) \\ \times 2\pi\tau(t+(e^{-t/\tau}-1)\tau).\end{aligned} \tag{2.23}$$

For the UT model we find

$$\begin{aligned}\gamma_{2x}(t) &= (\frac{2\mu_B}{\hbar})^2(\frac{q}{mw_{orb}^2})^2\frac{(9\pi+6)\rho_a p_0^2}{512\pi^2\epsilon_0^2 d^4} \\ &\times 2\pi\tau(t+(e^{-t/\tau}-1)\tau), \\ \gamma_{2y}(t) &= (\frac{2\mu_B}{\hbar})^2(\frac{q}{mw_{orb}^2})^2\frac{(9\pi-6)\rho_a p_0^2}{512\pi^2\epsilon_0^2 d^4} \\ &\times 2\pi\tau(t+(e^{-t/\tau}-1)\tau).\end{aligned} \tag{2.24}$$

The temporal part of γ_{2x} and γ_{2y} results from the integration of the product of a Lorentzian $g(\omega) = 2\tau/(1+(\omega\tau)^2)$, and $\mathrm{sinc}^2(\omega t/2)$. Those equations are obtained by converting noise electric field correlations (Eq. 2.14 or Eq. 2.15) into effective magnetic field correlation using Eq. 2.8. It is important to note first that the details of the noise spectrum and thus the choice of an exponential correlation are not crucial for the anisotropy patterns, since they depend only on ratios of noise strengths. On the negative side, if some parameter of the noise such as τ itself depends on position in the sample, then the extraction of useful information from the analysis of the data would become far more complicated.

ρ_v and ρ_a are poorly known, so we use them as fitting parameters. $T_2^* = 840\,\mathrm{ns}$ of the model device was measured for only a single direction of the field, indicated by the red dots in Fig. 2.2. This yields $\rho_v = 2.93 \times 10^{20}\,\mathrm{m}^{-3}$ and $\rho_a = 2.66 \times 10^{11}\,\mathrm{m}^{-2}$ for Fig. 2.2(a) and Fig. 2.2(b), respectively.

The anisotropy maps of T_2 for the various models are shown in Fig. 2.2. There

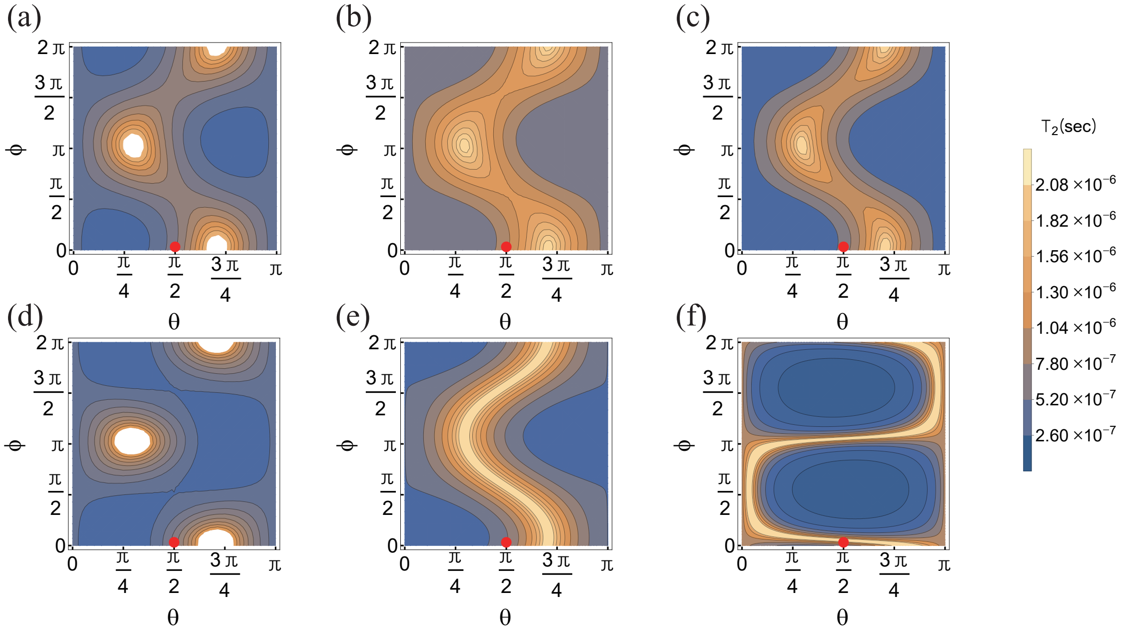

Figure 2.2: The anisotropy maps of decoherence time T_2. x and y axis are the polar angle θ and the azimuthal angle ϕ with respect to the device's z-direction, respectively. The models used for simulations are: **(a)** uniformly distributed random dipoles (UD), **(b)** uniformly distributed traps (UT), **(c)** and **(d)** single dipole cluster (CD) located at $(x, y, z) = (37, 0, 37)$ nm and $(x, y, z) = (0, 37, 37)$ nm respectively, **(e)** and **(f)** single trap cluster (CT) located at $(x, y, z) = (37, 0, 137)$ nm and $(x, y, z) = (0, 37, 137)$ nm respectively. The qubit is located at the origin. The applied field direction $(\theta, \phi) = (\pi/2, 0)$ used in the experiment is indicated by the red dot. For the uniform distribution models in (a) and (b), the volume density ρ_v and areal density ρ_a are respectively used as fitting parameters to match $T_2(\pi/2, 0)$ to the experimental value, 840 ns, and for single cluster models in (c)-(f) the dipole strength p_0 is used as a fitting parameter.

is some redundancy in the maps since they are symmetric under the transformation $\theta \to \pi - \theta$ and $\phi \to \pi + \phi$, stemming from $T_2(\mathbf{B}_0) = T_2(-\mathbf{B}_0)$. This same redundancy also arises in the anisotropy maps of T_1 in Fig. 2.3. We have chosen to show the full angular ranges since in some instances the topology of the function is clearer this way.

The background $T_2^{hyper} = 2.01\,\mu$s sets an upper bound on the plotted values in Fig. 2.2. The white regions in Fig. 2.2(a) and Fig. 2.2(d) represent angular regions where the charge noise contribution is negligible and this upper bound is reached.

Fig. 2.2(a) shows the results for the UD model and Fig. 2.2(b) for the UT model. The horizontal (vertical) axis denotes polar (azimuthal) angle with respect to the device's z-direction. The key feature of these two models is that anisotropy of T_2 results only from the magnetic field gradients. The patterns are not too dissimilar, with the ratio between maximum and minimum values being around 3 for the UD model and 2 for the UT model. The main difference between the UD and UT models is that the peaks and valleys are broader in the UT model. In the UD model, the dipoles are oriented randomly, while in the UT model they are in the z-direction. The differences in the anisotropy maps between UD and UT models can be traced back to the different behavior of electric field lines from these two different types of sources. However, this does not manifest itself in a simple way because of the complexity of the gradient tensors that mediate the electric noise. Because of that, it is difficult to develop much physical intuition about the distinction between UD and UT charge noise sources from inspection of the anisotropy maps, and it appears that a full calculation is necessary to test the differences between the two noise models.

The anisotropy maps for the CD model, a localized dipole cluster, are shown in Fig. 2.2(c) and in Fig. 2.2(d). The cluster is located at $(x, y, z) = (37, 0, 37)$ nm and $(x, y, z) = (0, 37, 37)$ nm respectively. The maps for the CT model, a localized trap cluster, are shown in Fig. 2.2(e) and Fig. 2.2(f). The trap is located at $(x, y, z) = (37, 0, 137)$ nm and $(x, y, z) = (0, 37, 137)$ nm respectively. In both CD and CT models, the qubit is located at the origin. Thus Fig. 2.2(c) (Fig. 2.2(d)) is directly comparable to Fig. 2.2(e) (Fig. 2.2(f)). Figs. 2.2(c)-2.2(f) exhibit more anisotropy relative to the uniform distribution models. This is expected since the localization of the source itself introduces anisotropy. On the other hand, one might expect that C- and U-type models would be easy to distinguish because of a simpler azimuthal dependence for the latter. But once more because of the mediation of the noise by the complicated field gradient tensors, such simple expectations are not borne out.

The difference between the CD and CT models lies in the dipole orientation. In the CD model, it is assumed that the cluster contains dipoles of all orientations and the noise electric field is averaged over the solid angle. This washes out the anisotropy to some extent, but the pattern still depends on the direction of the line connecting the dipole and the qubit. The distance between the dipole and qubit just changes the overall magnitude of T_2. In the CT model, however, the trap generates a noise electric field with more directionality, so the overall anisotropy patterns are sharper and both the direction and the distance are important.

Comparing Fig. 2.2(c) to Fig. 2.2(d) and Fig. 2.2(e) to Fig. 2.2(f) indicates that the source position has a large effect. To understand this in more detail, let us focus on the CT model in Fig. 2.2(e) and Fig. 2.2(f). Note that $\partial B_x/\partial x$, $\partial B_z/\partial x$, and $\partial B_y/\partial y$ are an order of magnitude greater than the other gradient terms. In Fig. 2.2(e), the electric field at the qubit has only x and z components. The x component contributes to $1/T_2$ after multiplication by $\partial B_x/\partial x$ and $\partial B_z/\partial x$. Thus small T_2 is expected when the applied field is in the x and z directions, which can be identified on the map with $(\theta, \phi) = (\pi/2, 0)$ and $(\theta, \phi) = (0, 0)$, respectively. On the other hand, in Fig. 2.2(f), the electric field at the qubit has only y and z components. The leading contribution to $1/T_2$ is the result of the product of the y component and $\partial B_y/\partial y$. A small T_2 is expected with the applied field is in the y-direction, which is seen at the point $(\theta, \phi) = (\pi/2, \pi/2)$ on the map. Thus for the distinction between CD and CT models, some relatively simple physical considerations can help to decipher the anisotropy map.

It is important to point out that if relatively few two-level systems contribute to the dephasing of the qubit, as is often hypothesized based on deviations for power-law spectra [40, 94], the anisotropy can be used to determine the source position and to distinguish between random dipole and trap models for the charge noise. The present method can be extended to models with very few sources by eliminating the averaging we have performed, but the analysis quickly becomes complicated.

2.9 Anisotropy of relaxation time

2.9.1 Relaxation time from charge noise

The relaxation rate with applied magnetic field in (θ, ϕ) direction is

$$\frac{1}{T_1(\theta,\phi)} = \sum_{ij} Q_{ij}^{(1)} \left[\gamma_{1x} \frac{\partial B_i}{\partial x} \frac{\partial B_j}{\partial x} + \gamma_{1y} \frac{\partial B_i}{\partial y} \frac{\partial B_j}{\partial y} \right] \tag{2.25}$$

where γ_{1x} and γ_{1y} are the prefactors related to the gradient in the x- and y-direction respectively, and determined by experimental parameters as follows: for the UD model

$$\gamma_{1x} = \gamma_{1y} = (\frac{\mu_B}{\hbar})^2 (\frac{q}{mw_{orb}^2})^2 \frac{\rho_v p_0^2}{576\pi\epsilon_0^2} \left(\frac{1}{l^3} - \frac{1}{d^3} \right) \frac{2\tau}{1+\omega_{op}\tau}, \tag{2.26}$$

and for the UT model

$$\begin{aligned} \gamma_{1x} &= (\frac{\mu_B}{\hbar})^2 (\frac{q}{mw_{orb}^2})^2 \frac{(9\pi+6)\rho_a p_0^2}{512\pi^2\epsilon_0^2 d^4} \frac{2\tau}{1+\omega_{op}\tau}, \\ \gamma_{1y} &= (\frac{\mu_B}{\hbar})^2 (\frac{q}{mw_{orb}^2})^2 \frac{(9\pi-6)\rho_a p_0^2}{512\pi^2\epsilon_0^2 d^4} \frac{2\tau}{1+\omega_{op}\tau}. \end{aligned} \tag{2.27}$$

The simulation results of $T_1^{(x)}$ are 6.50×10^9 s for the UD model and 1.72×10^{10} s for the UT model with the fitted volume and areal densities respectively.

In the experiment, T_1 of the device is in the order of 1 s. From the results above, we conclude that charge noise is not important for spin relaxation in the single-qubit system considered here. To exclude phonon relaxation we need to stipulate for the moment that the applied magnetic field strength is less than about 1 T. This leaves EWJN as the dominant mechanism.

2.9.2 Relaxation time from evanescent-wave Johnson noise

The calculation of T_1 of a spin qubit affected by evanescent-wave Johnson noise need to take into account both direct magnetic noise $\mathbf{B}(t)$ and indirect magnetic noise $\mathbf{B}^{(E)}$ due to the electrically-induced motion of the qubit in the magnetic field gradient. The correlation function of effective noise magnetic field $\mathbf{B}^{(\mathrm{eff})}$ can be expanded as

$$\begin{aligned}\langle B_i^{(\mathrm{eff})} B_j^{(\mathrm{eff})}\rangle &= \langle (B_i + B_i^{(E)})(B_j + B_j^{(E)})\rangle \\ &= \langle B_i B_j\rangle + \langle B_i B_j^{(E)}\rangle + \langle B_i^{(E)} B_j\rangle + \langle B_i^{(E)} B_j^{(E)}\rangle \\ &= \langle B_i B_j\rangle + \sum_{m,n}\left[\frac{q^2}{k_m k_n}\frac{\partial B_i}{\partial x_m}\frac{\partial B_j}{\partial x_n}\langle E_m E_n\rangle\right. \\ &\quad \left. + \frac{q}{k_m}\frac{\partial B_j}{\partial x_m}\langle B_i E_m\rangle + \frac{q}{k_n}\frac{\partial B_i}{\partial x_n}\langle E_n B_j\rangle\right].\end{aligned} \tag{2.28}$$

Using Eqs. 2.7 and 2.8 for the dynamics of $B_i^{(E)}(t)$ and assuming that there is no correlation between $B_i(t)$ and $B_i^{(E)}(t)$, we arrive at the correlation functions for the effective magnetic field:

$$\begin{aligned}
\langle B_x^{(\mathrm{eff})} B_x^{(\mathrm{eff})}\rangle &= \langle B_x B_x\rangle + (\frac{q}{m\omega_{orb}^2})^2 \left\{ (\frac{\partial B_x}{\partial x})^2 \langle E_x E_x\rangle + (\frac{\partial B_x}{\partial y})^2 \langle E_y E_y\rangle \right\} \\
&= \left[\frac{\mu_0 \hbar\omega_{op}\sigma w}{16 d^2} + (\frac{q}{m\omega_{orb}^2})^2 \frac{\hbar\omega_{op}\epsilon_d\epsilon_0}{4\sigma d^3} \left\{ (\frac{\partial B_x}{\partial x})^2 + (\frac{\partial B_x}{\partial y})^2 \right\} \right] \coth \frac{\hbar\omega_{op}}{2k_B T}, \\
\langle B_y^{(\mathrm{eff})} B_y^{(\mathrm{eff})}\rangle &= \langle B_y B_y\rangle + (\frac{q}{m\omega_{orb}^2})^2 \left\{ (\frac{\partial B_y}{\partial x})^2 \langle E_x E_x\rangle + (\frac{\partial B_y}{\partial y})^2 \langle E_y E_y\rangle \right\} \\
&= \left[\frac{\mu_0 \hbar\omega_{op}\sigma w}{16 d^2} + (\frac{q}{m\omega_{orb}^2})^2 \frac{\hbar\omega_{op}\epsilon_d\epsilon_0}{4\sigma d^3} \left\{ (\frac{\partial B_y}{\partial x})^2 + (\frac{\partial B_y}{\partial y})^2 \right\} \right] \coth \frac{\hbar\omega_{op}}{2k_B T}, \\
\langle B_z^{(\mathrm{eff})} B_z^{(\mathrm{eff})}\rangle &= \langle B_z B_z\rangle + (\frac{q}{m\omega_{orb}^2})^2 \left\{ (\frac{\partial B_z}{\partial x})^2 \langle E_x E_x\rangle + (\frac{\partial B_z}{\partial y})^2 \langle E_y E_y\rangle \right\} \\
&= \left[\frac{\mu_0 \hbar\omega_{op}\sigma w}{8 d^2} + (\frac{q}{m\omega_{orb}^2})^2 \frac{\hbar\omega_{op}\epsilon_d\epsilon_0}{4\sigma d^3} \left\{ (\frac{\partial B_z}{\partial x})^2 + (\frac{\partial B_z}{\partial y})^2 \right\} \right] \coth \frac{\hbar\omega_{op}}{2k_B T},
\end{aligned} \tag{2.29}$$

while the terms $\langle B_i^{(\mathrm{eff})} B_j^{(\mathrm{eff})}\rangle$ with $i \neq j$ are

$$\langle B_i^{(\mathrm{eff})} B_j^{(\mathrm{eff})}\rangle = (\frac{q}{m\omega_{orb}^2})^2 \frac{\hbar\omega_{op}\epsilon_d\epsilon_0}{4\sigma d^3} \left\{ \frac{\partial B_i}{\partial x}\frac{\partial B_j}{\partial x} + \frac{\partial B_i}{\partial y}\frac{\partial B_j}{\partial y} \right\} \coth \frac{\hbar\omega_{op}}{2k_B T}. \tag{2.30}$$

Substituting Eqs. 2.19 and 2.20 for the EWJN into equation of this kind, and applying Eq. 2.3 to rotate the results into a general direction, we arrive at Eqs. 2.31 and 2.32 from which the results in Fig. 2.3 are calculated. Eqs. 2.19 and 2.20 themselves are the half-space local (point qubit) correlation functions for EWJN [45]. They are valid only in the $d \ll \delta$ regime. The distance d between the qubit and accumulation gates is about 137 nm while skin depth $\delta = \sqrt{2/\mu_0\sigma\omega_{op}} = 313\,\mathrm{nm}$ with the conductivity of gates estimated very roughly as $\sigma = 2 \times 10^8\,\mathrm{S/m}$ [84] and the operating frequency $\omega_{op} = 2\pi \times 12.9\,\mathrm{GHz} = 8.11 \times 10^{10}\,\mathrm{s}^{-1}$. Thus the device parameters satisfy the $d \ll \delta$ requirement.

The relaxation rate with applied magnetic field direction in (θ, ϕ) for EWJN can

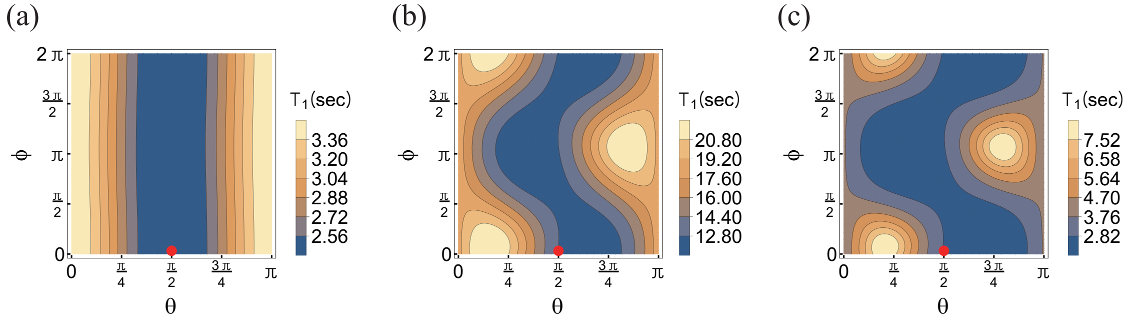

Figure 2.3: The anisotropy maps of relaxation time T_1. x and y axis are the polar angle θ and the azimuthal angle ϕ with respect to the device's z-direction, respectively. The conductivity of gates are **(a)** $\sigma = 2 \times 10^8\,\mathrm{S/m}$, **(b)** $\sigma = 2 \times 10^7\,\mathrm{S/m}$, and **(c)** $\sigma = 2 \times 10^6\,\mathrm{S/m}$. The applied field direction $(\theta, \phi) = (\pi/2, 0)$ used in the experiment is indicated by red dot.

be written as

$$\frac{1}{T_1(\theta,\phi)} = \alpha + \beta \sum_{ij} Q_{ij}^{(1)} \left[\frac{\partial B_i}{\partial x}\frac{\partial B_j}{\partial x} + \frac{\partial B_i}{\partial y}\frac{\partial B_j}{\partial y} \right] \tag{2.31}$$

where

$$\begin{aligned} \alpha &\equiv \frac{\hbar\omega_{op}\mu_0\sigma w}{4d^2} \coth\frac{\hbar\omega_{op}}{2k_BT}, \\ \beta &\equiv \left(\frac{q}{m\omega_{orb}^2}\right)^2 \frac{\hbar\omega_{op}\epsilon_d\epsilon_0}{4\sigma d^3} \coth\frac{\hbar\omega_{op}}{2k_BT}. \end{aligned} \tag{2.32}$$

The first term represents the direct effect of noise magnetic field while the second term is due to the noise electric field that is converted to effective noise magnetic field by the field gradients created by the micromagnets. The angular variation in $Q_{ij}^{(1)}$ and the rather anisotropic character of the magnetic field gradients imply that the anisotropy of T_1 will be intensified when the electric term is bigger than the direct magnetic term. Noting that $\alpha \sim \sigma$ and $\beta \sim 1/\sigma$, we see that varying σ will change the anisotropy pattern of T_1. As mentioned earlier, σ was not measured in the experiment and it makes sense to vary it to investigate the angular dependence of T_1.

The anisotropy map of T_1 is shown in Fig. 2.3 with (a) $\sigma = 2 \times 10^8\,\mathrm{S/m}$, (b)

$\sigma = 2 \times 10^7\,\mathrm{S/m}$, and (c) $\sigma = 2 \times 10^6\,\mathrm{S/m}$. The anisotropy pattern in Fig. 2.3(a) is fairly simple because the magnetic noise is dominant and the direct magnetic EWJN itself is not very anisotropic, as can be seen from Eq. 2.20 and the text following it. The anisotropy is increased as shown in Fig. 2.3(b) where the magnetic noise is more comparable to the electric noise. The anisotropy becomes even larger in Fig. 2.3(c) where the magnetic noise is one order of magnitude smaller than the electric noise. This pattern looks like the reversal of the anisotropy map of T_2 in Fig. 2.2(a) and Fig. 2.2(b). This is natural since T_2 of a spin qubit is due to longitudinal noise while T_1 is due to transverse noise. From practical point of view, the qubit performance would be improved when the applied field direction is set to the angles that give maximal T_2 (in the case of $T_\phi \ll T_1$).

When the strength of the applied magnetic field is increased, there is a crossover from EWJN- to phonon-dominated spin relaxation. The anisotropy maps for phonon interaction was worked out in Ref. [42]. They are determined by the orientation of the field relative to the crystal axes, not axes coming from the the device geometry. Hence we expect sharp changes in the anisotropy map as the field is increased beyond about 3 T.

2.10 Discussion

The anisotropy pattern for the decoherence time of a spin qubit comes from the combination of the magnetic field gradient and the noise electric field, the latter being determined by the configuration of noise dipoles. By introducing a vector magnet in a quantum dot device, noise characteristics such as noise dipole type and/or spatial distribution of noise dipoles can be experimentally investigated. Another way to obtain similar information is to exploit a controllable magnetic field gradient for a spin qubit on a nitrogen vacancy center in a diamond [95, 96]. In this case, the gradient can be varied instead of the direction of applied magnetic field to study noise characteristics.

The anisotropy pattern for relaxation time can be explained by a combination of direct magnetic noise and indirect electric noise. The magnetic noise part resulting from EWJN is isotropic in the $x - y$ plane in typical device structures. The electric noise is mediated by magnetic field gradients, which is the only source of anisotropy. As a result, the anisotropy gets bigger as the influence of the electric noise part increases.

To summarize, we have shown anisotropy in relaxation times and decoherence times using device parameters taken from quantum dot of Kawakami *et al.* Making the anisotropy map can help to understand the noise mechanisms. Specifically, this will benefit the understanding of solid state quantum processors where the causes of noise are still being investigated. Our work contributes to science in the noisy intermediate-scale quantum era by suggesting a new experimental method for noise characterization of spin qubit devices [97].

Chapter 3

Driving charge noise sources

3.1 Preliminary concepts

3.1.1 Brief review on noise source driving

To reduce the effect of $1/f$ noise, several experimental techniques have been proposed. By far the best known is dynamical decoupling that compensates accumulated phase error by applying refocusing pulses to a qubit [98]. This can substantially increase dephasing time of the qubit. It is not always practical, however, since it involves extensive additional manipulation of the qubit.

A quite different approach that is actively being studied in various contexts is driving the environment of the qubits, which we dub noise source driving (NSD). One example of NSD is spin bath driving that has shown to be useful for nitrogen-vacancy (NV) spin qubits in diamonds. This scheme applies a radio-frequency pulse or continuous wave to surface spins in the diamonds, giving rise to decoupling of dipolar interaction to the NV spin qubits [99, 100]. The consequence of the spin bath driving is manifested by the shift of noise power spectral density (PSD) from low to high frequencies, which increases the dephasing times [101, 102]. Recent experiments show that it works well with both monochromatic and polychromatic driving fields [103]. This method is somewhat analogous to dynamical decoupling but it has the advantage that one does not manipulate the qubits - the carriers of quantum information - but rather the noise sources, which carry no useful information for quantum computing.

Another NSD scheme for superconducting qubits has also been proposed. Theoretical study shows that the coherence times of a superconducting qubit can be increased by adding noise to the surrounding two-level systems (TLS) [104]. It is noteworthy that the relaxation (decoherence) time of the qubit is closely related to the decoherence (relaxation) of the TLSs. An experimental study exhibits 23% increase in the relaxation time of a transmon qubit on average when dc electric field is applied to the TLSs [105].

In comparison to those studies listed above, the NSD for qubits in quantum dot devices is still lacking. The noise sources in diamonds are exactly known, so the situation is different from that in semiconductor qubits. The studies for superconducting qubits could be applied to the quantum dot devices because they suffer from similar $1/f$ noise. Nevertheless, more detailed study specific to the devices is called for with various theoretical settings and experimental parameters.

3.1.2 Stochastic resonance

Noise source driving for TLSs can be considered in terms of stochastic resonance which was vigorously studied decades ago. Stochastic resonance is a phenomenon in which a particle moving back and forth randomly in a bistable potential is partially synchronized with external periodic signal (typically, oscillating electromagnetic field) [106]. It is not strictly resonance with natural frequency of the system, but it is useful in analogy to accept the concept of resonance because the signal-to-noise ratio (SNR) is maximized when certain condition is met.

The theory of stochastic resonance was developed in detail in weak-field limit [107] and strong-field limit [108, 109]. A more general approach that is independent of external signal strength was also studied [110]. Quantum stochastic resonance where a spin-boson model is adopted instead of classical particle in bistable potential was examined [111, 112]. In recent years quantum stochastic resonance was observed experimentally in the tunneling process of electrons in a quantum dot [113] and in the spin dynamics of a single Fe atom under scanning tunneling microscope [114]. It is important to note that the SNR of a TLS is maximized when driving frequency is about half of the switching rate of the TLS [106].

3.1.3 Parseval's theorem for TLS

Parseval's theorem states that the Fourier transform is unitary; specifically for time and frequency domains, it can be expressed as

$$\int_{-\infty}^{\infty} |x(t)|^2 \, dt = \frac{1}{2\pi} \int_{-\infty}^{\infty} |X(\omega)|^2 \, d\omega \tag{3.1}$$

where $X(\omega)$ is the Fourier transform of $x(t)$. In physical sense, it is equivalent to the statement that the total energies computed in time and frequency domain must be equal.

Parseval's theorem is the core of NSD for TLSs. Since a TLS can take $x(t) = \pm c$ with some constant c, the total noise power of the TLS ($\int |X(\omega)|^2 \, d\omega$) in a time period T is $c^2 T$. This implies that altering the dynamics of the TLS will not increase the noise power.

3.2 Motivation and outline

In this chapter, one motivation is to increase qubit dephasing times by mitigating the effects of noise. This is achieved by applying an oscillating electric field to the charge noise sources that contribute to $1/f$ noise. This gives noise at frequencies near the driving frequency, which can be chosen to be relatively high. Assuming the sources are TLSs, Parseval's theorem says that the total noise power is conserved so that the noise at low frequencies is suppressed. This generally increases dephasing time (T_ϕ). Depending on details, the shift could also affect the relaxation time (T_1), which is inversely proportional to the noise power at the operating frequency of a qubit. However, the main focus here will be on T_ϕ. For spin and most other qubits decoherence time $T_2 \ll T_1$ and it is therefore the limiting factor for qubit operation. In this limit one generally has $T_2 \approx T_\phi$.

Since the origin of $1/f$ noise is not well known, we need to assume and model the charge noise sources. We will use a rather generic model of a single TLS and compute its consequences for T_ϕ. We then investigate the effects of multiple TLSs and how they depend on the parameters of a double-well potential for a single TLS. This gives a second motivation for our work. Driving qubits can affect the noise PSD in ways that reveal the physical nature of the TLSs. Since qubits can be used as spectrometers [115], we can hope to combine NSD and qubit spectroscopy to gain insight into the physical nature of the TLSs.

To make our model of the TLS as general as possible, we include the possibility that it is a quantum object in the sense that coherent superpositions of the two levels are allowed. We keep in mind the usual assumption that a double-well potential is involved. The usual effectively classical TLS may be recovered when the dephasing rate is much larger than other parameters that impact its dynamics. This limit can also be compared with the well-established theory of stochastic resonance.

In Sec. 3.3, the model for quantum TLS is introduced and we discuss the meaning of the parameters in the model. In Sec. 3.4 we compute the shift in the noise PSD for a single TLS due to the driving and its consequences for the qubit dephasing times. In Sec. 3.5 we extend this to multiple noise sources. We deal with special cases where the driving field resonates with a single TLS in Sec. 3.6. Finally we discuss the question of how much light the driving experiments can throw on the nature of the noise sources in Sec. 3.8.

3.3 Model for noise sources

We provisionally view the TLS as having some quantum character. This means that a single TLS is an open quantum system whose dynamics are described by the Lindblad equation:

$$\frac{d\rho}{dt} = -i[H,\rho] + \sum_j \left(L_j \rho L_j^\dagger - \frac{1}{2}\left\{ L_j^\dagger L_j, \rho \right\} \right) \tag{3.2}$$

where ρ is the density matrix for the TLS and $\hbar = 1$.

The Hamiltonian is

$$H = \frac{1}{2}(\epsilon\sigma_z + \Delta\sigma_x) + (\alpha_z\sigma_z + \alpha_x\sigma_x)\cos\omega_d t \tag{3.3}$$

where ϵ is the energy difference between the two levels, Δ is the tunneling amplitude, α_z and α_x are the driving strength for z and x basis of the TLS respectively, and ω_d is the driving frequency. α_z is the strength of the dipole moment times the parallel component of the driving electric field. α_x represents the strength of the field component that modulates the tunneling. The Lindblad operators are

$$L_1 = \sqrt{\gamma} \begin{pmatrix} 0 & 1 \\ 0 & 0 \end{pmatrix}, \, L_2 = \sqrt{\kappa} \begin{pmatrix} 0 & 0 \\ 1 & 0 \end{pmatrix}, \, L_3 = \sqrt{\eta} \begin{pmatrix} 1 & 0 \\ 0 & -1 \end{pmatrix} \tag{3.4}$$

where γ, κ, and η denote relaxation, excitation, and pure dephasing rate, respectively. Note that all the parameters are in the units of Hz and ϵ has negative value assuming $|0\rangle$ and $|1\rangle$ are ground and excited state respectively.

We now change to variables whose physical meaning is more transparent. The "spin" $s_z(t) = \rho_{00}(t) - \rho_{11}(t)$ is proportional to the dipole moment, whose fluctuations produce the noise. The off-diagonal asymmetry is $p(t) = \rho_{01}(t) - \rho_{10}(t)$ and $q(t) = \rho_{01}(t) + \rho_{10}(t)$ is a phase measure. We also define the total relaxation rate: $\Gamma = (\gamma + \kappa)/2$, and the relative rate: $\lambda = \gamma - \kappa$. We apply a detailed balance condition to get a relation between γ and κ, which is $\lambda = 2\Gamma \tanh(\epsilon/2k_BT)$.

Changing to these variables, we get the following coupled differential equations from the Lindblad equation:

$$\begin{aligned} \frac{ds_z(t)}{dt} &= -2\Gamma s_z(t) + \lambda - (\Delta + 2\alpha_x \cos\omega_d t)p(t) \\ \frac{dp(t)}{dt} &= (\Delta + 2\alpha_x \cos\omega_d t)s_z(t) \\ &\quad - (\Gamma + 2\eta)p(t) - (\epsilon + 2\alpha_z \cos\omega_d t)q(t) \\ \frac{dq(t)}{dt} &= (\epsilon + 2\alpha_z \cos\omega_d t)p(t) - (\Gamma + 2\eta)q(t). \end{aligned} \tag{3.5}$$

Since no closed-form solutions are known to exist for these equations, we solve them numerically. One may refer to Ref. [116] for analytic method describing the dynamics of a TLS under strong driving field.

The focus is on $s_z(t)$ because it is proportional to the electric dipole moment produced by the TLS. Since $s_z(t) = \langle\sigma_z\rangle = \mathrm{Tr}[\rho(t)\sigma_z]$ is an expectation value, the correlation function for time duration τ can be regarded as $\pm s_z(\tau)$ depending on the initial state, $|0\rangle$ or $|1\rangle$, of an ensemble. We are going to deal with ϵ much smaller than k_BT, the initial state is fixed to $|0\rangle$ for numerical simulations. With some coupling constant C_0 that depends on the geometry in the device and the species of the qubit, the PSD in the electric field that the qubit experiences can be written as $S(\omega) = C_0 \int s_z(\tau)e^{-i\omega\tau}d\tau$. Therefore, we will look into the changes in $S(\omega)$ and T_ϕ caused by the driving field. To compute $S(\omega)$ we solve Eq. 3.5 numerically and then use fast Fourier transform for $s_z(t)$. In practice, $s_z(t)$ is sampled with frequency $f_s = 10^4$ Hz for total simulation time $T_m = 10^2$ s for a single TLS and $f_s = 10^3$ Hz for $T_m = 10^3$ s for multiple TLSs. This is sufficient for our purposes since we will only look at the changes in $S(\omega)$ for $\omega < f_s$.

3.4 PSD and dephasing time of a single TLS

The basic ideas of this work are already present at the single TLS level, which is the subject of this section. The parameters used are temperature $T = 0.1$ K, $\Gamma = 1$ Hz, $\eta = 1$ Hz, $\alpha_x = 0.5\alpha_z$, $\Delta = 0$ Hz, and $\epsilon = 0$ Hz.

The reasons for choosing such values are as follows: $T = 0.1$ K is a widely used experimental temperature. $\Gamma = 1$ Hz represents a typical low frequency fluctuator.

η for low frequency TLSs is not known experimentally, so its value is chosen to have similar order of magnitude as Γ. This follows the studies on high frequency TLSs having similar or a few orders of magnitude smaller η than Γ [117, 118]. If η is larger than Γ, the dynamics without driving is dominated by dephasing process.

α_x is much more important than α_z; there will be no driving effect if $\alpha_x \ll \alpha_z$. It is shown that α_x is smaller than α_z in the case of double well potential (see Sec. 3.7 for detail), but how much smaller depends on the coupling nature of the TLS to an

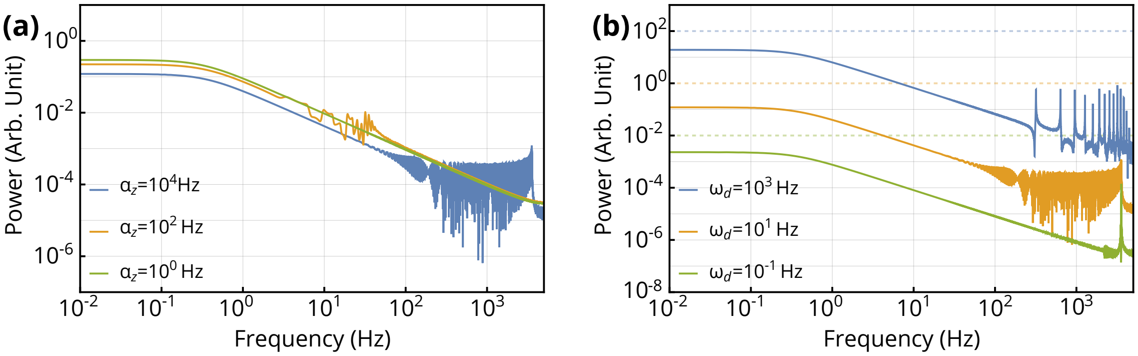

Figure 3.1: **(a)** Shift of PSD for a single TLS varying α_z with fixed $\omega_d = 10^1$ Hz. These PSDs correspond to the three simulation points along the vertical axis in Fig. 3.2. **(b)** Shift of PSD for a single TLS varying ω_d with fixed $\alpha_z = 10^4$ Hz. These PSDs are offset by 2 orders of magnitude for clarity and correspond to the three simulation points along the horizontal axis in Fig. 3.2. Color-coded dashed lines mean the offset power at $\omega = 10^{-2}$ Hz when driving field is not applied.

external electric field. Thus, we take $\alpha_x = 0.5\alpha_z$ for now. Δ is set to be zero since coherent oscillation is hard to find in noise PSD.

We assume $\epsilon = 0$ which means that the TLS is symmetrical. ϵ can take values other than zero and affect the relative rate λ. Driving has no effect when $\alpha_x \ll \epsilon$. This sets the basic scale for the strength of the driving field. There is a coherent regime where ϵ is larger than other parameters. In this case, damped Rabi oscillation can occur when $\omega_d \approx \epsilon$ which yields a significant increase in T_ϕ, which we will present in Sec. 3.6.

The point of our study is that the PSD of the TLS, which is a Lorentzian, can be shifted when it is driven. The shift is towards higher frequencies, and it is a function of both the driving strength and the driving frequency as shown in Fig. 3.1 (a) and (b). The increase in the shift as a function of driving strength is of course expected, and it is mainly limited by practical considerations. The frequency dependence is more interesting. The shift initially increases with frequency as the TLS attempts to follow the driving frequency, in somewhat the same fashion as a driven harmonic oscillator. However, as the driving frequency continues to increase,

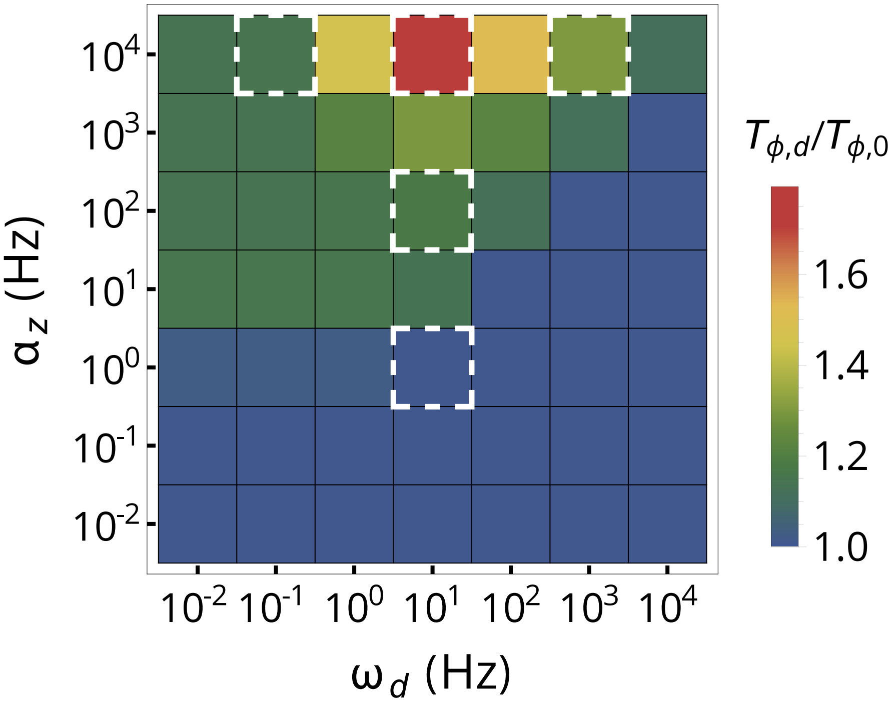

Figure 3.2: Increase in dephasing time of a qubit when a single TLS is driven by the oscillating electric field with strength α_z and frequency ω_d. The dephasing time with driving field ($T_{\phi,d}$) is divided by that without driving field ($T_{\phi,0}$). Only 49 values of $T_{\phi,d}/T_{\phi,0}$ with the combination of 7 different strengths (10^{-2}-10^4 Hz) and frequencies (10^{-2}-10^4 Hz) are shown. White dashed boxes are the simulation points used in Fig. 3.1.

the force averages out and the effects decrease. This phenomenology is very similar to that seen in classical stochastic resonance.

Any change in $S(\omega)$ will be reflected in the dephasing time T_ϕ of nearby qubit, defined by the formulas, Eqs. 1.7, 1.8, and 1.9. This allows us to compute T_ϕ again as a function of driving strength and frequency. To see the effects of driving, we compute the ratio of $T_{\phi,d}$, the dephasing time with driving, to $T_{\phi,0}$, that in the absence of driving.

The overall coupling strength C_0 is arbitrary in this chapter, since our interest is in the general phenomenon of suppression of decoherence. However, to give an idea of experimentally relevant parameters, if we take a coupling strength $C_0 = 10^{12}$ Hz^2, we will find $T_{\phi,0} = 1.00$ µs, a typical value in spin qubit experiments. In the simulations in Fig. 3.2, $C_0 = 1$ Hz^2 is used, resulting in $T_{\phi,0} = 2.31$ s. To have significant increase in T_ϕ, it is critical to choose C_0 so that the PSD is shifted over the dephasing rate without driving, $\omega > 1/T_{\phi,0}$.

As shown in Fig. 3.2, increase in T_ϕ when applying driving field is most effective when $\alpha_z > \omega_d > \Gamma$, giving increasing factor up to 1.79. There is no improvement in T_ϕ when $\alpha_z < \Gamma$ or $\alpha_z < \omega_d$. This is in accord with the changes in $S(\omega)$ discussed above: the time scale of the driving strength should be shorter than the average relaxation time of the TLS to see the maximum effect but very much shorter time scales will cause the driving effect to cancel out.

3.5 PSD and dephasing time of multiple TLSs

We now consider a more realistic model of a qubit in an actual device. There are many TLSs acting in an incoherent fashion on the qubit, giving rise to $1/f$ noise. Rather surprisingly, it turns out that if we choose a log-uniform distribution of

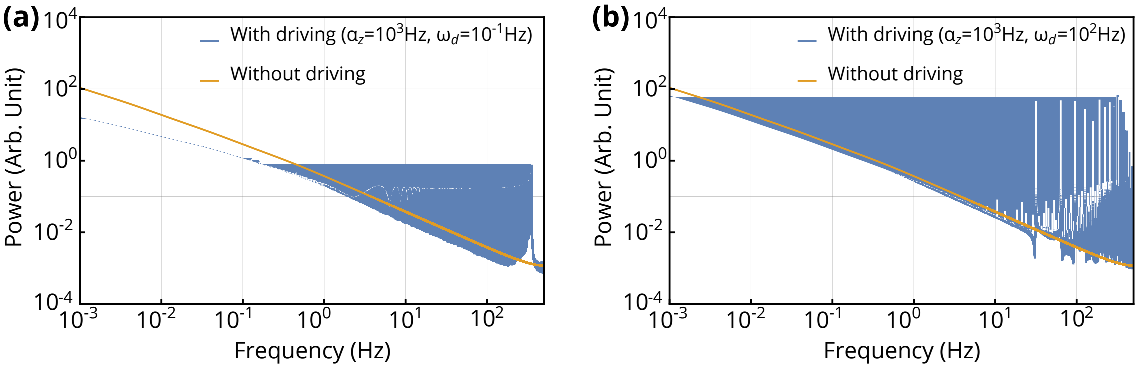

Figure 3.3: **(a)** and **(b)** Shift of PSD for multiple TLSs as varying ω_d with fixed $\alpha_z = 10^3$ Hz. These PSDs correspond to the two simulation points in Fig. 3.4, respectively.

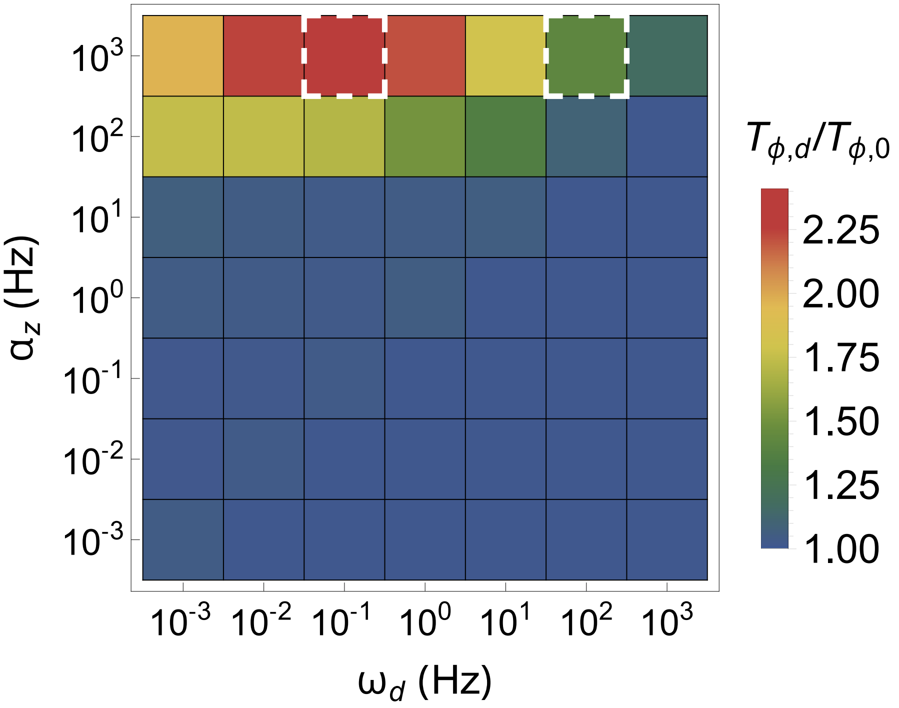

Figure 3.4: Increase in dephasing time of a qubit when multiple TLSs are driven by the oscillating electric field with strength α_z and frequency ω_d. The dephasing time with driving field ($T_{\phi,d}$) is divided by that without driving field ($T_{\phi,0}$). Only 49 values of $T_{\phi,d}/T_{\phi,0}$ with the combination of 7 different strengths (10^{-3}-10^3 Hz) and frequencies (10^{-3}-10^3 Hz) are shown. White dashed boxes are the simulation points used in Fig. 3.3.

Lorentzian widths, only one TLS per frequency decade is required to give a 1/f spectrum quite accurately. Motivated by this and computational convenience, we use 7 TLSs in this section. Γ and η of the TLSs are set to equal and range from 10^{-6} Hz to 1 Hz log-uniformly. Other parameters are set to those used in the Sec. 3.4 unless otherwise noted. Each is simulated using the same method as above, and the individual power spectra $S_i(\omega)$ are added to give the total PSD, $S(\omega) = \sum_i S_i(\omega)$, which then yields the fluctuating field at the qubit as in the previous section.

In Fig. 3.3 we plot the total PSDs with fixed driving strength and two different driving frequencies. As can be seen, the changes in the spectrum are more subtle than in the single TLS case. The spectrum can be moved to higher frequencies, but only in a limited range. This is a consequence of the fact that for the driving to have an effect there needs to be an approximate match between the switching rate of the TLSs and the driving frequency. This cannot be achieved if the noise is broadband and there is only a single driving frequency. It may be possible to do better using non-monochromatic driving, but we do not pursue this here.

The result for increased dephasing time due to 7 TLSs is given in Fig. 3.4. We see a qualitatively similar effect to that in Fig. 3.2, but find the maximum increasing factor in T_ϕ to be about 2.43 with $\alpha_z = 10^3$ Hz and $\omega_d = 10^{-1}$ Hz. This is quite intriguing because ω_d is smaller than $1/T_{\phi,0} = 2.27$ Hz and inside the noise bandwidth ($10^{-6} - 1$ Hz). In practical cases, an optimal driving frequency should exist for given $1/f$-like noise spectrum.

3.6 Damped Rabi oscillation

When the energy difference of a TLS, ϵ, is larger than other parameters, especially Γ and η, it is possible to drive the TLS coherently (still dealing with the regime,

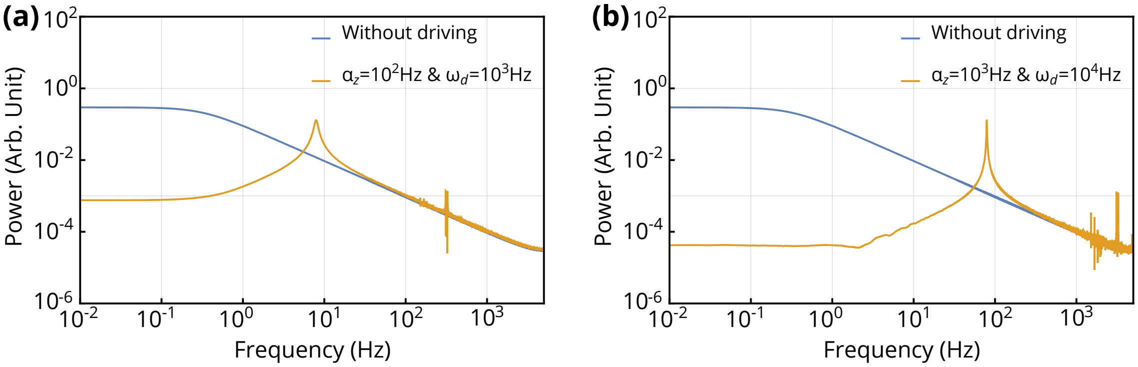

Figure 3.5: Shift of PSD for single TLS with **(a)** $\epsilon = 10^3$ Hz and **(b)** $\epsilon = 10^4$ Hz. These PSDs correspond to the two simulation points in Fig. 3.6, respectively.

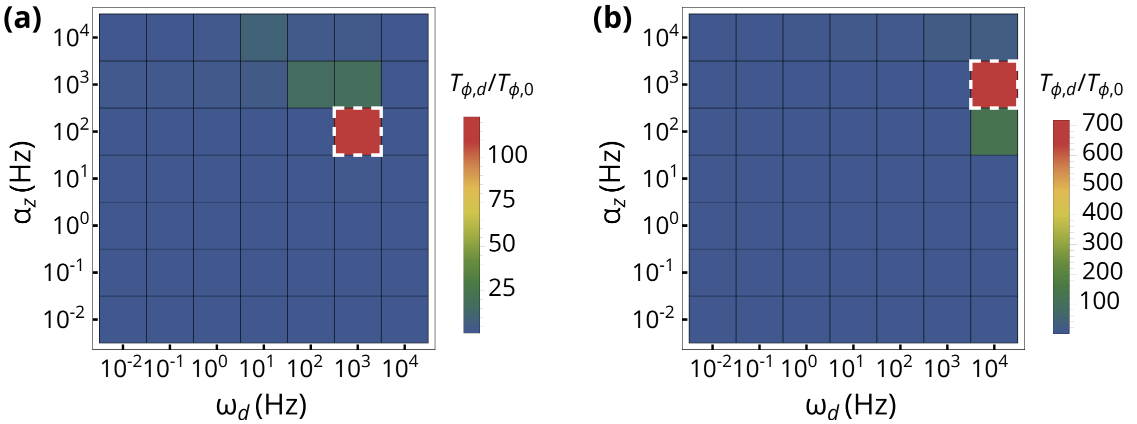

Figure 3.6: Increase in dephasing time of a qubit with **(a)** $\epsilon = 10^3$ Hz and **(b)** $\epsilon = 10^4$ Hz when a single TLS is driven by the oscillating electric field with strength α_z and frequency ω_d. The dephasing time with driving field ($T_{\phi,d}$) is divided by that without driving field ($T_{\phi,0}$). Only 49 values of $T_{\phi,d}/T_{\phi,0}$ with the combination of 7 different strengths (10^{-2}-10^4 Hz) and frequencies (10^{-2}-10^4 Hz) are shown. White dashed boxes are the simulation points used in Fig. 3.5.

$\epsilon \ll k_B T$). The PSDs in Fig. 3.5, for example, show extremely huge reduction at low frequencies for $\epsilon = 10^3$ Hz and $\epsilon = 10^4$ Hz, respectively. The reduced parts are shifted to higher frequencies as conspicuous peaks in the middle of the frequency range. Other parameters used in these simulations are those in Sec. 3.4 while α_z (also, $\alpha_x = 0.5\alpha_z$) and ω_d are chosen so that the shifts of PSDs are large. This is not similar to the cases in Sec. 3.4 where stochastic resonant behavior is observed around $\omega_d \sim \Gamma$, but more analogous to damped Rabi oscillation where the TLS resonantly interacts with the applied electric field by emitting and absorbing photons at $\omega_d = \epsilon$.

The increases in T_ϕ with varying α_z and ω_d are presented in Fig. 3.6 for $\epsilon = 10^3$ Hz and $\epsilon = 10^4$ Hz, respectively. The maximum values are 123 and 718 for the simulations points used in Fig. 3.5. One interesting observation is that it seems to have specific resonant condition for α_z as well as ω_d. This might be interpreted as saturation effect where the power absorbed by the TLS is saturated [119]. Detailed study on the resonant behavior of the TLS in terms of damped Rabi oscillation was conducted with Bloch-Redfield equations [120]. In the literature, the shift of PSD from low to high frequencies is predicted analytically by adopting rotating-wave approximation which is valid only for near resonance condition. This is less general than our theoretical approach, but can complement our results specifically for high-frequency TLSs that are important for T_1 of a qubit.

3.7 Realistic conditions for driving noise sources

Suppose that there is a double well potential whose localized states are given as $|L\rangle$ and $|R\rangle$. If an electron is in the double well, its Hamiltonian is

$$H_q = \frac{\hbar}{2}(\epsilon\sigma_z + \Delta\sigma_x) \tag{3.6}$$

in the $\{|L\rangle, |R\rangle\}$ basis and $\hbar$ is explicitly expressed in this section. In the energy eigenbasis, it is simplified to

$$H_q = \frac{\hbar\Omega}{2}\sigma_z \tag{3.7}$$

where $\hbar\Omega = \hbar\sqrt{\epsilon^2 + \Delta^2}$. The Hamiltonian for interaction betwen the electron and electromagnetic field is

$$H_{int} = -\frac{e}{2m}(\mathbf{A}\cdot\mathbf{p} + \mathbf{p}\cdot\mathbf{A}) \tag{3.8}$$

where e and m are electron's charge and mass respectively, $\mathbf{p}$ is the momentum operator of the electron and $\mathbf{A}$ is the vector potential. A^2 term is ignored in the weak-field limit. The interaction Hamiltonian can be written in the energy eigenbasis [121]:

$$H_{int} = -\int d\mathbf{r}\,[\sigma_x \mathbf{M}_r(\mathbf{r}) + \sigma_z \mathbf{M}_\phi(\mathbf{r})]\cdot\mathbf{A}(\mathbf{r},t) \tag{3.9}$$

where

$$\begin{aligned} \mathbf{M}_r(\mathbf{r}) &= \frac{e}{2m}\left[2\psi_+^*(\mathbf{p}\psi_-) + \psi_+^*\psi_-\mathbf{p}\right], \\ \mathbf{M}_\phi(\mathbf{r}) &= \frac{e}{4m}\left[2\psi_+^*(\mathbf{p}\psi_+) + \psi_+^*\psi_+\mathbf{p} - 2\psi_-^*(\mathbf{p}\psi_-) - \psi_-^*\psi_-\mathbf{p}\right]. \end{aligned} \tag{3.10}$$

Here $\psi_\pm(\mathbf{r})$ are the wave functions for energy eigenstates and their corresponding ket vectors can be expressed in the superposition of $|L\rangle$ and $|R\rangle$ such that

$$|\pm\rangle = \frac{\epsilon_\pm}{\sqrt{\epsilon_\pm^2 + 1}}|L\rangle + \frac{1}{\sqrt{\epsilon_\pm^2 + 1}}|R\rangle \tag{3.11}$$

where $\epsilon_\pm = (\epsilon \pm \Omega)/\Delta$.

Let us choose Weyl gauge that electric potential is zero (thus, $\mathbf{E} = -\partial\mathbf{A}/\partial t$) and assume the vector potential takes plane-wave form $\mathbf{A}(\mathbf{r},t) = A_0\hat{\mathbf{v}}(e^{i(\mathbf{k}\cdot\mathbf{r}-\omega_d t)} + e^{-i(\mathbf{k}\cdot\mathbf{r}+\omega_d t)})/2$ where $\hat{\mathbf{v}}$ is the polarization unit vector. Electric field is then given as $\mathbf{E}(\mathbf{r},t) = i\omega A_0\hat{\mathbf{v}}(e^{i(\mathbf{k}\cdot\mathbf{r}-\omega_d t)} + e^{-i(\mathbf{k}\cdot\mathbf{r}+\omega_d t)})/2 \equiv E_0\hat{\mathbf{v}}(e^{i(\mathbf{k}\cdot\mathbf{r}-\omega_d t)} + e^{-i(\mathbf{k}\cdot\mathbf{r}+\omega_d t)})/2$. If the wavelength of the driving field is much longer than the size of the double well

$2a$, we can use electric dipole approximation that $e^{i\mathbf{k}\cdot\mathbf{r}} \approx 1$. Therefore, the driving strengths in the Lindblad equation are

$$\begin{aligned} \alpha_x &= i\frac{E_0}{\hbar\omega_d}\int d\mathbf{r}\,\mathbf{M}_r\cdot\hat{\mathbf{v}}, \\ \alpha_z &= i\frac{E_0}{\hbar\omega_d}\int d\mathbf{r}\,\mathbf{M}_\phi\cdot\hat{\mathbf{v}} \end{aligned} \tag{3.12}$$

where $H_{int} = \hbar(\alpha_z\sigma_z + \alpha_x\sigma_x)\cos\omega_d t$ is used. It has to be careful to evaluate the driving strengths since we have regarded the $\{|L\rangle, |R\rangle\}$ basis as the computational basis in the Lindblad equation. In such a case, $\mathbf{M}_r(\mathbf{r})$ and $\mathbf{M}_\phi(\mathbf{r})$ should be converted to the computational basis as follows:

$$\begin{aligned} \mathbf{M}_r(\mathbf{r}) &= \frac{e}{2m}\left[2\psi_L^*(\mathbf{p}\psi_R) + \psi_L^*\psi_R\mathbf{p}\right], \\ \mathbf{M}_\phi(\mathbf{r}) &= \frac{e}{4m}\left[2\psi_L^*(\mathbf{p}\psi_L) + \psi_L^*\psi_L\mathbf{p} - 2\psi_R^*(\mathbf{p}\psi_R) - \psi_R^*\psi_R\mathbf{p}\right]. \end{aligned} \tag{3.13}$$

To evaluate α_x and α_z, let us find out the localized wave functions ψ_L and ψ_R in one dimensional case. Assuming the Hamiltonian of the double well potential has quartic form $H = p^2/2m + ms(z^2 - a^2)^2$, expansion at each minimum ($z = \pm a$) results in the Hamiltonian of harmonic oscillator such as $H = p^2/2m + 4msa^2\xi^2$ where $\xi = z \mp a$. Here s is used to make the potential have the unit of energy and means steepness of the wells. By letting $4msa^2 = m\nu^2/2$, we can get the frequency of the harmonic oscillator $\nu = 2a\sqrt{2s}$. The localized ground state wave functions for the hamonic potential is Gaussian such as

$$\psi_{L,R}(z) = (\frac{m\nu}{\pi\hbar})^{1/4}\exp(-\frac{m\nu(z\pm a)^2}{2\hbar}). \tag{3.14}$$

Additionally introducing Coulomb gauge $\nabla\cdot\mathbf{A} = 0$, the driving strengths can be simplified as

$$\begin{aligned}\alpha_x &= i\frac{E_0}{\hbar\omega_d}\int dz\, M_r(z),\\ \alpha_z &= i\frac{E_0}{\hbar\omega_d}\int dz\, M_\phi(z),\end{aligned} \tag{3.15}$$

where

$$\begin{aligned}M_r(z) &= \frac{-i\hbar e}{2m}[2\psi_L^*\frac{\partial\psi_R}{\partial z}],\\ M_\phi(z) &= \frac{-i\hbar e}{4m}[2\psi_L^*\frac{\partial\psi_L}{\partial z} - 2\psi_R^*\frac{\partial\psi_R}{\partial z}].\end{aligned} \tag{3.16}$$

Plugging the Gaussian wave functions $\psi_{L,R}(z)$ into the above equations yields

$$\begin{aligned}\alpha_x &= \frac{2eE_0}{\hbar\omega_d}a^2\sqrt{2s}\,\exp(-\frac{2ma^3\sqrt{2s}}{\hbar}),\\ \alpha_z &= -\frac{2eE_0}{\hbar\omega_d}a^2\sqrt{2s}.\end{aligned} \tag{3.17}$$

Rearranging these equations with ν,

$$\begin{aligned}\alpha_x &= \frac{eE_0 a}{\hbar}\frac{\nu}{\omega_d}\,\exp(-\frac{ma^2\nu}{\hbar}),\\ \alpha_z &= -\frac{eE_0 a}{\hbar}\frac{\nu}{\omega_d}.\end{aligned} \tag{3.18}$$

This suggests $|\alpha_x| < |\alpha_z|$ in general, but for small a and ν where the wells are close to each other and the electron is loosely confined in the wells, $|\alpha_x| \approx |\alpha_z|$.

To check if the method can be implemented in quantum dot devices, let us examine its requirement with typical parameters used in the quantum dot devices. The requirement for effective driving of the TLSs is empirically obtained from the simulation with the Lindblad equation in Sec. 3.4:

$$\Gamma < \omega_d < |\alpha_z| \leq |\alpha_x|. \tag{3.19}$$

The first inequality can be readily satisfied if we adopt driving frequency more than 1 MHz. Since typical dephasing time T_ϕ of the qubit in Si/SiGe heterostructure is about 10^{-6} s, the important frequency part of the noise is less than 1 MHz. This value comes from the width of the center lobe of the squared sinc function that is included in the Eq. 1.9.

The unknown values are a and ν for which we need some guesswork. Let us take a to be in the order of 0.1 nm, which is the size of typical atoms. ν might vary for different TLSs and be related to Γ. However, it is possible to get a lower bound because we approximate the double well potential to a TLS, implying the kinetic energy of the electron is less than the potential barrier: $k_B T < V(0) = msa^4 = m\nu^2 a^2/8$. The result is $\nu > 10^{13}$ Hz when using electron temperature $T = 0.1$ K and electron's rest mass. The order of this lower bound will be modified slightly if we take into account electron's effective mass.

In addition to those values, let us take $\omega_d = 1$ GHz and $E_0 = 10$ V/m where typical gate voltage in the order of 100 mV, thickness of silicon chip of 1mm, and dielectric constant of 10 are assumed with parallel plate geometry. Since the relaxation time of typical dielectric is in the order of 10 ps, the polarization direction in a dielectric follows the oscillating electric field direction immediately, which can be regarded as dc limit. Driving frequency higher than 100 GHz will increase E_0 by reducing the cancellation of applied electric field due to polarization, but the maximum is about 100 V/m which is the value for vacuum (ac limit). Therefore, the second inequality can be satisfied with a lower bound $|\alpha_z| > 10$ GHz.

With COMSOL simulation, the electric field in aluminum oxide is about 8×10^6 V/m and that in SiGe spacer above 2D electron gas (2DEG) is about 5×10^6 V/m. These results are obtained with $4 \times 10^{11}\,\mathrm{cm}^{-2}$ fixed electron density of the 2DEG, 100 mV uniform top gate voltage, 35 nm SiGe spacer thickness, and 50 nm thickness aluminum oxide layer whose dielectric constant is 9. The estimated values for the electric field can be understood by assuming the reference point for ground is set to the 2DEG. Besides, E_0 can be controlled in a wide range by changing the gate voltage; the maximum gate voltage is about $1\,\mathrm{V}$ because of the breakdown in the case of aluminum oxide for overlapping gate layers [122]. It is also helpful to refer to the recent paper in which ac electric field amplitude in quantum dot array is estimated to be $10^2 - 10^3$ V/m [123].

The last inequality depends rather sensitively on the details of the double well potential since it contains the exponential factor $\exp(-ma^2\nu/\hbar)$. If this factor is much less than 1, then $|\alpha_x| \ll |\alpha_z|$ and the needed inequality is violated. However, this would mean that the tunneling matrix is extremely small, which would in turn imply that the TLS would not fluctuate in the first place. Hence we can be confident that except for extremely slow fluctuators, the theory remains valid.

3.8 Discussion

Driving the noise sources results in changes in the noise power spectrum and can suppress decoherence provided the physical condition presented in the previous section is satisfied. Observation of these effects can rule out some alternative models. One is classical damped harmonic oscillator coupled to thermal bath (see Appendix A. The Langevin equation can be used to calculate its dynamics and PSD. For this case the driving field actually produces additional noise and decoherence would worsen. This comes from the fact that the position of the charge is a continuous variable, and the driving field allows the system to access higher energy states. Suppression of decoherence by driving is a clear indication that the TLS is the right model.

Another model is a purely classical TLS where an electric dipole fluctuates in static and driving fields. This system is not exactly solvable when it undergoes

Poisson process while driving field is turned on. Hence it is appropriate to study stochastic resonance in the strong-field limit to see the driving effects since there is no enhancement in T_ϕ in the weak-field limit. This is ongoing study for this chapter.

The other model is quantum TLS which is the main result of our study. We can use spin-boson model in which the interaction between the TLS and thermal bath is well-defined [104]. However, the Lindblad equation seems to be general enough to encompass the spin-boson model because they are phenomenological equations that do not require detailed description of the environment of the TLS.

Future study might be needed for the whole system of a qubit plus TLSs because the qubit is usually composed of electrons or holes that are also modulated by the oscillating electric field at the same time with the TLSs. Dressed qubit protocol may be a useful tool for the study [124, 125].

Another point to discuss further would be that the qubit can affect the dynamics of the TLSs, which is neglected in our model. This is when the square root of realistic coupling constant, $\sqrt{C_0} \sim 10^6$ Hz, is comparable to or greater than other parameters [120]. The Gaussian approximation for Eq. 1.9 may not be valid in this strong coupling regime [49].

Chapter 4

Pulse-induced resonance frequency shift

4.1 Practical issues and key idea

There has been considerable progress in semiconductor quantum computing, with significant strides in scaling up and in gate fidelities [22, 30]. The chief difficulty is decoherence, with charge noise as the main culprit [126–134]. The precise nature of the two-level systems (TLS) that produce the noise remains elusive. There have been extensive characterizations of the noise spectrum [40, 57], and the spatial correlations in the noise [135–137] in different devices. These observations can advance the elucidation of the nature of the TLSs, but the data are not currently sufficient to pin things down precisely.

Another problem, at first sight quite separate, that interferes with qubit operation is pulse-induced resonance shift (PIRS). This is a shift in the operating frequency (Larmor frequency) of the qubits as a computation proceeds. This is highly problematic, since continual recalibration of the system is not practical. Quadrature control [76] and prepulsing [138] can mitigate, but not eliminate this issue. PIRS has recently received an intensive experimental study [123].

Here we propose that the source of PIRS and the source of charge noise are the same group of TLSs, and that detailed observations of PIRS can provide additional insight into their microscopic nature. We proceed in the time-honored fashion of proposing a phenomenological model that explains that data, and then seeing what constraints the model places on the underlying physics of the system.

4.2 General description of PIRS

Let us take a concrete situation in which the system is in a resting state at low temperature for times $t < 0$ and the operations, which involve microwave pulses that feed energy into the system, begin at $t = 0$ and end at some positive time, $t = t_f$. PIRS is a time-dependent shift $\Delta f(t)$ with $\Delta f(t = 0) = 0$ by definition. Δf is a function of time that ultimately reverts to the base state some time after the operations have ceased: $\Delta f(t = \infty) = 0$.

PIRS appears to be rather ubiquitous in semiconductor qubits, but there is considerable variability in how it manifests itself. Early observations found positive shifts ($\Delta f \geq 0$) of order a few MHz [138]. The magnitude of the shift was an increasing function of the energy injected by the pulses. It also depended on the details of the electron wavefunctions in the dots, for example on the dot occupations. The MHz magnitude of the shifts is fairly typical for quantum dot qubits. Importantly, Δf can also be negative [25, 76]. The decay time after t_f varies in the dot systems, with values from 0.5 ms [22] to 38 μs [25] having been observed. PIRS also occurs in donor-based qubit systems [139], though $|\Delta f|$ is much smaller, of order tens of kHz. Effects of a similar magnitude are seen in flip-flop qubits [20].

Our interpretation is based on the fact that dot and donor systems share the feature that the qubit operating frequency depends on the spatial position of the electron. The arbitrary sign of Δf then implies that a change in the electric field on the qubit is the origin of PIRS. Experimentally, it now appears to be clear that PIRS is essentially a thermal rather than a mechanical effect [22, 123]. This is also supported by the characteristic return to a base state, most naturally interpreted as a return to thermal equilibrium. The most striking feature of the results is that the magnitude of Δf is not monotonic in temperature T, instead rising to a maximum at about 250-300 mK, then decreasing.

4.3 Theoretical model

4.3.1 Model specification

To explain these observations, we introduce a model based on the charged TLSs that are known to exist in these devices, and that in fact are also responsible, at least in part, for the decoherence of the qubits. These charged defects or traps are modeled as a collection of N fluctuating electric dipoles. The jth dipole fluctuates between states $s_j \mathbf{p}_j$, where $s_j = \pm 1$ and $\mathbf{p}_j$ is a fixed vector for each j. For simplicity we assume that the dipoles all have the same magnitude: $|\mathbf{p}_j| = p_0$. This is reasonable if all the TLSs have the same physical origin. The dipoles can have a non-zero equilibrium moment which is random in direction and they interact via the long-range Coulomb interaction. We call this interacting random-field glass model. Somewhat similar models have been introduced in the context of superconducting qubit systems to explain fluctuations in T_1 [140, 141].

The electric field $\langle \mathbf{F}_q \rangle$ on a qubit at the origin of coordinates is

$$\langle \mathbf{F}_q \rangle = \frac{1}{4\pi\varepsilon} \sum_{j=1}^{N} \langle s_j \rangle \frac{3(\mathbf{p}_j \cdot \mathbf{r}_j)\,\mathbf{r}_j - \mathbf{p}_j |\mathbf{r}_j|^2}{|\mathbf{r}_j|^5} \equiv \sum_{j=1}^{N} \langle s_j \rangle \mathbf{F}_j. \tag{4.1}$$

The angle brackets indicate a thermal average and ϵ is electric permittivity around 10 for an oxide or semiconductor layer. In the devices in question, the qubit operation frequency depends linearly on the electric field at its position. The frequency is a quasi-equilibrium quantity, so $\langle \mathbf{F}_q \rangle$ is the object of interest for our purposes. The relation between field and frequency is platform-dependent. In the set-up of Refs. [22, 76, 138], $\langle \mathbf{F}_q \rangle$ causes the displacement of the spin qubit in magnetic field gradients, while in the flip-flop qubit architecture motion of the qubit caused by $\langle \mathbf{F}_q \rangle$ would change the hyperfine coupling or the g-factor [142]. In all cases the displacement changes the qubit operating frequency. The point of interest here is that Δf is linear in some component of the static electric field at the qubit.

The Hamiltonian of the TLSs in our model contains a random-field term H_r and an interaction term H_{int}: $H = H_r + H_{int}$ with

$$H_r = -p_0 \sum_{j=1}^{N} s_j \mathbf{E}_j \cdot \hat{p}_j \tag{4.2}$$

and

$$H_{int} = -\frac{p_0^2}{8\pi\varepsilon} \sum_{j\neq k=1}^{N} s_j s_k V_{jk} \tag{4.3}$$

with

$$V_{jk} = \frac{3\hat{p}_j \cdot (\mathbf{r}_j - \mathbf{r}_k)\,\hat{p}_k \cdot (\mathbf{r}_j - \mathbf{r}_k) - (\hat{p}_j \cdot \hat{p}_k)\,|\mathbf{r}_j - \mathbf{r}_k|^2}{|\mathbf{r}_j - \mathbf{r}_k|^5}. \tag{4.4}$$

The random effective electric fields $\mathbf{E}_j$, if interpreted in a double-well picture of the TLSs, are related to the energy asymmetry ("detuning") of the two wells.

However, the physical origin of the $\mathbf{E}_j$ may not even be the same in all cases. For example, they could be actual external electric fields coming from the gate electrodes, strain fields, asymmetric microscopic defects, *etc.* For our purposes they are considered to be phenomenological parameters that must be fit, since they are very difficult to estimate in the absence of a real microscopic model. We expect N to be a number in the range of perhaps 10 to 100 and to be sample-dependent [40].

4.3.2 Model analysis

The dipoles are the same TLSs that give rise to the noise in the system, but here we are interested in their equilibrium behavior, not their fluctuations. This assumes that measurement of PIRS takes place over a time interval longer than the characteristic switching times of the TLSs. This should be a good approximation, since although those times can be quite long, of order seconds, most of the power spectrum is at higher frequencies.

The temperature dependence of $\langle \mathbf{F}_q \rangle$ in a non-interacting picture, setting $H_{int} = 0$, is already interesting, so we discuss it in detail. In this case the problem is exactly solvable, once the positions of the dipoles are specified. We have $\langle s_j \rangle = \mathrm{sgn}(\hat{p}_j \cdot \mathbf{E}_j) \tanh(p_0 \, \hat{p}_j \cdot \mathbf{E}_j / k_B T)$ where k_B is the Boltzmann constant and T is the temperature. $\langle s_j \rangle$ has a definite sign at $T = 0$ and as T is raised, $\langle s_j \rangle \to 0$ as $T \to \infty$, and we can identify a "turn-off temperature", $T_j = p_0 |\mathbf{E}_j| / k_B$ for each TLS. Substitution into Eq. 4.1 and performing the sum gives the equilibrium electric field at the qubit.

Taking $T = 0$ for a moment we divide the TLSs into two groups. In group S^+ we have the indices j for which $\langle \mathbf{F}_q \rangle \cdot \langle s_j \rangle \, \mathbf{F}_j > 0$ while in group S^- we have the indices $\langle \mathbf{F}_q \rangle \cdot \langle s_j \rangle \, \mathbf{F}_j < 0$. The electric field at the qubit is the result of a random walk of the vectors $\langle s_j \rangle \mathbf{F}_j$ with a resultant vector

$$\langle \mathbf{F}_q \rangle = \sum_{j \in S^+} \langle s_j \rangle \mathbf{F}_j + \sum_{j \in S^-} \langle s_j \rangle \mathbf{F}_j \tag{4.5}$$

The vectors in group S^+ are in the direction of the final result of the walk, while those in group S^- are in the opposite direction. Due to the randomness in the asymmetry, the various components of the walk turn off at different temperatures, and there will be some average turn-off temperature T^+ for group S^+ and a different average turn-off temperature T^- for group S^-.

We now increase T from zero. If $T^+ > T^-$, then the total field strength $|\langle \mathbf{F}_q \rangle|$ will first increase and eventually vanish when $T \gg T^+$. In this case we have a non-monotonic T-dependence of the field strength $|\langle \mathbf{F}_q \rangle|$, a surprising result. T^+ and T^- are not expected to be very different if the dipoles have the same physical structure, but even in this case the relatively small value of N implies that random fluctuations will make $T^+ \neq T^-$. If $T^+ < T^-$, then the total field strength $|\langle \mathbf{F}_q \rangle|$ will decrease as the dominant dipoles turn off and eventually vanish when $T \gg T^-$. If there is a gross mismatch between T^+ and T^-, components of $\langle \mathbf{F}_q \rangle$ could even reverse sign, but overall we would expect a monotonic decrease. The relative magnitudes of $|\sum_{j \in S^+} \langle s_j \rangle \mathbf{F}_j|$ and $|\sum_{j \in S^-} \langle s_j \rangle \mathbf{F}_j|$ are also important. If $|\sum_{j \in S^+} \langle s_j \rangle \mathbf{F}_j|$ dominates, then there is little cancellation in the sum and the non-monotonic behavior will be suppressed. If the fields from S^+ and S^- are comparable, then non-monotonicity is more likely.

Now we turn to the important effects of interactions, as summarized in Eqs. 4.3 and 4.4. Dipolar interactions are always antiferromagnetic. This favors depolarization - a smaller net moment $|\langle \mathbf{P} \rangle| = |\sum_j \langle s_j \rangle \mathbf{p}_j|$. If the TLSs are located to one side of the qubit, then the correlation between $|\langle \mathbf{P} \rangle|$ and $|\langle \mathbf{F}_q \rangle|$ will be strong, but even if the qubit is surrounded symmetrically by the TLSs, fluctuations will still give some correlation in a given sample. Small $|\langle \mathbf{P} \rangle|$ comes from cancellation in the directions of the individual moments.

We introduce additional turn-off temperatures associated with the random fields and the interactions for comparison between the two terms in our model Hamiltonian: $T_r = \langle H_r \rangle / N k_B$ is the average change in the energy from flipping one dipole in the random fields and $T_{int} = \langle H_{int} \rangle / N k_B$ is that in the interaction energy. The root-mean-square values are used for estimating the averages, $\langle H_r \rangle$ and $\langle H_{int} \rangle$.

If $T_{int} < T_r$ then the interactions will turn off first as T is increased, and $|\langle \mathbf{P} \rangle|$ increases. In such case, the interactions have little effect on the temperature dependence. If $T_{int} \gg T_r$ then the system is frozen by the interactions and we expect little change in $|\langle \mathbf{P} \rangle|$ until $T \gg T_{int}$. We can expect the temperature dependence with interaction is much different from that without interaction when $T_{int} > T_r$.

Overall, the effect of interactions is to make cancellation more likely. Unless the interactions are extremely strong, they make the non-monotonic temperature dependence of $|\langle \mathbf{F}_q \rangle|$ and therefore of Δf more likely.

4.4 Numerical Results

4.4.1 Physical models

These analytic considerations are semi-quantitative. To make the arguments more firm, we performed simulations of the model in a hypothetical device that is based on the Si/SiGe heterostructure devices in Refs. [22, 78, 123]. The parameter values and even the positions of the the TLSs are poorly known. This leads us to consider three physical models.

In the first model, called trap model, the TLSs are charge traps near the surface of a two-dimensional electron gas and its image particle of the opposite sign. The trap is positively charged when empty and then relatively negatively charged when full. It can be described as a fluctuating dipole in the z-direction. These dipoles are in a thin layer at positions $\mathbf{r}_j = (x_j, y_j, z_j)$ with $-150\,\text{nm} < x_j < 150\,\text{nm}$, $-150\,\text{nm} < y_j < 150\,\text{nm}$, and $z_j = 50\,\text{nm}$.

The second model conceives of the TLSs as point defect dipoles in the oxide layer with arbitrary orientations, which is called random dipole model. Their positions $\mathbf{r}_j = (x_j, y_j, z_j)$ are in the layer with $-150\,\text{nm} < x_j < 150\,\text{nm}$, $-150\,\text{nm} < y_j < 150\,\text{nm}$, and $30\,\text{nm} < z_j < 50\,\text{nm}$.

The third model is far from real device geometry, but close to the analysis in the previous section. The TLSs are in a spherical shell with their positions $\mathbf{r}_j = (r_j, \theta_j, \phi_j)$ satisfying $60\,\text{nm} < r_j < 80\,\text{nm}$, $0 \leq \theta_j < \pi$, and $0 \leq \phi_j < 2\pi$ in spherical coordinates. We call this spherical shell model.

4.4.2 Temperature dependence of noise electric field

We first show the temperature dependence of noise electric field from the trap and random dipole models because the qubit operation frequency linearly depends on it. The non-interacting case, $H_{int} = 0$, is exactly solvable with the equations given in Sec 4.3. The fully interacting case needs numerical simulation, for which we run Monte Carlo (MC) algorithm with Glauber dynamics.

Glauber dynamics is a way to simulate Ising model, but is slightly modified to use in our simulation:

(1): Choose a TLS randomly,

(2): Compute the change in energy, ΔE, if the TLS were to flip,

(3): Flip the TLS with the probability of $1/(e^{\Delta E/k_B T} + 1)$,

(4): Update TLS configuration with the flipping result.

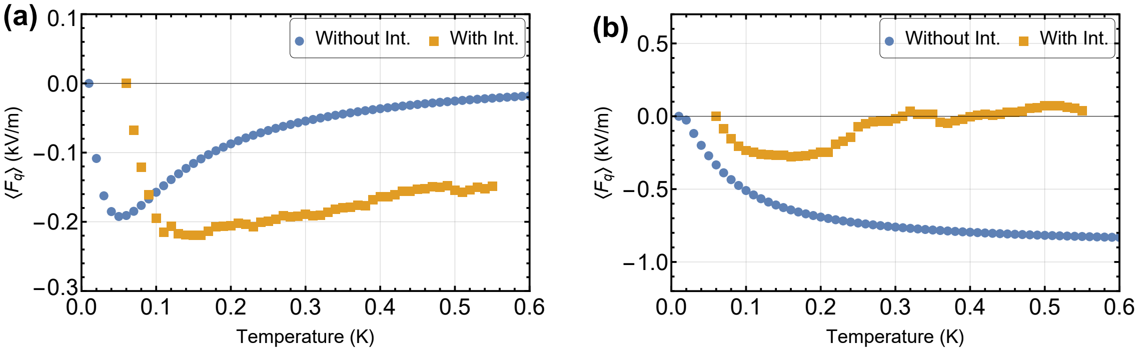

Figure 4.1: Average electric field components at qubit position for trap model. Without Int. and With Int. mean the non-interacting and fully interacting case, respectively. **(a)** Both non-interacting and interacting cases show non-monotonic $\langle \mathbf{F_q} \rangle$. **(b)** Example in which interactions cause non-monotonic behavior. The y components of $\langle \mathbf{F_q} \rangle$ are chosen for the examples.

This procedure is repeated every time step of the MC algorithm and the number of time steps for each temperature is 10^5, from which we take the average value, $\langle \mathbf{F_q} \rangle$. Temperature range is from 0.01 K to 0.6 K with 0.01 K spacing (60 temperature points). Moving average over 11 neighboring temperatures is applied to obtain stable results.

The parameters for numerical simulation in Figs. 4.1 and 4.2 are as follows. The dipole strength $p_0 = 48$ Debye, which is the product of electron charge and 1 nm. The random fields are assumed to follow Gaussian distribution with zero mean and standard deviation of $E_0 = 10^4$ V/m. The directions of the random fields are random on a unit sphere. The number of TLSs is $N = 30$. With these values, $T_r \sim 0.1$ K and $T_{int} \sim 1$ K in most samples. However, T_{int} can vary in a wide range of magnitudes (from 0.1 K to 10 K) because it depends sensitively on the separation and orientation of the distributed TLSs. These values are chosen to be representative of experiments on the Si/SiGe devices, in the sense that most analyses give something like this value for N and we can then fit the value of p_0 so that the decoherence time T_2 from charge noise is about 1μs, again a representative value.

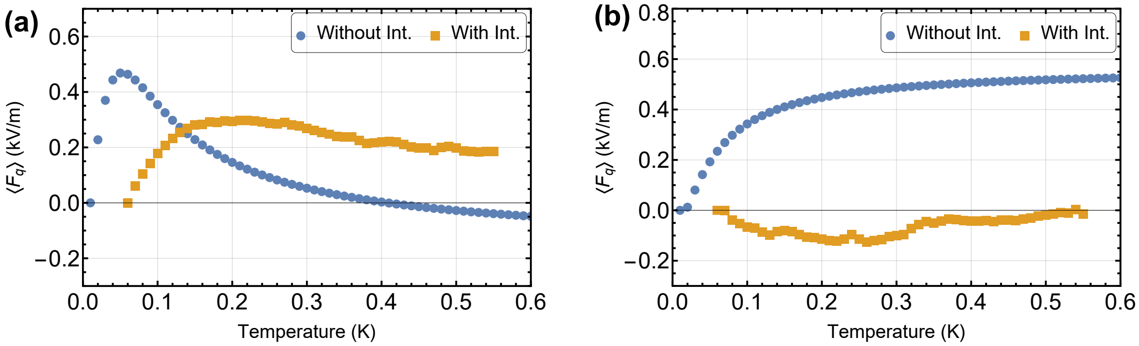

Figure 4.2: Average electric field components at qubit position for random dipole model. Without Int. and With Int. mean the non-interacting and fully interacting case, respectively. **(a)** Both non-interacting and interacting cases show non-monotonic $\langle \mathbf{F_q} \rangle$. **(b)** Example in which interactions cause non-monotonic behavior. The y components of $\langle \mathbf{F_q} \rangle$ are chosen for the examples.

In Fig. 4.1 we plot examples of the y component of $\langle \mathbf{F}_q \rangle(T)$ for the trap model. Non-monotonic temperature dependence appears both in the non-interacting case and fully interacting case in Fig. 4.1(a). Interactions can bring about non-monotonic dependence as in Fig. 4.1(b) where non-interacting case shows monotonic behavior. As noted earlier, the fluctuations due to random fields turn off around $T_r \sim 0.1$ K, which means the non-interacting cases have monotonic increase or decrease at temperatures $T > T_r$. Because $T_{int} > T_r$ in these examples, the interactions play a crucial role in the dependence.

In Fig. 4.2 we plot examples of the y component of $\langle \mathbf{F}_q \rangle(T)$ for the random dipole model. These differ slightly from those of Fig. 4.1, but exhibit similar fashion of temperature dependence. It is important to clarify, however, that the temperature dependence is sample-dependent at these rather low values of N. One should not conclude that the above plots for the trap and random dipole models are entirely typical.

4.4.3 Simulation on a large number of samples

Since $\langle \mathbf{F}_q \rangle(T)$ is highly dependent on samples, it is necessary to figure out if the model analysis works with a large number of samples statistically. We simulate 10,000 random samples both for the trap and random dipole models with high-throughput computing system [143]. The temperature range is from 0.01 K to 1.28 K with log-uniform spacing (100 temperature points). Other parameters are the same as those used in the previous section except for the number of dipoles: $N = 20$ and 30 for $T_{int} \sim 0.1$ K and 1 K, respectively.

To determine whether the samples have non-monotonic temperature dependence, we set up a criterion as follows: from exact or numerical results, we componentwisely define a group of differences in $\langle \mathbf{F}_q \rangle(T)$ as

$$F_{diff} = \{F_{m+1} - F_m |\ m = 1, 2, 3, ..., M - 1\} \tag{4.6}$$

where $M = 100$ is the number of temperature points for evaluation. The average slope magnitude is defined as

$$s = \frac{1}{M-1} \sum_{m=1}^{M-1} |F_{m+1} - F_m|. \tag{4.7}$$

To avoid misleading determination from small fluctuations in the values of $\langle \mathbf{F}_q \rangle(T)$ particularly for MC simulation, small slope elements are excluded from the group F_{diff} so that the group becomes

$$F_{large} = \{F_{m+1} - F_m |\ \frac{s}{2} < |F_{m+1} - F_m|\}. \tag{4.8}$$

Defining signs of the differences as $\sigma_m = \text{sgn}(F_{m+1} - F_m)$, we have groups of positive and negative slopes:

$$\begin{aligned} F_{pos} &= \{F_{m+1} - F_m \mid \sigma_m > 0 \text{ and } F_{m+1} - F_m \in F_{large}\}, \\ F_{neg} &= \{F_{m+1} - F_m \mid \sigma_m < 0 \text{ and } F_{m+1} - F_m \in F_{large}\}. \end{aligned} \tag{4.9}$$

The criterion is then given by

$$\frac{\min(|F_{pos}|, |F_{neg}|)}{|F_{pos}| + |F_{neg}|} > 0.1 \text{ and } s > 5 \tag{4.10}$$

where the first inequality requires that $\langle \mathbf{F}_q \rangle(T)$ has non-negligible positive and negative parts of slopes and the second one demands that the overall frequency shift in the temperature range is not so small. The tolerance values, 0.1 and 5, are empirically chosen and can be adjusted for different systems.

The fractions of the samples having non-monotonic temperature dependence are shown in Table 4.1 for each component of $\langle \mathbf{F}_q \rangle(T)$ with different physical models and T_{int}. In all settings, interaction tends to enhance the non-monotonic behavior. As expected, the increased fractions are larger for $T_r < T_{int}$ than $T_r \sim T_{int}$.

The fractions are almost same for the trap and random dipole models without interaction. With interaction, the random dipole model has higher fractions than the trap model. This might come from $s > 5$ in the criterion because the samples generally show larger electric field magnitudes in the random dipole model than in the trap model. The fractions for z component are smaller than those for x and y components, which may be due to the asymmetric positions of TLSs relative to the qubit ($z_j > 0$).

We also investigate $\langle \mathbf{F}_q \rangle(T)$ for the spherical shell model. It is remarkable to observe that the fractions are much larger than those of the trap and random dipole models, and with interaction most of the samples present non-monotonicity. This

Trap	$\langle F_{q,x} \rangle$	$\langle F_{q,y} \rangle$	$\langle F_{q,z} \rangle$
$T_r < T_{int}$			
Without Int.	15.9%	16.4%	12.0%
With Int.	48.0%	48.6%	40.1%
$T_r \sim T_{int}$			
Without Int.	11.0%	10.9%	7.4%
With Int.	30.5%	30.2%	24.2%

Random dipole	$\langle F_{q,x} \rangle$	$\langle F_{q,y} \rangle$	$\langle F_{q,z} \rangle$
$T_r < T_{int}$			
Without Int.	14.7%	15.9%	12.4%
With Int.	61.9%	61.9%	57.2%
$T_r \sim T_{int}$			
Without Int.	10.0%	9.4%	7.8%
With Int.	42.5%	42.3%	36.9%

Spherical shell	$\langle F_{q,x} \rangle$	$\langle F_{q,y} \rangle$	$\langle F_{q,z} \rangle$
$T_r < T_{int}$			
Without Int.	25.0%	25.3%	28.0%
With Int.	89.5%	89.4%	90.1%
$T_r \sim T_{int}$			
Without Int.	21.0%	21.8%	25.8%
With Int.	79.4%	79.0%	81.4%

Table 4.1: The fractions of the number of samples showing non-monotonic temperature dependence obtained from exact formula or MC simulation for three physical models. $\langle F_{q,i} \rangle$ is the i component of the vector $\langle \mathbf{F}_q \rangle (T)$. Without Int. and With Int. mean the non-interacting and fully interacting case, respectively. $T_r \sim 0.1$ K and $T_{int} \sim 1$K or 0.1K.

suggests that the electric fields from S^+ and S^- are more competitive in this model than the trap and random dipole models where one of the fields frequently dominates. All x, y, and z components should have similar fractions in this model, but the fraction for z component is slightly higher than others for some unknown reason.

4.4.4 Fitting for experimental data

To explicitly show the temperature dependence of the qubit frequency shift, $\Delta f(T)$, we focus on the device of Undseth *et al.* [123]. Our purpose is to reproduce the figure for Larmor frequency shifts of six qubits. The non-interacting random dipole model is chosen for simulation, and the only difference from the settings in the previous sections is the range in the z-direction, $31\text{nm} < z_j < 36\text{nm}$. For other parameters that are not provided in the paper such as magnetic field gradients, we take them from another device [78]. The magnetic field gradients at the origin in units of $\text{mT}(\text{nm})^{-1}$ are $\partial B_x/\partial x = -0.20$, $\partial B_y/\partial x = -0.05$, $\partial B_z/\partial x = -0.27$, $\partial B_x/\partial y = -0.03$, $\partial B_y/\partial y = 0.18$, and $\partial B_z/\partial y = -0.02$. The variation in the z-direction is not needed because the qubits are assumed to be in a circularly symmetric two-dimensional harmonic potential, $k(x^2 + y^2)/2$. The transverse effective mass $m = 0.19\, m_e = 1.73 \times 10^{-31}$ kg. The lowest orbital excitation frequency is $\omega_{orb} = 6.84 \times 10^{11}\,\text{s}^{-1}$, which is related to the spring constant, $k = m\omega_{orb}^2$. These numerical values are typical of micromagnet-based device.

With the parameters, we can simulate the qubit frequency shifts by the following equation:

$$\Delta f_i = \alpha \frac{g\mu_B}{h} \frac{q}{m\omega_{orb}^2} \left[\frac{\partial B_i}{\partial x} \Delta F_{q,x} + \frac{\partial B_i}{\partial y} \Delta F_{q,y} \right] \tag{4.11}$$

where $g = 2.0$ is the electron g-factor, μ_B is the Bohr magneton, h is the Planck constant, and the index i can be x or y depending on the applied magnetic field direction. Since the factor $q/m\omega_{orb}^2$ and the magnetic field gradients are not known for the device in question, α is introduced as a fitting parameter.

The fitting result is shown in Fig. 4.3 for the sample that has temperature dependence similar to that in Ref. [123]. Six different $\alpha = 0.6$, 0.59, 0.4, 0.39, 0.5, and 0.3 are used for the curves for the six qubits, Q1-Q6, respectively. The applied magnetic field is assumed to be in the y-direction, $N = 30$, and $E_0 = 1.2 \times 10^5$ V/m. The curves agree well with the experimental data in general; for Q5 and Q6, they slightly depart from the data. These deviations may be attributed to the spatial dependence of unknown parameters used in Eq. 4.11.

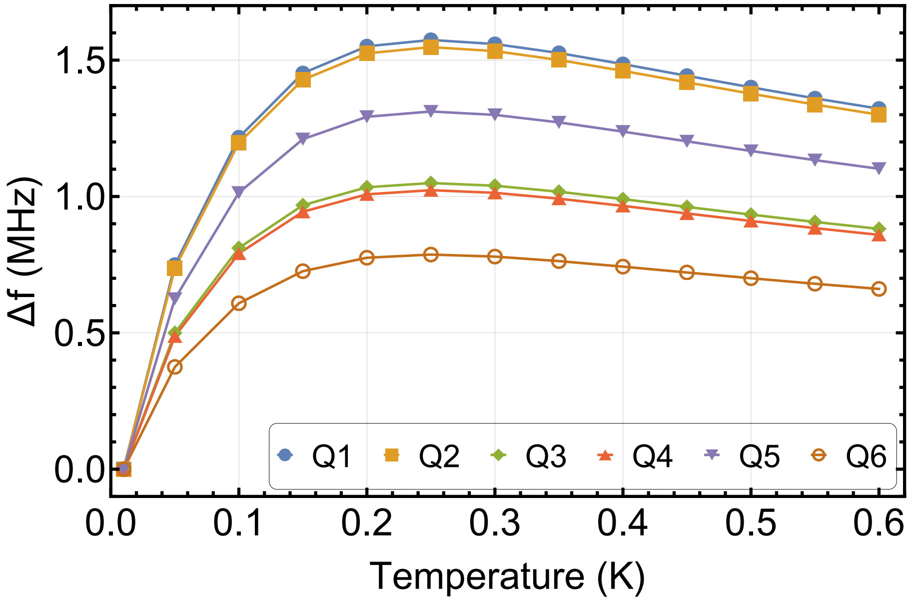

Figure 4.3: The fitting for the experimental data of Larmor frequency shifts of six qubits in Ref. [123]. Q1-Q6 denote the six qubits. Fitting parameter α is varied instead of simulating for different positions of the qubits. The applied magnetic field is assumed to be in the y-direction.

4.5 Discussion

To summarize, we identify that the electric fields from TLSs can produce non-monotonic temperature dependence of the qubit frequency shift from the theoretical model and numerical results. The non-monotonic dependence of the electric fields is confirmed in some samples for the trap and random dipole models. The simulation results on a large number of samples support the model analysis and show that the interactions between TLSs can be a major factor. We also reproduce the experimental data for the six-qubit device in Ref. [123] by simulating non-interacting random dipole model with a fitting parameter.

An unraveled conundrum is that the noisy environment of the six qubits seem to be global according to the fitting result which is reproduced only by a multiplicative factor. It is peculiar for such global effect to have no impact on other on-chip charge sensors as noted in Ref. [123]. Furthermore, the six qubits are separated by 90 nm, with maximum spacing being 450 nm between Q1 and Q6 [22]. The global effect seems to contradict to the observation that the noisy environment is fairly local with large inter-dot spacings [137].

Chapter 5

Conclusion

We have extensively investigated various methods for characterizing noise sources in semiconductor quantum dot devices. The principal objectives were to identify the dominant noise source affecting spin qubits, improve the coherence of the qubits, and understand the mechanism for the operating frequency shifts of the qubits. In particular, we scrutinized the charge noise due to its significant impact on qubit decoherence.

One future direction of study is to find out the physical origin of charge noise, generally attributed to two-level systems (TLS). This research should involve collaboration with materials science, as there are numerous potential defects in oxides that could generate the charge noise [144]. New experimental methods need to be proposed to study the properties of the TLSs, as the current focus on qubit-centric coherence times and the power spectral density (PSD) of individual qubits has been considerably explored. Further characterization of the TLSs may require direct inspection, as demonstrated in Ref. [145].

Another notable approach for future research includes analyzing the spatial correlation between two qubits, which can provide an additional tool for characterization [136, 137]. The cross-PSD obtained from two qubits is believed to be closely related to the distribution of TLSs surrounding the qubits. Especially, the TLSs are expected to divide into two groups based on their orientations and relative positions to the qubits: one group with positive correlation and the other with negative correlation. We have made some progress in this area and have developed explanations for experimental data on cross-PSDs.

From a more practical viewpoint, studying the optimal inter-dot spacing between qubits in relation to their cross-PSDs is worthwhile. Since surface codes can correct only for the errors that occur locally, it is critical for the qubits to have uncorrelated errors [34]. Generally, correlated error rates decrease with increased inter-dot spacing, making larger spacing between qubits preferable. However, compact qubit structures are necessary for scalable quantum computing. Thus, there is a trade-off between the two factors, and an optimal spacing should exist.

Another future direction is more general in nature. Decoherence typically arises from our lack of understanding of the environment of qubits. In order to control the qubits and measure computational results, we must transmit information to and from the qubits. During this transfer, unwanted interactions with the environment should be minimized to reduce decoherence. Achieving a perfect balance between communicating with the qubits and isolating them from environment poses a well-known dilemma in quantum computing. It could be challenging to construct a fault-tolerant quantum computing system by assembling Lego-like blocks of qubits and elementary gates to form a larger system with millions of qubits. This is due to the fact that macroscopic systems typically do not exhibit quantum behavior. Hence, it is essential to study either the larger system that encompasses the qubits and their environment as a whole or to explore buffer layers that enable more coherent information transfer.

A lot of work is still needed not only for characterizing noise sources in semiconductor qubit devices, but also for developing universal and fault-tolerant quantum computing systems using semiconductor qubits. Despite the challenges, we remain optimistic about the potential of the field of quantum computing and believe it is worth investing our efforts.

Appendix A

Driving classical damped harmonic oscillator

A.1 Damped harmonic oscillator coupled to thermal bath

Following the notation of the study on damped harmonic oscillator with driving force and fluctuating thermal bath [146], the Langevin equation for a particle is given by

$$m\ddot{x} + \gamma\dot{x} + kx = F_0\cos(\omega_d t) + \sqrt{2\gamma k_B T}\xi(t) \tag{A.1}$$

where m is the mass of the particle, γ is the damping constant, k is the spring constant, F_0 is the amplitude of the driving force, ω_d is the driving frequency, and $\xi(t)$ is the noise term from δ-correlated Gaussian white noise of thermal bath that has zero mean and unit intensity: $\langle\xi(t)\xi(t')\rangle = \delta(t-t')$. Our interest is the correlation function $\langle x(t)x(t')\rangle_{st}$ where $\langle\cdot\rangle_{st}$ is the ensemble average with long-time limit ($\gamma_0 t \gg 1$) and $\gamma_0 = \gamma/2m$ is the damping coefficient.

First of all, consider the case where there is no driving force, *i.e.* $F_0 = 0$. The position $x(t)$ can be written as a sum of homogeneous solution $x_c(t)$ and particular solution $x_\xi(t)$:

$$x(t) = x_c(t) + x_\xi(t) = Ae^{-\gamma_0 t}\sin(\Omega t) + Be^{-\gamma_0 t}\cos(\Omega t) + \sqrt{2\gamma k_B T}\int_0^\infty G(t,u)\xi(u)du \tag{A.2}$$

where $\Omega^2 = \omega_0^2 - \gamma_0^2$, $\omega_0^2 = k/m$, and the Green function for strongly damped regime ($\gamma_0 > \omega_0$) reads

$$G(t,u) = \Theta(t-u)\frac{1}{m\Omega_0}e^{-\gamma_0(t-u)}\sinh[\Omega_0(t-u)] \tag{A.3}$$

with $\Omega_0^2 = \gamma_0^2 - \omega_0^2 = -\Omega^2$ and Heaviside step function $\Theta(t) = 1$ for $t > 0$ and $\Theta(t) = 0$ for $t < 0$. Since $\langle x_c(t)\rangle_{st} \to 0$ due to exponential decaying terms,

$$\langle x(t)x(t')\rangle_{st} = \langle x_\xi(t)x_\xi(t')\rangle_{st} = 2\gamma k_B T\int_0^\infty\int_0^\infty dudu' G(t,u)G(t',u')\langle\xi(u)\xi(u')\rangle_{st}. \tag{A.4}$$

After expanding the Green functions,

$$\begin{aligned}\langle x_\xi(t)x_\xi(t')\rangle_{st} =& \frac{2\gamma k_B T}{m^2\Omega_0^2}e^{-\gamma_0(t+t')} \\ &\times\int_0^t\int_0^{t'} dudu'\, e^{\gamma_0(u+u')}\sinh[\Omega_0(t-u)]\sinh[\Omega_0(t'-u')]\delta(u-u').\end{aligned} \tag{A.5}$$

By introducing indicator functions such that $\chi_{\{0,t\}}(u) = 1$ when $u \in (0,t)$ and otherwise $\chi_{\{0,t\}}(u) = 0$,

$$\begin{aligned}\langle x_\xi(t)x_\xi(t')\rangle_{st} =& \frac{2\gamma k_B T}{m^2\Omega_0^2} e^{-\gamma_0(t+t')} \int_{\mathbb{R}}\int_{\mathbb{R}} du du' \, \chi_{\{0,t\}}(u)\chi_{\{0,t'\}}(u') \\ & \times e^{\gamma_0(u+u')} \sinh[\Omega_0(t-u)] \sinh[\Omega_0(t'-u')]\delta(u-u') \\ =& \frac{2\gamma k_B T}{m^2\Omega_0^2} e^{-\gamma_0(t+t')} \int_{\mathbb{R}} du \, \chi_{\{0,t\}}(u)\chi_{\{0,t'\}}(u) \\ =& \times e^{2\gamma_0 u} \sinh[\Omega_0(t-u)] \sinh[\Omega_0(t'-u)] \\ =& \frac{2\gamma k_B T}{m^2\Omega_0^2} e^{-\gamma_0(t+t')} \int_0^{t_s} du \, e^{2\gamma_0 u} \sinh[\Omega_0(t-u)] \sinh[\Omega_0(t'-u)],\end{aligned} \tag{A.6}$$

where $t_s = t \wedge t'$ is the smaller one between t and t'. This equation results in

$$\begin{aligned}\langle x_\xi(t)x_\xi(t')\rangle_{st} =& \frac{\gamma_0 k_B T}{2m\Omega_0^2} e^{-\gamma_0(t+t')} \\ & \times \left[\frac{e^{\Omega_0(t+t')}}{\gamma_0 - \Omega_0} e^{2(\gamma_0-\Omega_0)t_s} + \frac{e^{-\Omega_0(t+t')}}{\gamma_0 + \Omega_0} e^{2(\gamma_0+\Omega_0)t_s} \right. \\ & \left. - \frac{e^{\Omega_0(t-t')}}{\gamma_0} e^{2\gamma_0 t_s} - \frac{e^{-\Omega_0(t-t')}}{\gamma_0} e^{2\gamma_0 t_s} \right],\end{aligned} \tag{A.7}$$

which reduces to $k_B T/m\omega_0^2$ when $t = t' = t_s$. To calculate Fourier transform of the correlation function, let $t > t'$. Then the correlation function is

$$\langle x_\xi(t)x_\xi(t')\rangle_{st} = \frac{k_B T}{\Omega_0 m\omega_0^2} e^{-\gamma_0(t-t')}[\gamma_0 \sinh(\Omega_0(t-t')) + \Omega_0 \cosh(\Omega_0(t-t'))]. \tag{A.8}$$

The right-sided Fourier transform is

$$\langle x_\xi x_\xi\rangle_{right} = \int_0^\infty d\tau \, e^{i\omega\tau} \langle x_\xi(\tau)x_\xi(0)\rangle_{st} = \frac{k_B T}{2\Omega_0 m\omega_0^2}\left[\frac{\omega_p}{\omega_m - i\omega} - \frac{\omega_m}{\omega_p - i\omega}\right] \tag{A.9}$$

where $\omega_p = \gamma_0 + \Omega_0$ and $\omega_m = \gamma_0 - \Omega_0$. For $t < t'$, the left-sided Fourier transform is

$$\langle x_\xi x_\xi\rangle_{left} = \int_{-\infty}^0 d\tau \, e^{i\omega\tau} \langle x_\xi(\tau)x_\xi(0)\rangle_{st} = \frac{k_B T}{2\Omega_0 m\omega_0^2}\left[\frac{\omega_p}{\omega_m + i\omega} - \frac{\omega_m}{\omega_p + i\omega}\right]. \tag{A.10}$$

The total (two-sided) Fourier transform is their sum:

$$\begin{aligned}\langle x_\xi x_\xi\rangle_\omega =&\langle x_\xi x_\xi\rangle_{left} + \langle x_\xi x_\xi\rangle_{right}\\ =&\frac{\pi k_B T}{\Omega_0 m\omega_0^2}\left[\omega_p\left\{\frac{\omega_m}{\pi(\omega^2+\omega_m^2)}\right\} - \omega_m\left\{\frac{\omega_p}{\pi(\omega^2+\omega_p^2)}\right\}\right].\end{aligned} \tag{A.11}$$

It is noteworthy that the total Fourier transform is the difference between two Lorentzians whose widths are ω_m and ω_p respectively. Since $\omega_p > \omega_m$, its shape looks like sharpened single Lorentzian. In extremely damped regime where $\gamma_0 \gg \omega_0$ (or equivalently $\omega_p \gg \omega_m$), it follows $1/\omega^2$. This might explain recent experimental results that measure $1/\omega^2$ power spectrum in ultralow frequency range (below 10^{-3} Hz) only with single extremely damped harmonic oscillator [54]. Dutta-Horn model can also explain the $1/\omega^2$ behavior if the activation energy is very high compared to thermal energy, which is equivalent to the extreme damping condition.

Assume that the oxide layer is electrically neutral and there is fluctuation of electric potential. It would shift a charge from its original position, forming a noise dipole $\mathbf{p} = x\hat{d}$ whose magnitude acts as damped harmonic oscillator coupled to thermal bath. If the size of the noise dipole is small compared to the distance from a qubit, it can be approximated to a point dipole whose electric field is

$$\mathbf{E}(\mathbf{r}, t) = \frac{3(\mathbf{p}\cdot\mathbf{R})\mathbf{R} - R^2\mathbf{p}}{R^5} \tag{A.12}$$

where $\mathbf{R} = \mathbf{r} - \mathbf{r}'$ is the displacement vector from the dipole to the qubit and the factor of $1/4\pi\epsilon_0$ is suppressed for brevity. The Fourier transform of the correlation function for electric field at qubit position is

$$\langle E_i E_j\rangle_\omega = \frac{9(\mathbf{p}\cdot\mathbf{R})^2 R_i R_j - 3(\mathbf{p}\cdot\mathbf{R})R^2 R_i d_j - 3(\mathbf{p}\cdot\mathbf{R})R^2 d_i R_j + R^4 d_i d_j}{R^{10}}\langle x_\xi x_\xi\rangle_\omega \tag{A.13}$$

where subscripts i, j are Cartesian index. This electric field noise will directly affect the decoherence of charge qubit while it will be converted to magnetic field noise that contributes to the decoherence of spin qubit through magnetic field gradients from micromagnets.

Since a small number of Lorentzians can constitute $1/f$ noise (roughly one Lorentzian per one decade of frequency range), this classical model seems to be enough to explain the noise. Lorentzian shape deviated from power-law spectrum might be attributed to the stronger effect of noise dipole that is closer to the qubit than other noise dipoles. The nonlinear dependence of noise power on temperature may be addressed by introducing nonuniform temperature distribution (or temperature fluctuation) in the layer [94], but still needs further study [147, 148].

The correlation function for weakly damped regime ($\gamma_0 < \omega_0$) is

$$\langle x_\xi(t)x_\xi(t')\rangle_{st} = \frac{2\gamma k_B T}{m^2\Omega^2} e^{-\gamma_0(t+t')} \int_0^{t_s} du\, e^{2\gamma_0 u} \sin[\Omega(t-u)] \sin[\Omega(t'-u)] \tag{A.14}$$

where the Ω_0 in Eq. A.6 is simply replaced by $i\Omega$. Letting $t > t'$ leads to

$$\langle x_\xi(t)x_\xi(t')\rangle_{st} = \frac{k_B T}{\Omega m\omega_0^2} e^{-\gamma_0(t-t')} [\gamma_0 \sin(\Omega(t-t')) + \Omega\cos(\Omega(t-t'))]. \tag{A.15}$$

The total Fourier transform is

$$\begin{aligned} \langle x_\xi x_\xi\rangle_\omega = \frac{\pi k_B T}{\Omega m\omega_0^2} \Bigg[&(\omega + 2\Omega) \left\{ \frac{\gamma_0}{\pi((\omega+\Omega)^2 + \gamma_0^2)} \right\} \\ &-(\omega - 2\Omega) \left\{ \frac{\gamma_0}{\pi((\omega-\Omega)^2 + \gamma_0^2)} \right\} \Bigg]. \end{aligned} \tag{A.16}$$

This has more complicated shape than that of strongly damped regime. It consists of products of linear term and normalized Lorentzian whose center is shifted. With very small damping ($\gamma_0 \ll \omega_0$), it shows sharp peaks near $\omega = \pm\omega_0$ while it looks like broadened Lorentzian centered at $\omega = 0$ when $\gamma_0 \sim \omega_0$. The peak shape might explain bumps appearing in experimental power spectrum since Lorentzians centered at zero frequency only have negative slopes. For the same reason, Dutta-Horn model is inappropriate for reproducing the bumps because the individual power spectrum of two-level systems in the model is Lorentzian centered at $\omega = 0$.

Let us suppose that an experimental power spectrum comprises Lorentzians centered at zero frequency from strongly damped oscillators and shifted Lorentzians from weakly damped oscillators. This can be a mathematical justification, but does not give any insight for the physical origin of $1/f$ noise. To validate the damped harmonic oscillator model, we have to think about the source of each term in Langevin equation: damping term that dissipates kinetic energy of a charge to thermal bath and potential term related to natural frequency. The latter can be derived from any type of potential well that is approximated to harmonic potential near its minimum. The former might come from the interaction with nearby charges. One of the candidates would be electron clouds of atoms displaced from their equilibrium and closely packed with other atoms, which is natural in solid state systems. Since superconductor is usually used for metallic gates in which no resistive force on electrons exist, the atoms in semiconductor or insulator should be under consideration.

A.2 Driving damped harmonic oscillator

Now let us add driving force term x_d to the correlation function such that

$$\begin{aligned}\langle x(t)x(t')\rangle_{st} &= \langle (x_d(t) + x_\xi(t))(x_d(t') + x_\xi(t'))\rangle_{st} \\ &= \int_0^\infty \int_0^\infty du du' G(t,u)G(t',u')[F(u)F(u') + 2\gamma k_B T \langle \xi(u)\xi(u')\rangle_{st}].\end{aligned} \tag{A.17}$$

As there are no cross terms (due to $\langle \xi(t) \rangle = 0$), the correlation function for driving force can be obtained separately:

$$\langle x_d(t)x_d(t')\rangle_{st} = \lim_{\gamma_0 t, \gamma_0 t' \gg 1} \int_0^\infty G(t,u)F(u)du \int_0^\infty G(t',u')F(u')du'. \tag{A.18}$$

To proceed for strongly damped regime, we need the long-time limit average of $x_d(t)$:

$$\begin{aligned}
\langle x_d(t)\rangle_{st} &= \lim_{\gamma_0 t \gg 1} \int_0^\infty G(t,u)F(u)du \\
&= \lim_{\gamma_0 t \gg 1} \frac{F_0}{m\Omega_0} \int_0^t e^{-\gamma_0(t-u)} \sinh[\Omega_0(t-u)] \cos(\omega_d u) du \\
&= \lim_{\gamma_0 t \gg 1} \frac{F_0}{2m\Omega_0} e^{-\gamma_0 t} \\
&\quad \times \left[e^{\Omega_0 t} \left(\frac{e^{\omega_m t}}{\omega_m^2 + \omega_d^2} (\omega_m \cos(\omega_d t) + \omega_d \sin(\omega_d t)) - \frac{\omega_m}{\omega_m^2 + \omega_d^2} \right) \right. \\
&\quad \left. - e^{-\Omega_0 t} \left(\frac{e^{\omega_p t}}{\omega_p^2 + \omega_d^2} (\omega_p \cos(\omega_d t) + \omega_d \sin(\omega_d t)) - \frac{\omega_p}{\omega_p^2 + \omega_d^2} \right) \right] \\
&= \frac{F_0}{2m\Omega_0} \left[\frac{1}{\omega_m^2 + \omega_d^2} (\omega_m \cos(\omega_d t) + \omega_d \sin(\omega_d t)) \right. \\
&\quad \left. - \frac{1}{\omega_p^2 + \omega_d^2} (\omega_p \cos(\omega_d t) + \omega_d \sin(\omega_d t)) \right] \\
&= \frac{F_0}{2m\Omega_0} \left[\frac{1}{A_m} \cos(\omega_d t - \alpha_m) - \frac{1}{A_p} \cos(\omega_d t - \alpha_p) \right]
\end{aligned} \tag{A.19}$$

where $A_{m(p)} = \sqrt{\omega_{m(p)}^2 + \omega_d^2}$ and $\alpha_{m(p)} = \tan^{-1}(\omega_d/\omega_{m(p)})$. The correlation function is then

$$\begin{aligned}
\langle x_d(t)x_d(t')\rangle_{st} = \frac{F_0^2}{4m\Omega_0^2} &\left[\frac{1}{A_m} \cos(\omega_d t - \alpha_m) - \frac{1}{A_p} \cos(\omega_d t - \alpha_p) \right] \\
\times &\left[\frac{1}{A_m} \cos(\omega_d t' - \alpha_m) - \frac{1}{A_p} \cos(\omega_d t' - \alpha_p) \right].
\end{aligned} \tag{A.20}$$

Likewise, the long-time limit average of $x_d(t)$ for weakly damped regime is

$$\begin{aligned}\langle x_d(t)\rangle_{st} &= \lim_{\gamma_0 t\gg 1}\int_0^{\infty} G(t,u)F(u)du \\ &= \lim_{\gamma_0 t\gg 1}\frac{F_0}{m\Omega}\int_0^{t} e^{-\gamma_0(t-u)}\sin[\Omega(t-u)]\cos(\omega_d u)du \\ &= \frac{F_0}{mA}\left[(\omega_0^2-\omega_d^2)\cos(\omega_d t)+2\gamma_0\omega_d\sin(\omega_d t)\right]\end{aligned} \tag{A.21}$$

where $A = (\omega_0^2-\omega_d^2)^2+4\gamma_0^2\omega_d^2$. The correlation function is

$$\begin{aligned}\langle x_d(t)x_d(t')\rangle_{st} = \frac{F_0^2}{mA^2}&\left[(\omega_0^2-\omega_d^2)\cos(\omega_d t)+2\gamma_0\omega_d\sin(\omega_d t)\right] \\ \times&\left[(\omega_0^2-\omega_d^2)\cos(\omega_d t')+2\gamma_0\omega_d\sin(\omega_d t')\right].\end{aligned} \tag{A.22}$$

In both regimes, the terms that depend on $\omega_d(t-t')$ would result in sharp peaks at $\omega = \pm\omega_d$ in the noise power spectrum. The terms that depend on $\omega_d(t+t')$ are hard to be interpreted via Wiener-Khinchin theorem, but can be seen as transients that do not contribute to the noise power spectrum.

The introduction of driving force seems to be harmful since it adds up peaks at driving frequency to the noise power spectrum while leaving the original one as it was. This can be ascribed to the infinite number of energy levels (or displacements) that *classical* harmonic oscillator can take. In other words, there is corresponding energy level given any driving force and thermal bath configuration at certain time, which means the energy supplied from driving force directly leads to more fluctuating behavior of the particle.

The classical damped harmonic oscillator model naturally raises a question that what happens if the energy levels are quantized, *e.g.* two-level system or quantum harmonic oscillator. For a quantum model, driving force on noise sources does not always have a negative impact on the qubit.

Bibliography

[1] R. P. Feynman, “Simulating physics with computers”, International Journal of Theoretical Physics **21**, 467–488 (1981).

[2] P. W. Shor, “Algorithms for quantum computation: discrete logarithms and factoring”, in Proceedings of the 35th annual symposium on foundations of computer science (IEEE, 1994), pp. 124–134.

[3] R. L. Rivest, A. Shamir, and L. Adleman, “A method for obtaining digital signatures and public-key cryptosystems”, Communications of the ACM **21**, 120–126 (1978).

[4] L. K. Grover, “A fast quantum mechanical algorithm for database search”, in Proceedings of the 28th annual ACM symposium on theory of computing (1996), pp. 212–219.

[5] M. A. Nielsen and I. L. Chuang, *Quantum computation and quantum information: 10th anniversary edition* (Cambridge University Press, 2010).

[6] H.-L. Huang, D. Wu, D. Fan, and X. Zhu, “Superconducting quantum computing: a review”, Science China Information Sciences **63**, 1–32 (2020).

[7] C. D. Bruzewicz, J. Chiaverini, R. McConnell, and J. M. Sage, “Trapped-ion quantum computing: progress and challenges”, Applied Physics Reviews **6**, 021314 (2019).

[8] L. Henriet, L. Beguin, A. Signoles, T. Lahaye, A. Browaeys, G.-O. Reymond, and C. Jurczak, “Quantum computing with neutral atoms”, Quantum **4**, 327 (2020).

[9] A. Chatterjee, P. Stevenson, S. De Franceschi, A. Morello, N. P. de Leon, and F. Kuemmeth, “Semiconductor qubits in practice”, Nature Reviews Physics **3**, 157–177 (2021).

[10] S. Pezzagna and J. Meijer, “Quantum computer based on color centers in diamond”, Applied Physics Reviews **8**, 011308 (2021).

[11] P. Kok, W. J. Munro, K. Nemoto, T. C. Ralph, J. P. Dowling, and G. J. Milburn, “Linear optical quantum computing with photonic qubits”, Reviews of Modern Physics **79**, 135 (2007).

[12] V. Lahtinen and J. Pachos, “A short introduction to topological quantum computation”, SciPost Physics **3**, 021 (2017).

[13] D. P. DiVincenzo, “The physical implementation of quantum computation”, Fortschritte der Physik: Progress of Physics **48**, 771–783 (2000).

[14] D. Loss and D. P. DiVincenzo, “Quantum computation with quantum dots”, Physical Review A **57**, 120 (1998).

[15] T. Hayashi, T. Fujisawa, H.-D. Cheong, Y. H. Jeong, and Y. Hirayama, “Coherent manipulation of electronic states in a double quantum dot”, Physical Review Letters **91**, 226804 (2003).

[16] J. R. Petta, A. C. Johnson, J. M. Taylor, E. A. Laird, A. Yacoby, M. D. Lukin, C. M. Marcus, M. P. Hanson, and A. C. Gossard, “Coherent manipulation of coupled electron spins in semiconductor quantum dots”, Science **309**, 2180–2184 (2005).

[17] J. Medford, J. Beil, J. Taylor, S. Bartlett, A. Doherty, E. Rashba, D. DiVincenzo, H. Lu, A. Gossard, and C. M. Marcus, “Self-consistent measurement and state tomography of an exchange-only spin qubit”, Nature Nanotechnology **8**, 654–659 (2013).

[18] D. Kim, Z. Shi, C. Simmons, D. Ward, J. Prance, T. S. Koh, J. K. Gamble, D. Savage, M. Lagally, M. Friesen, et al., “Quantum control and process tomography of a semiconductor quantum dot hybrid qubit”, Nature **511**, 70–74 (2014).

[19] H. Watzinger, J. Kukučka, L. Vukušić, F. Gao, T. Wang, F. Schäffler, J.-J. Zhang, and G. Katsaros, “A germanium hole spin qubit”, Nature Communications **9**, 3902 (2018).

[20] R. Savytskyy, T. Botzem, I. Fernandez de Fuentes, B. Joecker, J. J. Pla, F. E. Hudson, K. M. Itoh, A. M. Jakob, B. C. Johnson, D. N. Jamieson, et al., “An electrically driven single-atom “flip-flop” qubit”, Science Advances **9**, eadd9408 (2023).

[21] R. Van Meter and D. Horsman, “A blueprint for building a quantum computer”, Communications of the ACM **56**, 84–93 (2013).

[22] S. G. Philips, M. T. Mądzik, S. V. Amitonov, S. L. de Snoo, M. Russ, N. Kalhor, C. Volk, W. I. Lawrie, D. Brousse, L. Tryputen, et al., “Universal control of a six-qubit quantum processor in silicon”, Nature **609**, 919–924 (2022).

[23] A. J. Weinstein, M. D. Reed, A. M. Jones, R. W. Andrews, D. Barnes, J. Z. Blumoff, L. E. Euliss, K. Eng, B. H. Fong, S. D. Ha, et al., “Universal logic with encoded spin qubits in silicon”, Nature **615**, 817–822 (2023).

[24] X. Xue, B. Patra, J. P. van Dijk, N. Samkharadze, S. Subramanian, A. Corna, B. Paquelet Wuetz, C. Jeon, F. Sheikh, E. Juarez-Hernandez, et al., “CMOS-based cryogenic control of silicon quantum circuits”, Nature **593**, 205–210 (2021).

[25] A. Zwerver, T. Krähenmann, T. Watson, L. Lampert, H. C. George, R. Pillarisetty, S. Bojarski, P. Amin, S. Amitonov, J. Boter, et al., “Qubits made by advanced semiconductor manufacturing”, Nature Electronics **5**, 184–190 (2022).

[26] L. Petit, H. Eenink, M. Russ, W. Lawrie, N. Hendrickx, S. Philips, J. Clarke, L. Vandersypen, and M. Veldhorst, “Universal quantum logic in hot silicon qubits”, Nature **580**, 355–359 (2020).

[27] C. H. Yang, R. Leon, J. Hwang, A. Saraiva, T. Tanttu, W. Huang, J. C. Lemyre, K. W. Chan, K. Tan, F. E. Hudson, et al., “Operation of a silicon quantum processor unit cell above one kelvin”, Nature **580**, 350–354 (2020).

[28] J. Yoneda, K. Takeda, T. Otsuka, T. Nakajima, M. R. Delbecq, G. Allison, T. Honda, T. Kodera, S. Oda, Y. Hoshi, et al., “A quantum-dot spin qubit with coherence limited by charge noise and fidelity higher than 99.9%”, Nature Nanotechnology **13**, 102–106 (2018).

[29] C. Yang, K. Chan, R. Harper, W. Huang, T. Evans, J. Hwang, B. Hensen, A. Laucht, T. Tanttu, F. Hudson, et al., “Silicon qubit fidelities approaching incoherent noise limits via pulse engineering”, Nature Electronics **2**, 151 (2019).

[30] A. R. Mills, C. R. Guinn, M. J. Gullans, A. J. Sigillito, M. M. Feldman, E. Nielsen, and J. R. Petta, “Two-qubit silicon quantum processor with operation fidelity exceeding 99%”, Science Advances **8**, eabn5130 (2022).

[31] M. T. Mądzik, S. Asaad, A. Youssry, B. Joecker, K. M. Rudinger, E. Nielsen, K. C. Young, T. J. Proctor, A. D. Baczewski, A. Laucht, et al., “Precision tomography of a three-qubit donor quantum processor in silicon”, Nature **601**, 348–353 (2022).

[32] X. Xue, M. Russ, N. Samkharadze, B. Undseth, A. Sammak, G. Scappucci, and L. M. Vandersypen, “Quantum logic with spin qubits crossing the surface code threshold”, Nature **601**, 343–347 (2022).

[33] A. Noiri, K. Takeda, T. Nakajima, T. Kobayashi, A. Sammak, G. Scappucci, and S. Tarucha, “Fast universal quantum gate above the fault-tolerance threshold in silicon”, Nature **601**, 338–342 (2022).

[34] A. N. Cleland, “An introduction to the surface code”, SciPost Phys. Lect. Notes, 49 (2022).

[35] W. A. Coish and J. Baugh, “Nuclear spins in nanostructures”, Phys. Status Solidi (b) **246**, 2203–2215 (2009).

[36] F. Beaudoin and W. A. Coish, "Enhanced hyperfine-induced spin dephasing in a magnetic-field gradient", Phys. Rev. B **88**, 085320 (2013).

[37] M. Veldhorst, J. C. C. Hwang, C. H. Yang, A. W. Leenstra, B. de Ronde, J. P. Dehollain, J. T. Muhonen, F. E. Hudson, K. M. Itoh, A. Morello, and A. S. Dzurak, "An addressable quantum dot qubit with fault-tolerant control-fidelity", Nat. Nanotechnol. **9**, 981–985 (2014).

[38] K. Eng, T. D. Ladd, A. Smith, M. G. Borselli, A. A. Kiselev, B. H. Fong, K. S. Holabird, T. M. Hazard, B. Huang, P. W. Deelman, I. Milosavljevic, A. E. Schmitz, R. S. Ross, M. F. Gyure, and A. T. Hunter, "Isotopically enhanced triple-quantum-dot qubit", Sci. Adv. **1**, e1500214 (2015).

[39] J. Yoneda, K. Takeda, T. Otsuka, T. Nakajima, M. R. Delbecq, G. Allison, T. Honda, T. Kodera, S. Oda, Y. Hoshi, N. Usami, K. M. Itoh, and S. Tarucha, "A quantum-dot spin qubit with coherence limited by charge noise and fidelity higher than 99.9%", Nat. Nanotechnol. **13**, 102–106 (2018).

[40] E. J. Connors, J. Nelson, H. Qiao, L. F. Edge, and J. M. Nichol, "Low-frequency charge noise in Si/SiGe quantum dots", Phys. Rev. B **100**, 165305 (2019).

[41] A. V. Khaetskii and Y. V. Nazarov, "Spin-flip transitions between Zeeman sublevels in semiconductor quantum dots", Phys. Rev. B **64**, 125316 (2001).

[42] C. Tahan, M. Friesen, and R. Joynt, "Decoherence of electron spin qubits in Si-based quantum computers", Phys. Rev. B **66**, 035314 (2002).

[43] S. Amasha, K. MacLean, I. P. Radu, D. M. Zumbuehl, M. A. Kastner, M. P. Hanson, and A. C. Gossard, "Electrical control of spin relaxation in a quantum dot", Phys. Rev. Lett. **100**, 046803 (2008).

[44] L. S. Langsjoen, A. Poudel, M. G. Vavilov, and R. Joynt, "Qubit relaxation from evanescent-wave Johnson noise", Phys. Rev. A **86**, 010301 (2012).

[45] V. Premakumar, M. Vavilov, and R. Joynt, "Evanescent-wave Johnson noise in small devices", Quantum Sci. Tech. **3**, 105001 (2017).

[46] E. Paladino, Y. Galperin, G. Falci, and B. Altshuler, "1/f noise: implications for solid-state quantum information", Reviews of Modern Physics **86**, 361 (2014).

[47] P. Stano and D. Loss, "Review of performance metrics of spin qubits in gated semiconducting nanostructures", Nature Reviews Physics **4**, 672–688 (2022).

[48] J. Schriefl, Y. Makhlin, A. Shnirman, and G. Schön, "Decoherence from ensembles of two-level fluctuators", New Journal of Physics **8**, 1 (2006).

[49] J. Bergli, Y. M. Galperin, and B. Altshuler, "Decoherence in qubits due to low-frequency noise", New Journal of Physics **11**, 025002 (2009).

[50] A. V. Kuhlmann, J. Houel, A. Ludwig, L. Greuter, D. Reuter, A. D. Wieck, M. Poggio, and R. J. Warburton, “Charge noise and spin noise in a semiconductor quantum device”, Nature Physics **9**, 570 (2013).

[51] G. Burkard, T. D. Ladd, J. M. Nichol, A. Pan, and J. R. Petta, “Semiconductor spin qubits”, arXiv:2112.08863 (2021).

[52] A. Saraiva, W. H. Lim, C. H. Yang, C. C. Escott, A. Laucht, and A. S. Dzurak, “Materials for silicon quantum dots and their impact on electron spin qubits”, Advanced Functional Materials **32**, 2105488 (2022).

[53] F. A. Zwanenburg, A. S. Dzurak, A. Morello, M. Y. Simmons, L. C. Hollenberg, G. Klimeck, S. Rogge, S. N. Coppersmith, and M. A. Eriksson, “Silicon quantum electronics”, Reviews of Modern Physics **85**, 961 (2013).

[54] T. Struck, A. Hollmann, F. Schauer, O. Fedorets, A. Schmidbauer, K. Sawano, H. Riemann, N. V. Abrosimov, Ł. Cywiński, D. Bougeard, et al., “Low-frequency spin qubit energy splitting noise in highly purified ^{28}Si/SiGe”, npj Quantum Information **6**, 40 (2020).

[55] E. Rashba and A. L. Efros, “Orbital mechanisms of electron-spin manipulation by an electric field”, Physical Review Letters **91**, 126405 (2003).

[56] V. N. Golovach, M. Borhani, and D. Loss, “Electric-dipole-induced spin resonance in quantum dots”, Physical Review B **74**, 165319 (2006).

[57] E. J. Connors, J. Nelson, L. F. Edge, and J. M. Nichol, “Charge-noise spectroscopy of Si/SiGe quantum dots via dynamically-decoupled exchange oscillations”, Nature Communications **13**, 940 (2022).

[58] R. M. Jock, N. T. Jacobson, M. Rudolph, D. R. Ward, M. S. Carroll, and D. R. Luhman, “A silicon singlet–triplet qubit driven by spin-valley coupling”, Nature Communications **13**, 641 (2022).

[59] P. Dutta and P. Horn, “Low-frequency fluctuations in solids: 1 f noise”, Reviews of Modern physics **53**, 497 (1981).

[60] J. B. Johnson, “The schottky effect in low frequency circuits”, Physical Review **26**, 71 (1925).

[61] Y. Choi and R. Joynt, “Anisotropy with respect to the applied magnetic field of spin qubit decoherence times”, npj Quantum Information **8**, 70 (2022).

[62] T. S. Koh, J. K. Gamble, M. Friesen, M. A. Eriksson, and S. N. Coppersmith, “Pulse-gated quantum dot hybrid qubit”, Phys. Rev. Lett. **109**, 250503 (2012).

[63] A. C. Johnson, J. R. Petta, C. M. Marcus, M. P. Hanson, and A. C. Gossard, “Singlet-triplet spin blockade and charge sensing in a few-electron double quantum dot”, Phys. Rev. B **72**, 165308 (2005).

[64] A. E. Seedhouse, T. Tanttu, R. C. Leon, R. Zhao, K. Y. Tan, B. Hensen, F. E. Hudson, K. M. Itoh, J. Yoneda, C. H. Yang, A. Morello, A. Laucht, S. N. Coppersmith, A. Saraiva, and A. S. Dzurak, "Pauli blockade in silicon quantum dots with spin-orbit control", PRX Quantum **2**, 010303 (2021).

[65] L. C. Camenzind, L. Yu, P. Stano, J. D. Zimmerman, A. C. Gossard, D. Loss, and D. M. Zumbühl, "Hyperfine-phonon spin relaxation in a single-electron GaAs quantum dot", Nat. Commun. **9**, 3454 (2018).

[66] M. Raith, P. Stano, F. Baruffa, and J. Fabian, "Theory of spin relaxation in two-electron lateral coupled quantum dots", Phys. Rev. Lett. **108**, 246602 (2012).

[67] M. Xiao, M. House, and H. W. Jiang, "Measurement of the spin relaxation time of single electrons in a silicon metal-oxide-semiconductor-based quantum dot", Phys. Rev. Lett. **104**, 096801 (2010).

[68] X. Hao, R. Ruskov, M. Xiao, C. Tahan, and H. W. Jiang, "Electron spin resonance and spin-valley physics in a silicon double quantum dot", Nat. Commun. **5**, 3860 (2014).

[69] R. Ferdous, K. W. Chan, M. Veldhorst, J. Hwang, C. Yang, H. Sahasrabudhe, G. Klimeck, A. Morello, A. S. Dzurak, and R. Rahman, "Interface-induced spin-orbit interaction in silicon quantum dots and prospects for scalability", Phys. Rev. B **97**, 241401 (2018).

[70] A. J. Sigillito, A. M. Tyryshkin, T. Schenkel, A. A. Houck, and S. A. Lyon, "All-electric control of donor nuclear spin qubits in silicon", Nat. Nanotechnol. **12**, 958–962 (2017).

[71] X. Zhang, Y. Zhou, R.-Z. Hu, R.-L. Ma, M. Ni, K. Wang, G. Luo, G. Cao, G.-L. Wang, P. Huang, X. Hu, H.-W. Jiang, H.-O. Li, G.-C. Guo, and G.-P. Guo, "Controlling synthetic spin-orbit coupling in a silicon quantum dot with magnetic field", Phys. Rev. Appl. **15**, 044042 (2021).

[72] A. Crippa, R. Maurand, L. Bourdet, D. Kotekar-Patil, A. Amisse, X. Jehl, M. Sanquer, R. Laviéville, H. Bohuslavskyi, L. Hutin, S. Barraud, M. Vinet, Y.-M. Niquet, and S. D. Franceschi, "Electrical spin driving by g-matrix modulation in spin-orbit qubits", Phys. Rev. Lett. **120**, 137702 (2018).

[73] T. Tanttu, B. Hensen, K. W. Chan, C. H. Yang, W. W. Huang, M. Fogarty, F. Hudson, K. Itoh, D. Culcer, A. Laucht, A. Morello, and A. Dzurak, "Controlling spin-orbit interactions in silicon quantum dots using magnetic field direction", Phys. Rev. X **9**, 021028 (2019).

[74] M. Marx, J. Yoneda, Á. G. Rubio, P. Stano, T. Otsuka, K. Takeda, S. Li, Y. Yamaoka, T. Nakajima, A. Noiri, et al., "Spin orbit field in a physically defined p type MOS silicon double quantum dot", arXiv:2003.07079 (2020).

[75] P. Scarlino, E. Kawakami, D. R. Ward, D. E. Savage, M. G. Lagally, M. Friesen, S. N. Coppersmith, M. A. Eriksson, and L. M. K. Vandersypen, "Second-harmonic coherent driving of a spin qubit in a Si/SiGe quantum dot", Phys. Rev. Lett. **115**, 106802 (2015).

[76] K. Takeda, J. Yoneda, T. Otsuka, T. Nakajima, M. Delbecq, G. Allison, Y. Hoshi, N. Usami, K. M. Itoh, S. Oda, T. Kodera, and S. Tarucha, "Optimized electrical control of a Si/SiGe spin qubit in the presence of an induced frequency shift", npj Quantum Inf. **4**, 54 (2018).

[77] Y. Tokura, W. G. van der Wiel, T. Obata, and S. Tarucha, "Coherent single electron spin control in a slanting zeeman field", Phys. Rev. Lett. **96**, 047202 (2006).

[78] E. Kawakami, P. Scarlino, D. R. Ward, F. R. Braakman, D. E. Savage, M. G. Lagally, M. Friesen, S. N. Coppersmith, M. A. Eriksson, and L. M. K. Vandersypen, "Electrical control of a long-lived spin qubit in a Si/SiGe quantum dot", Nat. Nanotechnol. **9**, 666–670 (2014).

[79] R. Neumann and L. Schreiber, "Simulation of micro-magnet stray field dynamics for spin qubit manipulation", J. Appl. Phys. **117**, 193903 (2015).

[80] S. Chesi, Y.-D. Wang, J. Yoneda, T. Otsuka, S. Tarucha, and D. Loss, "Single-spin manipulation in a double quantum dot in the field of a micromagnet", Phys. Rev. B **90**, 235311 (2014).

[81] R. Ferdous, E. Kawakami, P. Scarlino, M. P. Nowak, D. Ward, D. Savage, M. Lagally, S. Coppersmith, M. Friesen, M. A. Eriksson, L. M. K. Vandersypen, and R. Rahman, "Valley dependent anisotropic spin splitting in silicon quantum dots", npj Quantum Inf. **4**, 26 (2018).

[82] M. De Campos, F. Landgraf, N. Saito, S. Romero, A. Neiva, F. Missell, E. De Morais, S. Gama, E. Obrucheva, and B. Jalnin, "Chemical composition and coercivity of $SmCo_5$ magnets", J. Appl. Phys **84**, 368–373 (1998).

[83] M. E. Levinshtein, S. L. Rumyantsev, and M. S. Shur, *Properties of advanced semiconductor materials: GaN, AIN, InN, BN, SiC, SiGe* (John Wiley & Sons, 2001).

[84] J. De Vries, "Temperature-dependent resistivity measurements on polycrystalline SiO_2-covered thin gold films", Thin Solid Films **150**, 201–208 (1987).

[85] E. Kawakami, "Characterization of an electron spin qubit in a Si/SiGe quantum dot", PhD thesis (Delft University of Technology, 2016).

[86] P. W. Anderson, B. I. Halperin, and C. M. Varma, "Anomalous low-temperature thermal properties of glasses and spin glasses", Philos. Mag. **25**, 1–9 (1972).

[87] W. A. Phillips, "Tunneling states in amorphous solids", J. Low Temp. Phys. **7**, 351–360 (1972).

[88] E. Burstein, A. L. McWhorter, P. H. Miller, D. T. Stevenson, and P. B. Weisz, *Semiconductor surface physics* (University of Pennsylvania Press, 1957).

[89] M. Shehata, G. Simion, R. Li, F. A. Mohiyaddin, D. Wan, M. Mongillo, B. Govoreanu, I. Radu, K. De Greve, and P. Van Dorpe, "Modelling semiconductor spin qubits and their charge noise environment for quantum gate fidelity estimation", arXiv:2210.04539 (2022).

[90] P. Philippopoulos, "Hyperfine and spin-orbit interactions in semiconductor nanostructures", PhD thesis (McGill University, 2020).

[91] K. Takeda, J. Kamioka, T. Otsuka, J. Yoneda, T. Nakajima, M. R. Delbecq, S. Amaha, G. Allison, T. Kodera, S. Oda, and S. Tarucha, "A fault-tolerant addressable spin qubit in a natural silicon quantum dot", Sci. Adv. **2**, e1600694 (2016).

[92] C. Henkel and M. Wilkens, "Heating of trapped atoms near thermal surfaces", Europhys. Lett. **47**, 414–420 (1999).

[93] L. Langsjoen, A. Poudel, M. Vavilov, and R. Joynt, "Electromagnetic fluctuations near metallic thin films", Phys. Rev. B **89**, 115401 (2014).

[94] S. Ahn, S. Das Sarma, and J. P. Kestner, "Microscopic bath effects on noise spectra in semiconductor quantum dot qubits", Phys. Rev. B **103**, L041304 (2021).

[95] H. Zhang, K. Arai, C. Belthangady, J.-C. Jaskula, and R. L. Walsworth, "Selective addressing of solid-state spins at the nanoscale via magnetic resonance frequency encoding", npj Quantum Inf. **3**, 31 (2017).

[96] J. Zimmermann, P. London, Y. Yirmiyahu, F. Jelezko, A. Blank, and D. Gershoni, "Selective noise resistant gate", Phys. Rev. B **102**, 245408 (2020).

[97] J. Preskill, "Quantum Computing in the NISQ era and beyond", Quantum **2**, 79 (2018).

[98] D. Suter and G. A. Álvarez, "Colloquium: protecting quantum information against environmental noise", Reviews of Modern Physics **88**, 041001 (2016).

[99] G. De Lange, T. Van Der Sar, M. Blok, Z.-H. Wang, V. Dobrovitski, and R. Hanson, "Controlling the quantum dynamics of a mesoscopic spin bath in diamond", Scientific Reports **2**, 1–5 (2012).

[100] H. S. Knowles, D. M. Kara, and M. Atatüre, "Observing bulk diamond spin coherence in high-purity nanodiamonds", Nature Materials **13**, 21–25 (2014).

[101] E. Bauch, C. A. Hart, J. M. Schloss, M. J. Turner, J. F. Barry, P. Kehayias, S. Singh, and R. L. Walsworth, "Ultralong dephasing times in solid-state spin ensembles via quantum control", Physical Review X **8**, 031025 (2018).

[102] D. Bluvstein, Z. Zhang, C. A. McLellan, N. R. Williams, and A. C. B. Jayich, "Extending the quantum coherence of a near-surface qubit by coherently driving the paramagnetic surface environment", Physical Review Letters **123**, 146804 (2019).

[103] M. Joos, D. Bluvstein, Y. Lyu, D. Weld, and A. Bleszynski Jayich, "Protecting qubit coherence by spectrally engineered driving of the spin environment", npj Quantum Information **8**, 47 (2022).

[104] X. You, Z. Huang, U. Alyanak, A. Romanenko, A. Grassellino, and S. Zhu, "Stabilizing and improving qubit coherence by engineering the noise spectrum of two-level systems", Physical Review Applied **18**, 044026 (2022).

[105] J. Lisenfeld, A. Bilmes, and A. V. Ustinov, "Enhancing the coherence of superconducting quantum bits with electric fields", npj Quantum Information **9**, 8 (2023).

[106] L. Gammaitoni, P. Hänggi, P. Jung, and F. Marchesoni, "Stochastic resonance", Reviews of Modern Physics **70**, 223 (1998).

[107] B. McNamara and K. Wiesenfeld, "Theory of stochastic resonance", Physical Review A **39**, 4854 (1989).

[108] V. A. Shneidman, P. Jung, and P. Hanggi, "Weak-noise limit of stochastic resonance", Physical Review Letters **72**, 2682 (1994).

[109] L. Gammaitoni, F. Marchesoni, E. Menichella-Saetta, and S. Santucci, "Stochastic resonance in the strong-forcing limit", Physical Review E **51**, R3799 (1995).

[110] R. Löfstedt and S. Coppersmith, "Stochastic resonance: nonperturbative calculation of power spectra and residence-time distributions", Physical Review E **49**, 4821 (1994).

[111] R. Löfstedt and S. Coppersmith, "Quantum stochastic resonance", Physical Review Letters **72**, 1947 (1994).

[112] M. Grifoni and P. Hänggi, "Nonlinear quantum stochastic resonance", Physical Review E **54**, 1390 (1996).

[113] T. Wagner, P. Talkner, J. C. Bayer, E. P. Rugeramigabo, P. Hänggi, and R. J. Haug, "Quantum stochastic resonance in an ac-driven single-electron quantum dot", Nature Physics **15**, 330–334 (2019).

[114] M. Hänze, G. McMurtrie, S. Baumann, L. Malavolti, S. N. Coppersmith, and S. Loth, "Quantum stochastic resonance of individual Fe atoms", Science Advances **7**, eabg2616 (2021).

[115] R. J. Schoelkopf, A. A. Clerk, S. M. Girvin, K. W. Lehnert, and M. H. Devoret, "Qubits as spectrometers of quantum noise", in *Quantum noise in mesoscopic physics* (Springer Netherlands, Dordrecht, 2003), pp. 175–203.

[116] A. Saiko, S. Markevich, and R. Fedaruk, "Dissipative two-level systems under ultrastrong off-resonant driving", Physical Review A **93**, 063834 (2016).

[117] J. Lisenfeld, C. Müller, J. H. Cole, P. Bushev, A. Lukashenko, A. Shnirman, and A. V. Ustinov, "Measuring the temperature dependence of individual two-level systems by direct coherent control", Physical Review Letters **105**, 230504 (2010).

[118] J. Lisenfeld, A. Bilmes, S. Matityahu, S. Zanker, M. Marthaler, M. Schechter, G. Schön, A. Shnirman, G. Weiss, and A. V. Ustinov, "Decoherence spectroscopy with individual two-level tunneling defects", Scientific Reports **6**, 1–8 (2016).

[119] M. Constantin, C. Y. Clare, and J. M. Martinis, "Saturation of two-level systems and charge noise in josephson junction qubits", Physical Review B **79**, 094520 (2009).

[120] H. Brox, J. Bergli, and Y. M. Galperin, "Effects of external driving on the coherence time of a josephson junction qubit in a bath of two-level fluctuators", Physical Review B **84**, 245416 (2011).

[121] A. Poudel, L. S. Langsjoen, M. G. Vavilov, and R. Joynt, "Relaxation in quantum dots due to evanescent-wave johnson noise", Phys. Rev. B **87**, 045301 (2013).

[122] J. P. Dodson, "Overlapping aluminum-gate quantum dots for valley-orbit based qubits in Si/SiGe", PhD thesis (The University of Wisconsin-Madison, 2021).

[123] B. Undseth, O. Pietx-Casas, E. Raymenants, M. Mehmandoost, M. T. Madzik, S. G. Philips, S. L. de Snoo, D. J. Michalak, S. V. Amitonov, L. Tryputen, et al., "Hotter is easier: unexpected temperature dependence of spin qubit frequencies", arXiv:2304.12984 (2023).

[124] A. E. Seedhouse, I. Hansen, A. Laucht, C. H. Yang, A. S. Dzurak, and A. Saraiva, "Quantum computation protocol for dressed spins in a global field", Physical Review B **104**, 235411 (2021).

[125] I. Hansen, A. E. Seedhouse, A. Saraiva, A. Laucht, A. S. Dzurak, and C. H. Yang, "Pulse engineering of a global field for robust and universal quantum computation", Physical Review A **104**, 062415 (2021).

[126] C. Dekker, A. J. Scholten, F. Liefrink, R. Eppenga, H. van Houten, and C. T. Foxon, "Spontaneous resistance switching and low-frequency noise in quantum point contacts", Phys. Rev. Lett. **66**, 2148–2151 (1991).

[127] T. Sakamoto, Y. Nakamura, and K. Nakamura, "Distributions of single-carrier traps in GaAs/$\mathrm{Al}_x\mathrm{Ga}_{1-x}\mathrm{As}$ heterostructures", Applied Physics Letters **67**, 2220–2222 (1995).

[128] C. Kurdak, C.-J. Chen, D. C. Tsui, S. Parihar, S. Lyon, and G. W. Weimann, "Resistance fluctuations in GaAs/$\mathrm{Al}_x\mathrm{Ga}_{1-x}\mathrm{As}$ quantum point contact and hall bar structures", Phys. Rev. B **56**, 9813–9818 (1997).

[129] C. Buizert, F. H. L. Koppens, M. Pioro-Ladrière, H.-P. Tranitz, I. T. Vink, S. Tarucha, W. Wegscheider, and L. M. K. Vandersypen, “Insitu reduction of charge noise in GaAs/AlGaAs Schottky-gated devices”, Phys. Rev. Lett. **101**, 226603 (2008).

[130] M. Pioro-Ladrière, J. H. Davies, A. R. Long, A. S. Sachrajda, L. Gaudreau, P. Zawadzki, J. Lapointe, J. Gupta, Z. Wasilewski, and S. Studenikin, “Origin of switching noise in GaAs/$\mathrm{Al}_x\mathrm{Ga}_{1-x}\mathrm{As}$ lateral gated devices”, Phys. Rev. B **72**, 115331 (2005).

[131] K. Takeda, T. Obata, Y. Fukuoka, W. M. Akhtar, J. Kamioka, T. Kodera, S. Oda, and S. Tarucha, “Characterization and suppression of low-frequency noise in Si/SiGe quantum point contacts and quantum dots”, Applied Physics Letters **102**, 123113 (2013).

[132] X. Croot, S. Pauka, M. Jarratt, H. Lu, A. Gossard, J. Watson, G. Gardner, S. Fallahi, M. Manfra, and D. Reilly, “Gate-sensing charge pockets in the semiconductor-qubit environment”, Phys. Rev. Applied **11**, 064027 (2019).

[133] J. Campbell and P. Lenahan, “Density of states of P_{b1} Si/SiO_2 interface trap centers”, Applied Physics Letters **80**, 1945–1947 (2002).

[134] M. Hofheinz, X. Jehl, M. Sanquer, G. Molas, M. Vinet, and S. Deleonibus, “Individual charge traps in silicon nanowires”, The European Physical Journal B - Condensed Matter and Complex Systems **54**, 299–307 (2006).

[135] J. M. Boter, X. Xue, T. Krähenmann, T. F. Watson, V. N. Premakumar, D. R. Ward, D. E. Savage, M. G. Lagally, M. Friesen, S. N. Coppersmith, M. A. Eriksson, R. Joynt, and L. M. K. Vandersypen, “Spatial noise correlations in a Si/SiGe two-qubit device from Bell state coherences”, Physical Review B **101**, 235133 (2020).

[136] J. Yoneda, J. Rojas-Arias, P. Stano, K. Takeda, A. Noiri, T. Nakajima, D. Loss, and S. Tarucha, “Noise-correlation spectrum for a pair of spin qubits in silicon”, arXiv:2208.14150 (2022).

[137] J. Rojas-Arias, A. Noiri, P. Stano, T. Nakajima, J. Yoneda, K. Takeda, T. Kobayashi, A. Sammak, G. Scappucci, D. Loss, and S. Tarucha, “Spatial noise correlations beyond nearest-neighbor in ^{28}Si/SiGe spin qubits”, arXiv:2302.11717 (2023).

[138] T. F. Watson, S. G. J. Philips, E. Kawakami, D. R. Ward, P. Scarlino, M. Veldhorst, D. E. Savage, M. G. Lagally, M. Friesen, S. N. Coppersmith, M. A. Eriksson, and L. M. K. Vandersypen, “A programmable two-qubit quantum processor in silicon”, Nature **555**, 633–637 (2018).

[139] S. Freer, S. Simmons, A. Laucht, J. T. Muhonen, J. P. Dehollain, R. Kalra, F. A. Mohiyaddin, F. E. Hudson, K. M. Itoh, J. C. McCallum, D. N. Jamieson, A. S. Dzurak, and A. Morello, “A single-atom quantum memory in silicon”, Quantum Science and Technology **2**, 015009 (2017).

[140] C. Müller, J. Lisenfeld, A. Shnirman, and S. Poletto, "Interacting two-level defects as sources of fluctuating high-frequency noise in superconducting circuits", Physical Review B **92**, 035442 (2015).

[141] C. Müller, J. H. Cole, and J. Lisenfeld, "Towards understanding two-level-systems in amorphous solids: insights from quantum circuits", Reports on Progress in Physics **82**, 124501 (2019).

[142] R. Rahman, S. H. Park, T. B. Boykin, G. Klimeck, S. Rogge, and L. C. L. Hollenberg, "Gate-induced g-factor control and dimensional transition for donors in multivalley semiconductors", Phys. Rev. B **80**, 155301 (2009).

[143] Center for High-Throughput Computing at UW-Madison, `https://doi.org/10.21231/GNT1-HW21`.

[144] O. A. Dicks, J. Cottom, A. L. Shluger, and V. V. Afanas'ev, "The origin of negative charging in amorphous Al_2O_3 films: the role of native defects", Nanotechnology **30**, 205201 (2019).

[145] C.-C. Hung, L. Yu, N. Foroozani, S. Fritz, D. Gerthsen, and K. D. Osborn, "Probing hundreds of individual quantum defects in polycrystalline and amorphous alumina", Physical Review Applied **17**, 034025 (2022).

[146] M. Yaghoubi, M. E. Foulaadvand, A. Bérut, and J. Łuczka, "Energetics of a driven brownian harmonic oscillator", Journal of Statistical Mechanics: Theory and Experiment **2017**, 113206 (2017).

[147] D. Mickelsen, H. M. Carruzzo, S. N. Coppersmith, and C. C. Yu, "Effects of temperature fluctuations on charge noise in quantum dot qubits", arXiv:2305.14515 (2023).

[148] R. E. Throckmorton and S. D. Sarma, "A generalized model of the noise spectrum of a two-level fluctuator in the presence of an electron subbath", arXiv:2305.14348 (2023).